Signatures of the *r*-process in Ancient Stellar Populations Using Barium Abundances

Thesis by
Gina Elizabeth Duggan

In Partial Fulfillment of the Requirements for the
Degree of
Doctor of Philosophy in Astrophysics

CALIFORNIA INSTITUTE OF TECHNOLOGY
Pasadena, California

2020
Defended October 21, 2019

Gina Elizabeth Duggan
ORCID: 0000-0002-9256-6735

"Do not complain beneath the stars about the lack of bright spots in your life."

——Bjørnstjerne Bjørnson

To the terrestrial and astrophysical bright spots in my life

ACKNOWLEDGEMENTS

If I had to describe graduate school in one word it would be "struggle". Struggle to understand cosmology. Struggle to keep up with my peers. Struggle to meet my—or anyone's—expectations. Struggle to juggle being a student, TA, and researcher. Later, struggle to juggle being a scientist, wife, mother, and myself. *Thankfully* I have had many, many people support, believe in, and encourage me. Without you I can think of several times when I would have left before this thesis was written. Thank you for helping me persevere.

Thank you to the Caltech scientists and engineers that have helped me complete my thesis. First and foremost, thank you to my thesis advisor, Evan Kirby. You approach science with such joy, which I have always appreciated and admired. Thank you to Phil Hopkins for making me an honorary member of your research group. Thank you to Shri Kulkarni for your career advice and mentorship. Thank you to the ZTF engineering team for being helpful and welcoming, specifically Richard Dekany and Roger Smith. Thank you to the astronomy technical support team for quickly and cheerfully fixing what I had broken. Thank you to Gita Patel for helping me with miscellaneous questions and for welcoming me into the office each day.

Thank you to my scientific mentors for supporting and encouraging me. Thank you to Ben Mazin for giving me my first research experience in astronomy and for continuing to check in on me. Thank you to Anneila Sargent, Gwen Rudie, and Lynne Hillenbrand for helping me see how to proceed and giving me the advice I needed.

Thank you to the Graduate Student Council and administration at Caltech for allowing me to advocate for graduate students. In particular, I'd like to thank Kate McAnulty, Felicia Hunt, Doug Rees, Joseph Shepherd, and Sofie Leon for working to improve the graduate student experience.

Thank you to other support personnel at Caltech for encouraging me, specifically Maggie Ateia, Denise Lin, and Alice Sogomonian.

Thank you to the astronomy graduate students for creating and maintaining a welcoming and caring environment. Chatting with Jake Jencson, Denise Schmitz, Matthew Orr, Ivanna Escala, and Nikita Kamraj gave me extra motivation to come into my office.

Thank you to Allison Strom, Alicia Lanz, and Annie Serbulea for being my friends throughout this entire journey.

Thank you to my family for loving me and supporting me; thanks especially to my parents, Gil and Lisa. I am extremely fortunate to grow up believing I can be whatever I choose to be, and to know that you will help me achieve that goal in any way that you can.

Thank you to Mark for going through every high and low along with me. You are what makes a good life a great life.

Finally, thank you, Ella. You joined this journey partway through, but you have made the end even sweeter.

ABSTRACT

For over sixty years scientists have known that a large percentage of heavy elements are created by the rapid neutron-capture process (*r*-process). However, a clear picture of where the *r*-process occurs has remained elusive. Many astrophysical origins have been proposed—each with a range of possible chemical yields and rates. Discovering which origin (or combinations of origins) truly produce the heavy elements we see on Earth is a daunting task.

This thesis seeks to provide observational constraints to pinpoint the dominant origin of the *r*-process. The majority of this thesis uses Galactic Archaeology to look for *r*-process signatures in ancient stellar populations (e.g., dwarf galaxies and globular clusters). These ancient stellar populations provide the clearest "experiments" to observe how quickly and how much *r*-process was created. The *r*-process signature we observe is the amount of barium in individual red giant branch stars in these stellar populations. Chapter 2 discusses how these barium measurements are made from individual extragalactic stars and presents the largest catalog of barium abundances in dwarf galaxies to date.

Chapter 3 compares the *r*-process signature—barium—to other elements (e.g., magnesium and iron) in the same galaxy to see how the timescale of *r*-process enrichment compares to the other abundances (whose origins are known). This analysis found that the *r*-process timescale was more delayed than core-collapse supernovae. This points to neutron star mergers (NSMs) as the dominant source of *r*-process in the early history of dwarf galaxies.

Chapter 4 uses a galactic chemical evolution model to test what *r*-process timescales, yields, and rates are needed to recreate the observations presented in Chapter 2. Preliminary results indicate that NSMs must be included in order for the model to match the observations. In addition, Chapter 4 presents what yield of barium is needed from NSMs to recreate the observations.

Chapter 5 tests if the stars in the globular cluster M15 were enriched by the *r*-process after they were born. M15 has an unusual abundance pattern with $\sim$ 1 dex variation in *r*-process abundances even though most other elements, including iron, do not show a variation. New measurements of barium abundances in main sequence and red giant branch stars of M15 show that the stars were born with their *r*-process enrichment. This means that an *r*-process event occurred quickly after the cluster

was born—while it was still forming stars—and resulted in uneven enrichment.

Finally, Chapter 6 presents a solution to one of the technical challenges in locating the sites of *r*-process nucleosynthesis. Chapter 6 describes how to accurately measure the position and orientation of the CCDs in Zwicky Transient Facility's (ZTF's) camera. ZTF is a transient survey that—among other science goals—searches for the electromagnetic counterpart of NSM detections with LIGO. The work included in this chapter increased the survey efficiency of ZTF, which will aid ZTF in localizing transient events, including NSMs. Following up NSMs found by LIGO can provide direct measurements of the amount of *r*-process material created by NSMs.

Altogether, this thesis has made strides to identifying the origin of the *r*-process. Chapters 3 and 4 identify NSMs as the dominant source of *r*-process elements in dwarf galaxies. However, Chapter 5 found that globular cluster M15 needs a *r*-process event to occur quickly—quicker than is typically expected from a NSM. The observational constraints that have resulted from this thesis provide important clues to where the heaviest elements are made.

PUBLISHED CONTENT AND CONTRIBUTIONS

Kirby, E. N., G. E. Duggan, et al. (in prep). “The Stars in M15 Were Born with the *r*-process”. In: *Astrophysical Journal, Letters*.
G.E.D. co-authored the observing proposal, adapted the analysis software, and analyzed the data.

Duggan, G. E., R. Dekany, and J. Milburn (2018). “Aligning the ZTF science focal plane using stellar images”. In: *Ground-based and Airborne Instrumentation for Astronomy VII*. Vol. 10702. Society of Photo-Optical Instrumentation Engineers (SPIE) Conference Series, 107024K. DOI: 10.1117/12.2309994.
G.E.D. planned and conducted the observations and wrote the paper. For one of the two methods presented (the "donut method"), G.E.D. developed the analysis software and analyzed the data.

Duggan, G. E., E. N. Kirby, et al. (2018). “Neutron Star Mergers are the Dominant Source of the r-process in the Early Evolution of Dwarf Galaxies”. In: *Astrophysical Journal* 869, 50, p. 50. DOI: 10.3847/1538-4357/aaeb8e. arXiv: 1809.04597.
G.E.D. generated barium grid of synthetic spectra, developed the analysis software, analyzed the data, and wrote the paper.

TABLE OF CONTENTS

Acknowledgements iv
Abstract vi
Published Content and Contributions viii
Table of Contents ix
List of Illustrations xi
List of Tables xiii
Chapter I: Introduction 1
1.1 Introduction to the *s*- and the *r*-processes 2
1.2 Narrowing Down the Search for the Dominant R-Process Origin . . . 7
1.3 Barium and Europium as Probes of the *r*-process 10
1.4 Outline of this Thesis 13
Chapter II: Measuring Barium Abundances in Dwarf Galaxies Using Medium-Resolution Spectra for the First Time 21
2.1 Introduction 21
2.2 Observations 23
2.3 Stellar Parameters 28
2.4 Synthetic Spectra 29
2.5 Barium Measurement Technique 32
2.6 The Catalog 32
2.7 Systematic Uncertainty 33
Chapter III: Neutron Star Mergers Are the Dominant Source of the r-process in the Early Evolution of Dwarf Galaxies 50
3.1 Introduction 51
3.2 Distinguishing Between Dominant R-Process Candidates Based on Timescales for the First Time 52
3.3 Sample of Barium Abundances in Dwarf Galaxies 53
3.4 Why AGB Stars are Not the Dominant Source of Barium Enrichment at Early Times 55
3.5 New Critical Piece of Evidence of the Dominant R-Process Origin . . 58
3.6 NSMs Could Be the Dominant Source of Barium in Dwarf Galaxies . 61
3.7 Implications 62
3.8 Summary 63
Chapter IV: Quantitative Constraints on the r-process in Dwarf Galaxies from a Galactic Chemical Evolution Model 69
4.1 Introduction 69
4.2 Main Assumptions and Equations 70
4.3 Results 78
4.4 Conclusion: Important Constraints on Neutron Star Mergers 82
4.5 Next Steps 87

Chapter V: The Stars in M15 Were Born with the *r*-process 94
5.1 Introduction 94
5.2 Observations and Abundance Measurements 96
5.3 Mixing on the RGB 97
5.4 Results 99
5.5 Discussion 101
Chapter VI: Aligning the ZTF Science Focal Plane Using Stellar Images . . . 112
6.1 Introduction 112
6.2 Placing the science focal plane in approximate focus 113
6.3 Creating a height map of the science focal plane 115
6.4 Measuring adjustments to the science focus plane from height maps . 129
6.5 Compare the results of the parabola and donut methods 131
6.6 Final science focal plane adjustments 132
6.7 Conclusion 133
Chapter VII: Outro 137

LIST OF ILLUSTRATIONS

Number		*Page*
1.1	Chart of nuclides with the *s*- and *r*-process paths indicated.	3
1.2	Abundance of isotopes with origins labeled.	4
1.3	Neutron-capture cross section decreases at closed shells.	5
1.4	Chart of nuclides color-coded by main decay type.	6
1.5	Cartoon of how free neutrons are created in AGB stars.	8
1.6	High barium and europium enrichment in Reticulum II.	10
2.1	Example barium measurement for a single star.	33
2.2	Comparing our [Ba/Fe] measurements with and without assuming LTE.	37
2.3	Comparison of our MRS to literature HRS abundance measurements.	39
2.4	[Ba/Fe] error derived from literature HRS abundance measurements.	41
2.5	Globular cluster [Ba/Fe] measurements.	42
2.6	[Ba/Fe] error derived from globular cluster abundance measurements.	42
3.1	Barium abundance measurements in dwarf galaxies.	54
3.2	Literature [Ba/Eu] measurements for each galaxy.	59
3.3	Comparison of the trend of [Mg/Fe] and [Ba/Fe]$_r$ as a function of [Fe/H] for each galaxy.	60
4.1	Overview of how GCE model returns abundance trends.	72
4.2	Cristallo AGB yield models.	73
4.3	Karakas AGB yield models.	73
4.4	Supernova yield models.	74
4.5	GCE model with default parameters.	77
4.6	GCE model for two different SFHs.	78
4.7	Varying AGB model yields.	80
4.8	Varying SNe II model yields.	81
4.9	A single GCE model with barium coming from AGB stars, CCSNe, and NSMs.	83
4.11	GCE models with various levels of barium contributed by NSMs	86
4.12	GCE model with NSMs for two different SFHs.	88
5.1	The initial conditions for a MESA model of a star polluted by an *r*-process event.	98
5.2	Evolution of surface-polluting *r*-process material in M15.	99

5.3 The barium abundances in M15 show no trend with stellar luminosity. 100
6.1 Stellar FWHM map of the SFP. 115
6.2 Measuring the height for a ZTF star using the parabola method. . . . 117
6.3 Measuring the height for a PTF star using the parabola method. . . . 117
6.4 Height map of PTF's SFP created from images taken in October 2015. 121
6.5 Height map of sections of PTF's SFP from October 2015. 123
6.6 PTF profilometry height map published in Rahmer et al. (2008). . . . 123
6.7 Demonstration of the donut method. 124
6.8 Example of the vignetted ZTF pupil used for image simulation. . . . 126
6.9 Master map of α as a function of position. 127
6.10 Removing the global tip/tilt from a height map. 129
6.11 Fit a plane to each CCD. 131
6.12 CCD residual heights. 132
6.13 Master height maps using the parabola and donut methods. 133
6.14 Height difference between the parabola and donut methods. 134

LIST OF TABLES

Number *Page*

2.1 Spectroscopic Targets 22
2.2 DEIMOS Observations 24
2.3 Adopted Solar Composition 28
2.4 Barium Synthetic Spectra Grid 30
2.5 Spectral Line List 31
2.6 DEIMOS Multi-Element Abundances Catalog of dSph Stars 34
2.7 Non-LTE Effects 36
2.8 Previously Published HRS Abundance Methods 38
2.9 Comparison Between High-Resolution and DEIMOS Abundances . . 40
2.10 DEIMOS Multi-Element Abundances Catalog of Globular Cluster Stars 44
2.11 Abundance Error Floor 45
3.1 Properties of Dwarf Galaxies 56
5.1 Barium Abundances in M15 103
6.1 Final plane coefficients for the 16 ZTF science CCDs. 135

Chapter 1

INTRODUCTION

Some sections in this chapter are published in Duggan et al. (2018).

Scientists have known that the elements on earth are the same elements that are in our sun's atmosphere since the 1860s. William Huggins led research that compared the spectrum of the sun to spectra of various metals on earth (Huggins, 1864). He eventually concluded that the elements on the earth and sun are the same. This discovery led to the often-quoted fact that humans (and everything we see and touch) are made of stardust.

But how is this stardust (i.e., elements) made? In 1920, F. Aston presented evidence that the mass of helium is less than the mass of four hydrogen atoms (these results were later published in Aston 1927). This showed that the fusion of light elements to form heavier elements are exothermic reactions (i.e., these reactions release energy). Inspired by this result, Arthur Eddington proposed that the sun's energy is powered by hydrogen fusing into helium (Eddington, 1920). It was later confirmed that the nucleosynthesis of elements lighter than iron occurs in hydrostatic equilibrium in stars.

However, creating elements heavier than iron by fusing lighter elements are endothermic reactions (i.e., these reactions require energy). The binding energy per nucleon is maximized for isotopes with similar masses to iron, which are described as the iron peak. This peak was included in Aston (1927) and has been studied much more rigorously in the years since (e.g., Wapstra and Audi, 1985). The binding energy per nucleon is impacted by two competing forces. (1) The nuclear force holds the nucleus together, and its strength diminishes rapidly with distance. (2) The Coulomb repulsion between same-charge particles pushes the nucleus apart and its strength diminishes less rapidly with distance. For nuclei heavier (and therefore larger) than the iron peak, the nuclear force is diminished by the increasing nucleus size and the Coulomb repulsion is increased by the large positive charge of the nucleus. Instead of directly adding a proton to the atomic nucleus to create a heavier element, a neutron is captured and β-decays into a proton. This neutron-capture process avoids the Coulomb repulsion of the large positive nucleus. The challenge of neutron-capture processes is that we need free neutrons to exist, but free neu-

trons spontaneously decay into protons in ~ 15 minutes on average (Beringer et al., 2012). Therefore for heavy elements to be created, we need a source of neutrons that can be quickly captured by an atomic nucleus. The relative timescales of a neutron being captured and that neutron β-decaying into a proton define two types of neutron-capture processes: the slow neutron-capture process (s-process) and the rapid neutron-capture process (r-process).

In 1957, Burbidge et al.'s and Cameron's monumental papers independently summarized the different nucleosynthesis processes known today and proposed the possible astrophysical origins for the s- and r-processes.

Today, over sixty years after Burbidge et al. (1957) and Cameron (1957), the origin of heavy elements that are produced by the r-process remains unknown. This is arguably the largest gap in our current knowledge of stellar nucleosynthesis. Many potential sites have been identified, and some have been ruled out in the following years (see Section 1.2). This thesis tackles this question: What is the main astrophysical site that creates heavy elements via the r-process?

1.1 Introduction to the s- and the r-processes

The s- and r-processes occur in very different physical scenarios and originate in very different astrophysical origins. The s-process occurs in episodes lasting from $10^2 - 10^4$ yrs. The s-process has a very long time between each free neutron being captured ($\tau_{\rm n} \sim 10 - 10^4$ yr), and this timescale is much longer than the timescale for that neutron to β-decay into a proton. In the s-process, when an element captures a neutron to form an unstable element, the captured neutron will β-decay into a proton before capturing another neutron. This causes the s-process to follow the valley of stability (see the blue line in Figure 1.1). This means that some isotopes (e.g., ^{134}Xe) are not created by the s-process, because the isotope with one less neutron (e.g., ^{133}Xe) is unstable. Therefore, that isotope is only created through the r-process.

The r-process occurs in a single event that lasts seconds, where a nucleus captures many neutrons ($\tau_{\rm n} \sim 10^{-2} - 10$ sec) before those neutrons β-decay into protons. In the r-process the isotopes trace the nuclear drip line, which delineates the most neutron rich isotopes possible. Then these very neutron-rich isotopes β-decay to the valley of stability (green arrows in Figure 1.1). This causes some isotopes (e.g., ^{134}Ba) to be shielded by stable isotopes closer to the nuclear drip line (e.g., ^{134}Xe). Therefore, isotopes like ^{134}Ba are only created by the s-process.

We have now discussed the different isotope pathways that the s- and r-processes

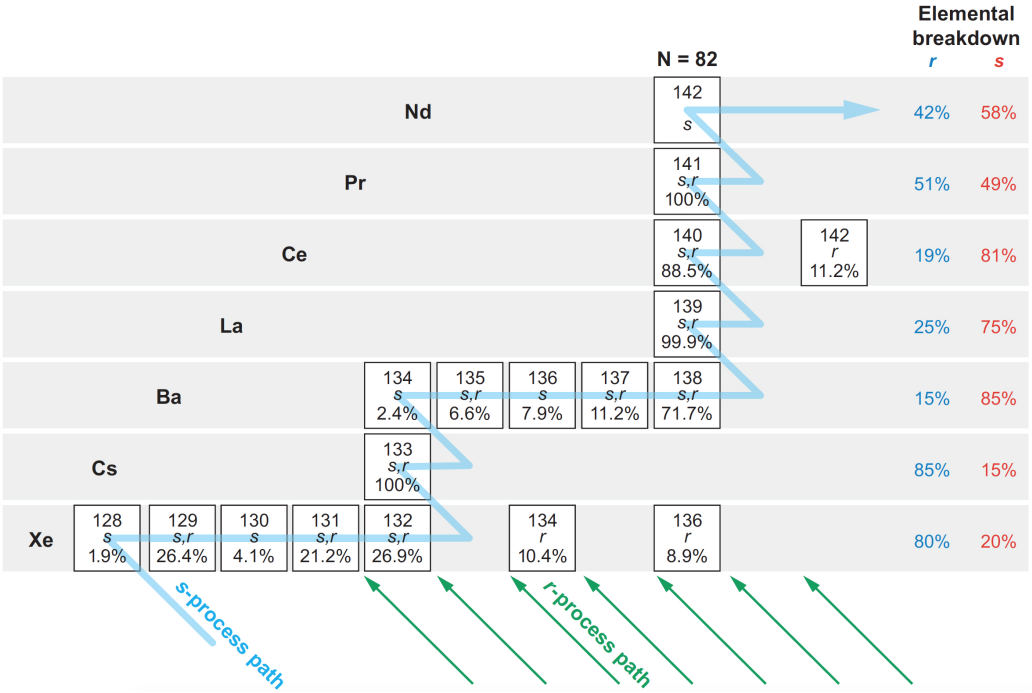

Figure 1.1: This chart of nuclides organizes stable isotopes based on the number of neutrons (x-axis) and the number of protons (y-axis). Each row includes isotopes of the same element. For each isotope the following properties are included: total mass, main neutron-capture processes, and distribution of the element in each stable isotope. Capturing a neutron is equivalent to moving one isotope to the right in this diagram. Converting a neutron into a proton is called β^--decay and is equivalent to moving diagonally up and left in this diagram. The *s*-process path is indicated in blue, where an unstable isotope will β-decay before capturing another neutron. The *r*-process path captures many neutrons along the nuclear drip line, which occurs off this diagram to the lower right. Then the *r*-process path β-decays until it forms a stable isotope (green arrows). Some isotopes are created by only one process (e.g., ^{134}Xe and ^{134}Ba); most isotopes are created by both processes. The percentage of each element that is created by the *s*- and *r*-processes in the solar system is given on the right. Figure from C. Sneden, Cowan, and Gallino (2008).

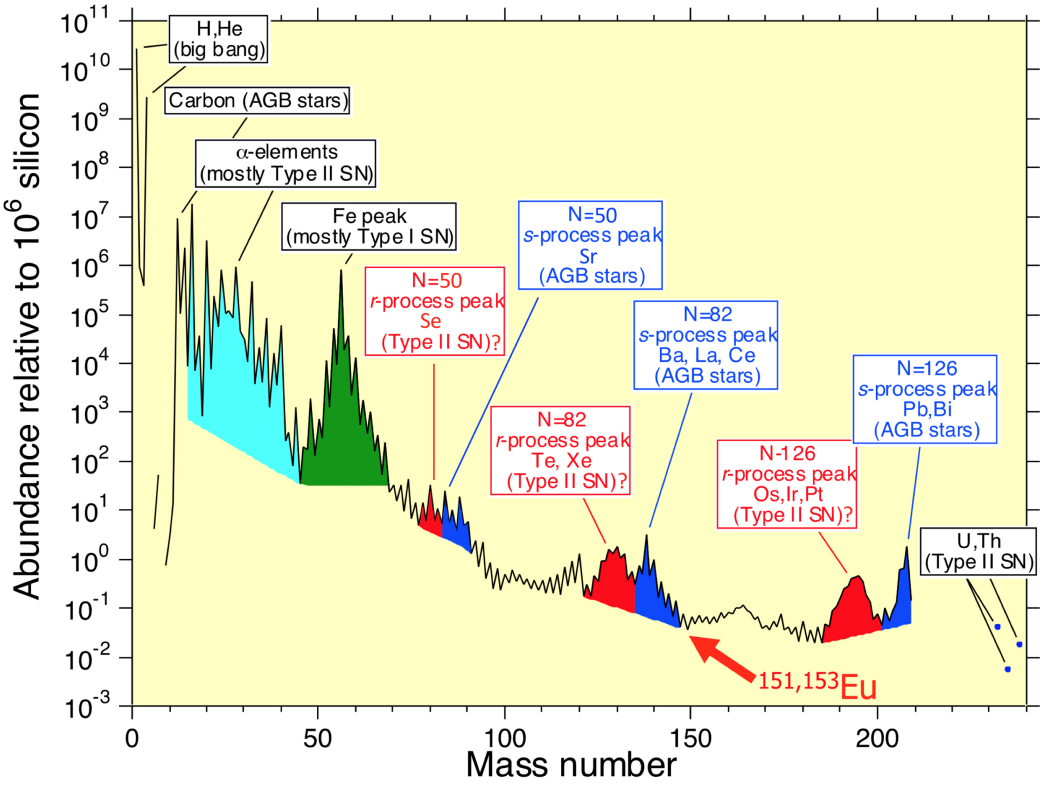

Figure 1.2: Relative abundance of isotopes in the sun as a function of total atomic mass. Over-abundances are highlighted and their main origin is labeled. Notice that the three neutron-capture peaks are labeled and the *r*-process peak occurs at a slightly lower mass than the *s*-process peak. The origin of the *r*-process is labeled as "Type II SN?" and this uncertainty is the subject of this thesis. Figure from Roberto Gallino (private communication).

take and how these pathways cause isotopes to be created by *s*- and/or *r*-processes. However, elemental abundance peaks also affect the relative amount of each element created by the *s*- and *r*-processes.

Elemental Abundance Peaks

Suess and Urey discovered in 1956 that the solar abundance pattern (relative abundances as a function of nucleus mass, Figure 1.2) has several clear peaks. These peaks correspond to "magic" numbers where isotopes with these numbers of protons and/or neutrons are over-produced. It was later found that these "magic" numbers correspond to low neutron-capture cross sections (see Figure 1.3) and closed proton/neutron shells. These "magic" numbers are: 2, 8, 20, 28, 50, 82, and 126 (see Figure 1.4). Because the neutron-capture cross section decreases at these numbers, there is a build-up of isotopes when the total number of protons and/or neutrons

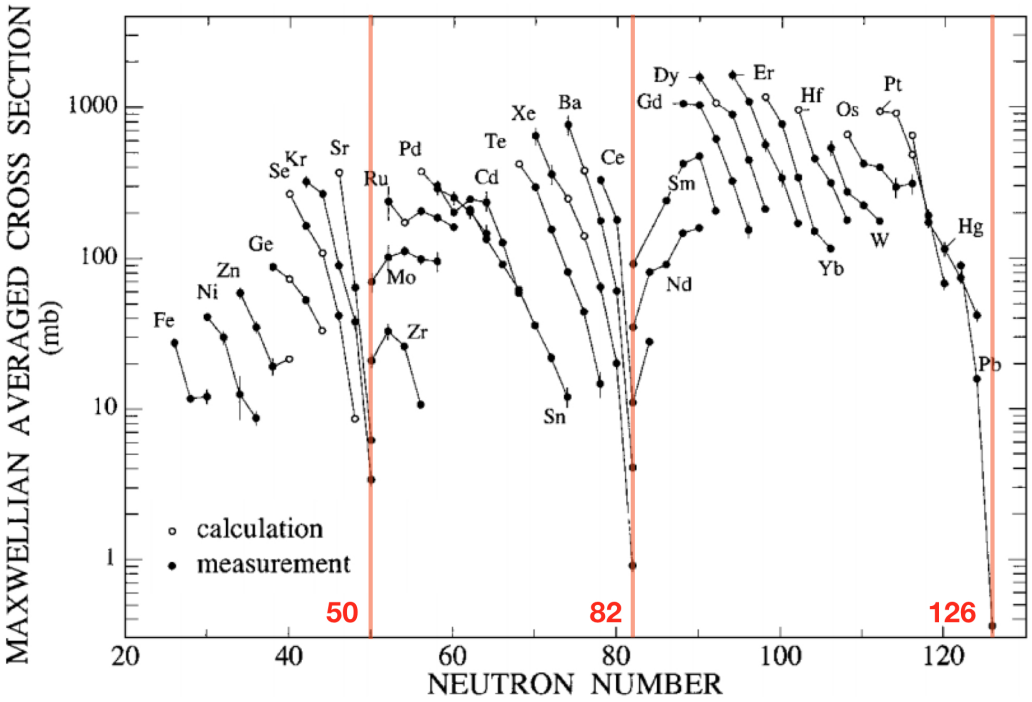

Figure 1.3: Neutron-capture cross sections for individual isotopes are shown for different neutron numbers. Lines connect isotopes of the same element. The cross sections are for nuclei with even numbers of nucleons along the *s*-process path. The neutron-capture cross sections decrease at the three neutron numbers (red) that correspond to closed neutron shells. These neutron numbers are coined "magic" numbers and cause three abundance peaks in neutron-capture elements. Figure adapted from Bao et al. (2000).

equals one of these numbers.

There are three abundance peaks for neutron-capture elements that are caused by closed neutron shells (Figure 1.2). The first, second, and third peaks correspond to 50, 82, and 126 neutrons, respectively. Each broad peak is split into an *s*- and *r*-process peak. As we discussed in the previous section, the *s*-process follows the valley of stability. Therefore, the *s*-process peak occurs when the total number of neutrons equal a "magic" number (i.e., 50, 82, or 126). The column of stable isotopes with 82 neutrons is labeled in Figure 1.1. It follows that ^{138}Ba, ^{139}La, and ^{140}Ce are over-produced and form the second *s*-process peak (as labeled in Figure 1.2). On the other hand, the *r*-process pathway does not capture neutrons around the valley of stability. Instead, the *r*-process captures neutrons near the nuclear drip line. Therefore, the isotope build-up caused by closed neutron shells occurs in the unstable region (around the bottom pink edge in Figure 1.4). This build-up

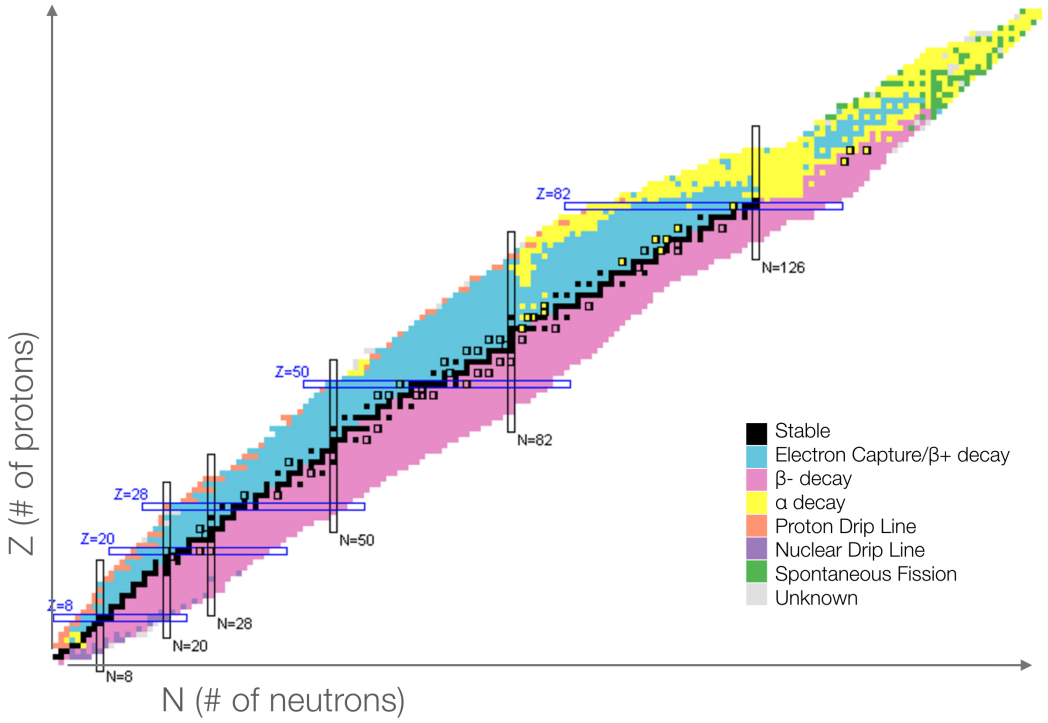

Figure 1.4: This chart of nuclides color-codes unstable isotopes by their main decay type. Blue rectangles indicate which isotopes have a closed neutron or proton shell. The *r*-process path follows the nuclear drip line (bottom pink edge) until the isotopes start β-decaying to the valley of stability (stable elements represented by black boxes along the center of this diagram). Figure adapted from `www.nndc.bnl.gov/nudat2/`.

then β-decays to stable elements, causing the *r*-process peak to occur at slightly lower atomic number than the *s*-process peak (see Figure 1.2). For example, the doubly-magic unstable isotope ^{132}Sn (N=82, P=50) is created by the *r*-process and β-decays to ^{132}Xe, which belongs to the second *r*-process peak.

There is a subtle rare earth peak around A $\sim$ 160 that is not caused by a closed neutron shell. This peak includes most of the lanthanide elements and the precise mechanism that creates the rare earth peak is still debated (Mumpower, McLaughlin, and Surman, 2012). It is likely caused by fission of elements heavier than the third neutron-capture peak and/or freezeout as unstable neutron-rich isotopes β-decay to the valley of stability.

The first peak of neutron-capture elements may be created in a different astrophysical origin than the second and third peak. This will be discussed in more detail in Section 1.2.

Astrophysical Origin of the *s*-process

The *s*-process requires a lower neutron flux ($\sim 10^5 - 10^{11}$ neutrons/cm^2/s) and predominantly occurs in low and intermediate mass asymptotic giant branch (AGB) stars. Low mass AGB stars ($M_* \lesssim 4M_\odot$) generate a neutron flux when third dredge-up episodes mix protons from the convective hydrogen envelope into the He-intershell (the region between H and He shell burning, see Figure 1.5). A ^{13}C rich area—^{13}C pocket—is created by $^{12}C(p,\gamma)^{13}N(\beta^+\nu)^{13}C$ reactions[1]. Free neutrons are then released via $^{13}C(\alpha,n)^{16}O$. In intermediate mass AGB stars ($M_* \gtrsim 4M_\odot$), the base of the He intershell reaches sufficient temperatures ($T > 3 \times 10^8$ K) during a thermal pulse for a different reaction to release free neutrons: $^{14}N(\alpha,\gamma)^{18}F(\beta^+\nu)^{18}O(\alpha,\gamma)^{22}Ne(\alpha,n)^{25}Mg$. Once free neutrons are created by either ^{13}C or ^{22}Ne reactions in the He-intershell, these neutrons are captured by preexisting metals and create *s*-process elements. These *s*-process elements are redistributed to the surface of the star through flash-driven convection and third dredge-up episodes. The *s*-process elements are then ejected into the ISM through strong stellar outflows or winds. Low mass AGB stars result in the majority of *s*-process enrichment in the ISM, despite generating a lower neutron fluence than intermediate mass stars, because the ^{13}C source is active for longer ($\sim 10^3$ years) than the ^{22}Ne source (~ 10 years, Karakas and Lattanzio 2014).

However, AGB stars are not the sole location of *s*-process nucleosynthesis. Massive rotating stars can also produce *s*-process elements. The presence of elements produced by the *s*-process in ancient halo stars and globular cluster stars indicates there is a process faster than AGB stars that releases *s*-process elements into the ISM (e.g., Travaglio et al., 2004; Chiappini et al., 2011). Rotation in low-metallicity massive stars causes mixing between the H convective shell and He core. This mixing allows the *s*-process to occur through the ^{22}Ne reaction while releasing a free neutron (as discussed above). Simulations confirm that *s*-process elements can be produced in rotating massive stars, though a rotating massive star produces $\lesssim 10$ times the second-peak neutron-capture elements produced in an AGB star (e.g., Pignatari et al., 2010; Frischknecht et al., 2016).

1.2 Narrowing Down the Search for the Dominant R-Process Origin

We will now use the results of theoretical models and observational constraints to limit our search for the dominant *r*-process origin. Specifically, core-collapse

[1]This condensed notation describes the following reactions: $^{12}C + p \rightarrow ^{13}N + \gamma$ and $^{13}N \rightarrow ^{13}C + e^+ + \nu_e$

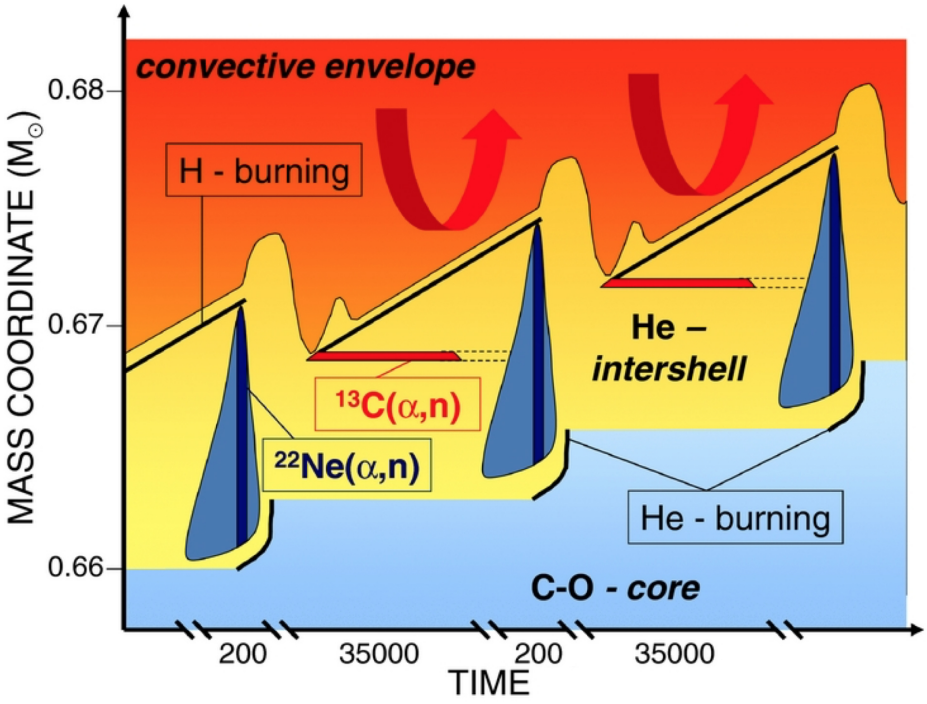

Figure 1.5: This cartoon indicates how free neutrons are created in AGB stars in the He-intershell. In low mass AGB stars, free neutrons are created from ^{13}C (red horizontal bar) for $\sim 10^3$ years. In intermediate mass AGB stars, free neutrons are created from ^{22}Ne (blue vertical bar) for ~ 10 years. Figure from Reifarth, Lederer, and Käppeler (2014).

supernovae (CCSNe), magnetorotational supernovae (MRSNe), collapsars, binary neutron star mergers (NSMs), and neutron star/black hole mergers (NS+BHs) are currently being considered (e.g., Qian and Wasserburg, 2007; Arnould, Goriely, and Takahashi, 2007; Thielemann et al., 2011; Papish, Soker, and Bukay, 2015; Liccardo et al., 2018).

In a CCSN it was thought that neutrino winds drive neutrons and protons from the surface of the proto-neutron star (located at the core), resulting in a large neutron flux in the middle region of the explosion, which might be a site of *r*-process (Meyer et al., 1992; Woosley and T. Janka, 2005). However, recent simulations have been unable to generate *r*-process elements up to or beyond barium except in extreme cases (e.g., Wanajo, 2013). This limitation on the average *r*-process yields of CCSNe provided by simulations, paired with estimates of the yield required by observations, has convincingly eliminated 'typical' CCSNe as the dominant source of the *r*-process (e.g., Macias and Ramirez-Ruiz, 2016).

However, rare types of CCSNe that produce copious amounts of *r*-process material

are still being considered as a potential source of r-process. We will discuss two types of rare CCSNe that are possible r-process origins. The first type is MRSNe. MRSNe are supernovae that start out with high magnetic fields (B$\sim 10^{12-13}$ G) that cause jet-like explosions, which may produce r-process elements. MRSNe are possibly $0.1\% - 1\%$ of all CCSNe and could produce enough r-process material to account for the observed levels of r-process enrichment found in the solar system. Some simulations have been able to reproduce the full r-process pattern seen in the solar system with only minor discrepancies, but other simulations struggle to produce third-peak neutron-capture elements (Mösta et al., 2017; Nishimura, Takiwaki, and Thielemann, 2015; Nishimura, Sawai, et al., 2017). There is currently no proof that MRSNe occur, although it is the most popular explanation for hydrogen-poor superluminous supernovae (SLSNe I, e.g., Kasen and Bildsten, 2010; De Cia et al., 2018). This lack of observational constraints means that there is also no proof that MRSNe actually produce large amounts of r-process material.

The second type of CCSNe is collapsars. As a rotating massive star collapses it launches a jet and forms an accretion disk. MRSNe occur when r-process nucleosynthesis occurs in this jet. In comparison, the collapsar model posits that the r-process occurs in the material that is ejected from the accretion disk of the newly-created black hole (Siegel, Barnes, and Metzger, 2018).

NSMs have the most complete theoretical models and easily produce a large amount of r-process material. Simulations have predicted that NSMs are able to recreate the full r-process pattern, and have shown that these results are insensitive to the detailed choices of the simulation (Côté et al., 2017). NSMs now have an observational constraint in the form of the first observed NSM (GW170817, B. P. Abbott, R. Abbott, T. D. Abbott, Acernese, et al., 2017). The discovery of the electromagnetic counterpart was originally announced by Coulter et al. (2017). Photometric and spectroscopic follow-up enabled r-process yields to be determined (e.g., Tanvir et al., 2017; Troja et al., 2017; Evans et al., 2017; Chornock et al., 2017; Kilpatrick et al., 2017). This is the first observational constraint of an r-process yield coming from a known astrophysical origin. This NSM yield is high enough for all r-process elements to be produced by NSMs. However, assuming the yield from GW170817 is representative of all NSMs could be inaccurate. Quantitative predictions for the rates, time delays, and yields are still active areas of study (e.g., Radice et al., 2016).

Some NS+BHs likely reproduce the full r-process pattern as well, but restrictions (e.g., on the black hole mass and spin) are required to eject r-process material from a

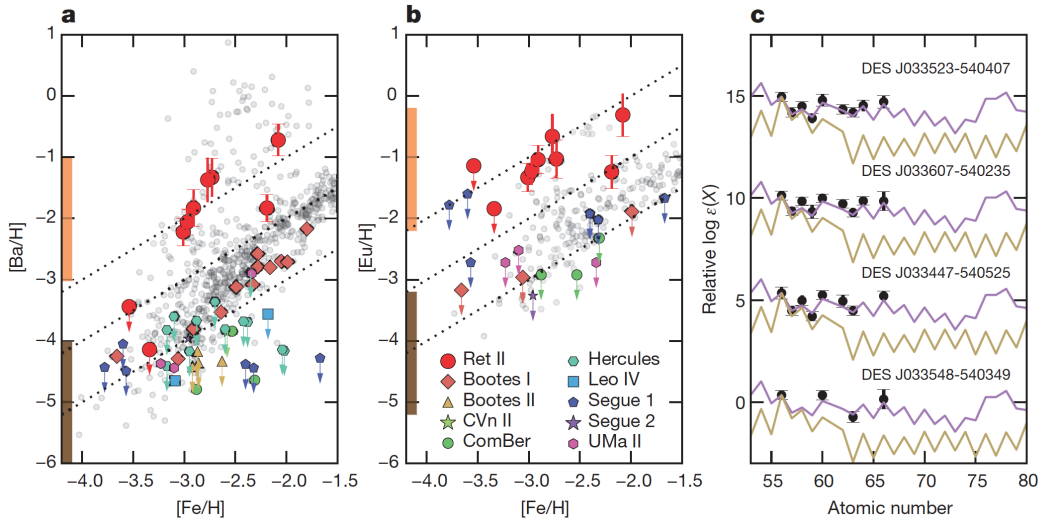

Figure 1.6: The majority of red giants measured in Reticulum II show significant barium and europium enhancement (panels a and b) due to the *r*-process (see panel c), which is consistent with a NSM. In panels a and b, Milky Way halo stars (grey circles) and other ultra-faint dwarf galaxy stars (colored symbols) are compared to Reticulum II stars. The bars represent abundance ranges expected from a NSM (orange) and CCSN (brown). Panel c shows the relative abundances of neutron-capture elements compared to the *s*- and *r*-process patterns plotted in yellow and purple, respectively. Figure from Ji et al. (2016).

NS+BHs (e.g., Lattimer and Schramm, 1974; Shibata and Taniguchi, 2011; Foucart et al., 2015; Barack et al., 2018). The subset of NS+BHs that are a source of *r*-process are expected to be much rarer than the NSMs. Therefore, the contribution of NSMs dominates over the contribution of NS+BHs.

1.3 Barium and Europium as Probes of the *r*-process

Barium is a heavy metal element that belongs to the second peak of neutron-capture elements. It has 56 protons and its neutral state has two valence electrons in a closed s-shell, which qualifies it as an alkaline earth metal.

In the solar system, 85% of barium is produced via the *s*-process (C. Sneden, Cowan, and Gallino, 2008). Barium has five stable isotopes (with masses of 134 – 138, see Figure 1.1). Shielding by stable Xe isotopes causes two Ba isotopes to be created solely by the *s*-process. The most abundant barium isotope is ^{138}Ba, which is created by both the *s*- and *r*-processes and has a closed neutron shell (N=82).

In cases where there is little AGB ejecta, barium production is dominated by the

r-process. This occurs when low and intermediate mass stars have not had time to evolve to the AGB. AGB stars with masses below $4\,M_{\odot}$ (Cristallo et al., 2015; Fishlock et al., 2014) dominate the *s*-process production of barium, which would eject barium into the ISM no earlier than 0.3 Gyrs after star formation begins. Therefore, barium can be used to study the *r*-process in stars that were born when the stellar population was very young. In practice, this is true for old, metal-poor stellar populations (e.g., the most metal-poor stars in dwarf galaxies).

For optical observers, barium is one of the easiest neutron-capture elements to measure in stellar atmospheres. Singly ionized barium happens to have five strong absorption lines that fall in the wavelength range probed by multi-object medium-resolution spectrographs (e.g., DEIMOS). These lines are 4554.0, 4934.1, 5853.7, 6141.7, and 6496.9 Å[2]. One of these lines (4934.1 Å) is blended with two iron lines even in high-resolution spectroscopy (HRS). In medium-resolution spectroscopy (MRS), 4554.0 and 6496.9 Å lines are blended with nearby Ti, Fe, and Ca lines. This leaves 5853.7 and 6141.7 Å lines as the clearest indicators of barium abundance in MRS. However, as discussed in Chapter 2, all five barium lines can be used in an abundance analysis that relies on spectral synthesis rather than the measurement of individual line strengths.

Europium is a heavy metal element that belongs to the rare earth peak of neutron-capture elements. It has 63 protons, and its neutral state has seven valence electrons in the f-shell, which qualifies it as a lanthanide.

In the solar system, 98% of europium is produced via the *r*-process (C. Sneden, Cowan, and Gallino, 2008). Europium has two stable isotopes (^{151}Eu and ^{153}Eu). ^{151}Eu is skipped by the *s*-process, because the *s*-process path travels from $^{150}\mathrm{Sm}\rightarrow{}^{151}\mathrm{Sm}\rightarrow{}^{152}\mathrm{Sm}\rightarrow{}^{153}\mathrm{Sm}\rightarrow{}^{153}\mathrm{Eu}$. Although ^{151}Sm is classified as unstable, its half-life is 90 yrs. Therefore, the *s*-process is able to pass through ^{151}Sm to eventually create a small percentage of ^{153}Eu. In all cases, europium can be used to study the *r*-process.

For optical observers, europium is difficult to measure. It is less abundant than barium (10 times less abundant in neutron-star merger simulations, Goriely, Bauswein, and H.-T. Janka 2011), which contributes to weaker absorption lines in general. There are three absorption lines that are often used to measure europium: 4129.7, 6437.6 and 6645.1 Å. Two of the lines (6437.6 and 6645.1 Å) are in a wavelength

[2]These wavelengths correspond to the following transitions of the single valence electron: $^2\mathrm{P}^0_{3/2}\rightarrow{}^2\mathrm{S}_{1/2}$, $^2\mathrm{P}^0_{1/2}\rightarrow{}^2\mathrm{S}_{1/2}$, $^2\mathrm{P}^0_{3/2}\rightarrow{}^2\mathrm{D}_{3/2}$, $^2\mathrm{P}^0_{3/2}\rightarrow{}^2\mathrm{D}_{5/2}$, and $^2\mathrm{P}^0_{1/2}\rightarrow{}^2\,\mathrm{D}_{3/2}$, respectively.

range appropriate for studying red giants with modern, ground-based spectrographs, but the lines tend to be very weak in metal-poor stars. Although some studies only use these two lines to measure europium (Worley et al., 2013), many studies (e.g., James et al. 2004) use 4129.7 Å instead, which is challenging to observe in red giants with many spectrographs, including DEIMOS. This bluer line is easily saturated and is blended in metal-rich stars. Given the scarcity of available europium lines, europium measurements are challenging in general and are not well-suited for measurements with MRS.

We have discussed that barium can be an indicator of the *s*- or *r*-process depending on the contribution of AGB stars and that europium is almost always an indicator of the *r*-process. It follows that the ratio of barium-to-europium ([Ba/Eu]) indicates the percentage of neutron-capture elements produced by the *s*- and *r*-processes. Using [Ba/Eu] as an indicator assumes that there is a consistent value of [Ba/Eu] for a pure *s*- or *r*-process source (i.e., a *s*- or *r*-process pattern). Studies of abundances of extremely metal-poor stars find that for elements in the second neutron-capture peak and heavier (A$>$ 130) there are robust *s*- and *r*-process patterns (see C. Sneden, Cowan, and Gallino 2008 for a summary). Although the total abundances of each element vary star-to-star, the ratio of heavy neutron-capture elements (typically normalizing at the barium abundance) either match the *s*- or *r*-process pattern. An example of this can be seen in the last panel of Figure 1.6, where the eight abundances heavier than barium match the *r*-process pattern in several stars. It is worth mentioning that there is significant star-to-star variation in the abundance pattern of first peak neutron-capture elements (again see C. Sneden, Cowan, and Gallino 2008 for a summary). This varying light *r*-process pattern is the main piece of observational evidence that supports a different astrophysical source for "weak" *r*-process elements (first peak) and "strong" *r*-process elements (second peak and heavier). In this thesis I focus on barium and europium as indicators of the *r*-process, so when I discuss the dominant *r*-process origin I am referring to the dominant "strong" *r*-process origin.

Examples of Using Barium and Europium to Study the *r*-process

The existence of *r*-process enrichment (often determined by the barium to europium ratio) in many extremely metal-poor ([Fe/H] < -2.5) halo stars proves that *r*-process enrichment (possibly by CCSNe) occurs before Type Ia supernovae start to explode (e.g., Honda et al., 2004). Also, the globular cluster M15 shows unusual, large *r*-process variations (more than a dex spread in [Ba/H] vs. [Eu/H]) with

constant iron abundance (Worley et al., 2013, see Chapter 5), potentially caused by a large event unevenly enriching the surrounding area. Furthermore, Ji et al. (2016) discovered a high percentage of red giants in the ultra-faint dwarf galaxy Reticulum II with dramatic *r*-process—barium and europium—enhancement (Figure 1.6). The *r*-process abundances in Reticulum II are enhanced compared to other ultra-faint dwarf galaxies, providing clear evidence for a rare event generating large amounts of *r*-process enrichment in a dwarf galaxy (e.g., a MRSN or NSM). Although these cases all have low metallicities ([Fe/H]< -2), *r*-process contributions of barium may be important even in more metal-rich environments (see Chapter 4). The majority of this thesis (Chapter 2, 3, 4 and 5) involves measuring barium and using barium to study the *r*-process in metal-poor dwarf galaxies and globular clusters. We also use [Ba/Eu] measurements from the literature to separate barium created by the *s*- and *r*-processes in Chapter 3.

1.4 Outline of this Thesis

This thesis contains several ways of studying the *r*-process origin. This thesis uses galactic archaeology with barium abundances in three different ways. Then, I present an instrumentation project that optimizes the efficiency of the Zwicky Transient Facility (ZTF). Finally, this thesis is concluded in Chapter 7.

Galactic Archaeology with Barium Abundances

The premise of galactic archaeology is that stars form out of a galaxy's gas and display the chemical composition of the gas when they were born (Tinsley, 1980). At the same time, galactic inflows, outflows, and stellar ejecta dilute or enhance the chemical composition of the star-forming gas in a galaxy. We can not watch these processes happen in real time in an individual galaxy, so instead we use galactic archaeology to learn how a given galaxy has evolved in the past.

I use galactic archaeology to determine the timescale of *r*-process enrichment by comparing barium abundances to abundances created by other well-known astrophysical sources. As discussed in Section 1.3, barium in metal-poor dwarf galaxies and globular clusters is an indicator of the *r*-process. In order to study chemical trends, we need a large sample of stellar abundances ($\gtrsim 30$), so our results are not overwhelmed by our measurement error and star-to-star variation. To achieve a large sample, we use MRS to measure barium abundances for the first time in dwarf galaxies.

Many recent technical and scientific advancements have enabled obtaining barium

abundances in individual stars in nearby galaxies. Increased CCD sensitivity has enabled spectrographs to obtain high signal-to-noise spectra of extragalactic stars ($\sim$ 80 kpc away) in a reasonable time ($\sim$ 2 hrs, Wright et al. 2003). In addition, the development of multi-object spectrographs (e.g., DEIMOS, Faber et al., 2003), where tens to hundreds of spectra can be observed simultaneously, enables the observation of a large numbers of stars. There have also been advancements in our ability to measure chemical abundances from spectra. Line lists of the atomic transitions have been incorporating results from atomic experiments and have increased the accuracy of the abundance measurements (e.g., McWilliam, 1998; Lawler et al., 2001; Ryabchikova et al., 2015). Large grids of model atmospheres (e.g., Kurucz, 1993) and codes generating synthetic spectra (e.g., C. A. Sneden, 1973) have streamlined these abundance measurements.

Chapter 2 describes how we measure barium abundances in MRS, confirms that MRS is a reliable method of measuring barium, and quantifies the errors associated with this measurement. Chapter 2 also presents the largest catalog of barium abundances ever assembled for dwarf galaxies.

Using this large catalog of barium abundances, Chapter 3 compares abundance trends in four dwarf galaxies. Using [Ba/Eu] measurements from the literature, we isolate the barium abundance created by the *r*-process. From comparing the slopes of [Mg/Fe] vs. [Fe/H] and [Ba/Fe]$_r$ vs. [Fe/H], we find that the *r*-process origin has a delayed timescale early in the history of dwarf galaxies. From this we conclude that NSMs are the dominant source of the r-process in the early evolution of dwarf galaxies.

The work in Chapter 4 also uses this large catalog of barium abundances, but Chapter 4 uses a simple galactic chemical evolution (GCE) model to match the [Mg/Fe], [Fe/H], and [Ba/Fe] abundance trends. Chapter 4 describes the model, discusses assumptions, and presents our preliminary results. The GCE model found that AGB star ejecta does not make nearly enough barium to match the observations. In order for the models to match the observed abundance trends, *r*-process elements need to be contributed with a delayed timescale. This has confirmed that NSMs are the most likely physical origin for the *r*-process in dwarf galaxies.

Chapter 5 tests whether the *r*-process material in the globular cluster M15 was formed and accreted after the stars in the cluster formed. M15 has large *r*-process abundance dispersions and is slightly *r*-process-enhanced compared to other globular clusters, including stars with [Eu/Fe] > 1 (C. Sneden, Kraft, et al., 1997). The

inhomogeneity of r-process abundances could be a result of a rare event that unevenly deposited r-process material onto the stars of M15. In new observations of stars before and after the first dredge-up, we find the barium abundances are unchanged. Therefore, we conclude that the r-process enrichment occurred before the stars were created, and this puzzle remains unsolved.

Electromagnetic Follow-up of Neutron Star Mergers

LIGO began astrophysically meaningful observations in 2015 (B. P. Abbott, R. Abbott, T. D. Abbott, Abernathy, et al., 2016). With electromagnetical follow-up of LIGO detections of NSMs, we can infer the r-process yield from a single event more directly than ever before. When LIGO discovers a NSM (B. P. Abbott, R. Abbott, T. D. Abbott, Acernese, et al., 2017), many different electromagnetic observatories are notified and given the localization that LIGO determines. At that point, the surveys scan the sky to find the transient that is associated with this NSM (i.e., its electromagnetic counterpart). The technical advancement of CCD quality has enabled large optical/IR surveys to quickly scan the sky to find the electromagnetic counterpart to the LIGO detection (Dekany et al., 2016). Advancements in image processing and machine learning (e.g., Mahabal et al., 2019) have dramatically improved the ability of these surveys to identify changing light sources (i.e., transients) in the large volume of imaging data—1 terabytes of raw uncompressed images are taken a night by ZTF (Masci et al., 2019). ZTF (and the precursor survey, PTF) participates in the electromagnetic follow-up of NSMs (Kasliwal, Cenko, et al., 2016; Kasliwal, Nakar, et al., 2017). ZTF, with its large field-of-view (47 $\deg^2$), is perfectly suited for this follow-up. Chapter 6 discusses how to optimize ZTF's efficiency by correcting CCD misalignment.

References

Abbott, B. P., R. Abbott, T. D. Abbott, M. R. Abernathy, et al. (2016). "Observation of Gravitational Waves from a Binary Black Hole Merger". In: *PhRvL* 116.6, 061102, p. 061102. DOI: 10.1103/PhysRevLett.116.061102. arXiv: 1602.03837 [gr-qc].

Abbott, B. P., R. Abbott, T. D. Abbott, F. Acernese, et al. (2017). "GW170817: Observation of Gravitational Waves from a Binary Neutron Star Inspiral". In: *Physical Review Letters* 119.16, 161101, p. 161101. DOI: 10.1103/PhysRevLett.119.161101. arXiv: 1710.05832 [gr-qc].

Arnould, M., S. Goriely, and K. Takahashi (2007). "The r-process of stellar nucleosynthesis: Astrophysics and nuclear physics achievements and mysteries".

In: *PhR* 450, pp. 97–213. DOI: 10.1016/j.physrep.2007.06.002. arXiv: 0705.4512.

Aston, F. W. (1927). "Bakerian Lecture. A New Mass-Spectrograph and the Whole Number Rule". In: *Proceedings of the Royal Society of London Series A* 115.772, pp. 487–514. DOI: 10.1098/rspa.1927.0106.

Bao, Z. Y. et al. (2000). "Neutron Cross Sections for Nucleosynthesis Studies". In: *Atomic Data and Nuclear Data Tables* 76.1, pp. 70–154. DOI: 10.1006/adnd.2000.0838.

Barack, L. et al. (2018). "Black holes, gravitational waves and fundamental physics: a roadmap". In: *ArXiv e-prints*. arXiv: 1806.05195 [gr-qc].

Beringer, J. et al. (2012). "Review of Particle Physics". In: *PhRvD* 86.1, 010001, p. 010001. DOI: 10.1103/PhysRevD.86.010001.

Burbidge, E. M. et al. (1957). "Synthesis of the Elements in Stars". In: *Reviews of Modern Physics* 29, pp. 547–650. DOI: 10.1103/RevModPhys.29.547.

Cameron, A. G. W. (1957). "Nuclear Reactions in Stars and Nucleogenesis". In: *PASP* 69.408, p. 201. DOI: 10.1086/127051.

Chiappini, Cristina et al. (2011). "Imprints of fast-rotating massive stars in the Galactic Bulge". In: *Nature* 474.7353, p. 666. DOI: 10.1038/nature10185.

Chornock, R. et al. (2017). "The Electromagnetic Counterpart of the Binary Neutron Star Merger LIGO/Virgo GW170817. IV. Detection of Near-infrared Signatures of r-process Nucleosynthesis with Gemini-South". In: *ApJL* 848.2, L19, p. L19. DOI: 10.3847/2041-8213/aa905c. arXiv: 1710.05454 [astro-ph.HE].

Côté, B. et al. (2017). "Advanced LIGO Constraints on Neutron Star Mergers and r-process Sites". In: *ApJ* 836, 230, p. 230. DOI: 10.3847/1538-4357/aa5c8d. arXiv: 1610.02405.

Coulter, D. A. et al. (2017). "Swope Supernova Survey 2017a (SSS17a), the optical counterpart to a gravitational wave source". In: *Science* 358, pp. 1556–1558. DOI: 10.1126/science.aap9811. arXiv: 1710.05452 [astro-ph.HE].

Cristallo, S. et al. (2015). "Evolution, Nucleosynthesis, and Yields of AGB Stars at Different Metallicities. III. Intermediate-mass Models, Revised Low-mass Models, and the ph-FRUITY Interface". In: *ApJS* 219, 40, p. 40. DOI: 10.1088/0067-0049/219/2/40. arXiv: 1507.07338 [astro-ph.SR].

De Cia, A. et al. (2018). "Light Curves of Hydrogen-poor Superluminous Supernovae from the Palomar Transient Factory". In: *ApJ* 860, 100, p. 100. DOI: 10.3847/1538-4357/aab9b6.

Dekany, Richard et al. (2016). "The Zwicky Transient Facility Camera". In: *Proc. SPIE*. Vol. 9908. Society of Photo-Optical Instrumentation Engineers (SPIE) Conference Series, p. 99085M. DOI: 10.1117/12.2234558.

Eddington, A. S. (1920). "The Internal Constitution of the Stars". In: *The Scientific Monthly* 11.4, pp. 297–303. ISSN: 00963771. URL: http://www.jstor.org/stable/6491.

Evans, P. A. et al. (2017). "Swift and NuSTAR observations of GW170817: Detection of a blue kilonova". In: *Science* 358, pp. 1565–1570. DOI: 10.1126/science.aap9580. arXiv: 1710.05437 [astro-ph.HE].

Faber, S. M. et al. (2003). "The DEIMOS spectrograph for the Keck II Telescope: integration and testing". In: *Instrument Design and Performance for Optical/Infrared Ground-based Telescopes*. Ed. by M. Iye and A. F. M. Moorwood. Vol. 4841. Proc. SPIE, pp. 1657–1669. DOI: 10.1117/12.460346.

Fishlock, C. K. et al. (2014). "Evolution and Nucleosynthesis of Asymptotic Giant Branch Stellar Models of Low Metallicity". In: *ApJ* 797, 44, p. 44. DOI: 10.1088/0004-637X/797/1/44. arXiv: 1410.7457 [astro-ph.SR].

Foucart, F. et al. (2015). "Post-merger evolution of a neutron star-black hole binary with neutrino transport". In: *PhRvD* 91.12, 124021, p. 124021. DOI: 10.1103/PhysRevD.91.124021. arXiv: 1502.04146 [astro-ph.HE].

Frischknecht, U. et al. (2016). "s-process production in rotating massive stars at solar and low metallicities". In: *MNRAS* 456, pp. 1803–1825. DOI: 10.1093/mnras/stv2723. arXiv: 1511.05730 [astro-ph.SR].

Goriely, S., A. Bauswein, and H.-T. Janka (2011). "r-process Nucleosynthesis in Dynamically Ejected Matter of Neutron Star Mergers". In: *ApJL* 738, L32, p. L32. DOI: 10.1088/2041-8205/738/2/L32. arXiv: 1107.0899 [astro-ph.SR].

Honda, S. et al. (2004). "Spectroscopic Studies of Extremely Metal-Poor Stars with the Subaru High Dispersion Spectrograph. II. The r-Process Elements, Including Thorium". In: *ApJ* 607, pp. 474–498. DOI: 10.1086/383406. eprint: astro-ph/0402298.

Huggins, William (1864). "On the Spectra of Some of the Chemical Elements". In: *Philosophical Transactions of the Royal Society of London Series I* 154, pp. 139–160.

James, G. et al. (2004). "Heavy elements and chemical enrichment in globular clusters". In: *A&A* 427, pp. 825–838. DOI: 10.1051/0004-6361:20041512. eprint: astro-ph/0408330.

Ji, A. P. et al. (2016). "R-process enrichment from a single event in an ancient dwarf galaxy". In: *Nature* 531, pp. 610–613. DOI: 10.1038/nature17425. arXiv: 1512.01558.

Karakas, A. I. and J. C. Lattanzio (2014). "The Dawes Review 2: Nucleosynthesis and Stellar Yields of Low- and Intermediate-Mass Single Stars". In: *PASA* 31, e030, e030. DOI: 10.1017/pasa.2014.21. arXiv: 1405.0062 [astro-ph.SR].

Kasen, D. and L. Bildsten (2010). "Supernova Light Curves Powered by Young Magnetars". In: *ApJ* 717, pp. 245–249. DOI: 10.1088/0004-637X/717/1/245. arXiv: 0911.0680 [astro-ph.HE].

Kasliwal, M. M., S. B. Cenko, et al. (2016). "iPTF Search for an Optical Counterpart to Gravitational-wave Transient GW150914". In: *ApJL* 824, L24, p. L24. DOI: 10.3847/2041-8205/824/2/L24. arXiv: 1602.08764 [astro-ph.IM].

Kasliwal, M. M., E. Nakar, et al. (2017). "Illuminating gravitational waves: A concordant picture of photons from a neutron star merger". In: *Science* 358.6370, pp. 1559–1565. DOI: 10.1126/science.aap9455. arXiv: 1710.05436 [astro-ph.HE].

Kilpatrick, C. D. et al. (2017). "Electromagnetic evidence that SSS17a is the result of a binary neutron star merger". In: *Science* 358.6370, pp. 1583–1587. DOI: 10.1126/science.aaq0073. arXiv: 1710.05434 [astro-ph.HE].

Kurucz, R. (1993). "ATLAS9 Stellar Atmosphere Programs and 2 km/s grid." In: *ATLAS9 Stellar Atmosphere Programs and 2 km/s grid. Kurucz CD-ROM No. 13. Cambridge, Mass.: Smithsonian Astrophysical Observatory, 1993.* 13.

Lattimer, J. M. and D. N. Schramm (1974). "Black-hole-neutron-star collisions". In: *ApJL* 192, pp. L145–L147. DOI: 10.1086/181612.

Lawler, J. E. et al. (2001). "Improved Laboratory Transition Parameters forEu II and Application to the Solar Europium Elemental and Isotopic Composition". In: *ApJ* 563.2, pp. 1075–1088. DOI: 10.1086/323407.

Liccardo, V. et al. (2018). "Nuclear processes in Astrophysics: Recent progress". In: *ArXiv e-prints*. arXiv: 1805.10183 [astro-ph.SR].

Macias, P. and E. Ramirez-Ruiz (2016). "A Stringent Limit on the Mass Production Rate of *r*-Process Elements in the Milky Way". In: *ArXiv e-prints*. arXiv: 1609.04826 [astro-ph.HE].

Mahabal, Ashish et al. (2019). "Machine Learning for the Zwicky Transient Facility". In: *PASP* 131.997, p. 038002. DOI: 10.1088/1538-3873/aaf3fa. arXiv: 1902.01936 [astro-ph.IM].

Masci, Frank J. et al. (2019). "The Zwicky Transient Facility: Data Processing, Products, and Archive". In: *PASP* 131.995, p. 018003. DOI: 10.1088/1538-3873/aae8ac. arXiv: 1902.01872 [astro-ph.IM].

McWilliam, A. (1998). "Barium Abundances in Extremely Metal-poor Stars". In: *AJ* 115, pp. 1640–1647. DOI: 10.1086/300289.

Meyer, B. S. et al. (1992). "R-Process Nucleosynthesis in the High-Entropy Supernova Bubble". In: *ApJ* 399, p. 656. DOI: 10.1086/171957.

Mösta, P. et al. (2017). "R-process Nucleosynthesis from Three-Dimensional Magnetorotational Core-Collapse Supernovae". In: *ArXiv e-prints*. arXiv: 1712.09370 [astro-ph.HE].

Mumpower, Matthew R., G. C. McLaughlin, and Rebecca Surman (2012). "THE RARE EARTH PEAK: AN OVERLOOKEDr-PROCESS DIAGNOSTIC". In: *The Astrophysical Journal* 752.2, p. 117. DOI: 10.1088/0004-637x/752/2/117. URL: https://doi.org/10.1088%2F0004-637x%2F752%2F2%2F117.

Nishimura, N., H. Sawai, et al. (2017). "The Intermediate r-process in Core-collapse Supernovae Driven by the Magneto-rotational Instability". In: *ApJL* 836.2, L21, p. L21. DOI: 10.3847/2041-8213/aa5dee. arXiv: 1611.02280 [astro-ph.HE].

Nishimura, N., T. Takiwaki, and F.-K. Thielemann (2015). "The r-process Nucleosynthesis in the Various Jet-like Explosions of Magnetorotational Core-collapse Supernovae". In: *ApJ* 810, 109, p. 109. DOI: 10.1088/0004-637X/810/2/109. arXiv: 1501.06567 [astro-ph.SR].

Papish, Oded, Noam Soker, and Inbal Bukay (2015). "Ejecting the envelope of red supergiant stars with jets launched by an inspiralling neutron star". In: *MNRAS* 449.1, pp. 288–295. DOI: 10.1093/mnras/stv345.

Pignatari, M. et al. (2010). "The Weak s-Process in Massive Stars and its Dependence on the Neutron Capture Cross Sections". In: *ApJ* 710.2, pp. 1557–1577. DOI: 10.1088/0004-637X/710/2/1557.

Qian, Y. -Z. and G. J. Wasserburg (2007). "Where, oh where has the r-process gone?" In: *PhR* 442.1-6, pp. 237–268. DOI: 10.1016/j.physrep.2007.02.006. arXiv: 0708.1767 [astro-ph].

Radice, D. et al. (2016). "Dynamical mass ejection from binary neutron star mergers". In: *MNRAS* 460, pp. 3255–3271. DOI: 10.1093/mnras/stw1227. arXiv: 1601.02426 [astro-ph.HE].

Reifarth, R., C. Lederer, and F. Käppeler (2014). "Neutron reactions in astrophysics". In: *Journal of Physics G Nuclear Physics* 41.5, 053101, p. 053101. DOI: 10.1088/0954-3899/41/5/053101. arXiv: 1403.5670 [astro-ph.IM].

Ryabchikova, T. et al. (2015). "A major upgrade of the VALD database". In: *PhyS* 90.5, 054005, p. 054005. DOI: 10.1088/0031-8949/90/5/054005.

Shibata, M. and K. Taniguchi (2011). "Coalescence of Black Hole-Neutron Star Binaries". In: *Living Reviews in Relativity* 14, 6, p. 6. DOI: 10.12942/lrr-2011-6.

Siegel, D. M., J. Barnes, and B. D. Metzger (2018). "The neutron star merger GW170817 points to collapsars as the main r-process source". In: *arXiv e-prints*. arXiv: 1810.00098 [astro-ph.HE].

Sneden, C. A. (1973). "Carbon and Nitrogen Abundances in Metal-Poor Stars." PhD thesis. THE UNIVERSITY OF TEXAS AT AUSTIN.

Sneden, C., J. J. Cowan, and R. Gallino (2008). "Neutron-Capture Elements in the Early Galaxy". In: *ARA&A* 46, pp. 241–288. DOI: 10.1146/annurev.astro.46.060407.145207.

Sneden, C., R. P. Kraft, et al. (1997). "Star-To-Star Abundance Variations Among Bright Giants in the Metal-Poor Globular Cluster M15". In: *AJ* 114, p. 1964. DOI: 10.1086/118618.

Suess, Hans E. and Harold C. Urey (1956). "Abundances of the Elements". In: *Rev. Mod. Phys.* 28 (1), pp. 53–74. DOI: 10.1103/RevModPhys.28.53. URL: https://link.aps.org/doi/10.1103/RevModPhys.28.53.

Tanvir, N. R. et al. (2017). "The Emergence of a Lanthanide-rich Kilonova Following the Merger of Two Neutron Stars". In: *ApJL* 848, L27, p. L27. DOI: 10.3847/2041-8213/aa90b6. arXiv: 1710.05455 [astro-ph.HE].

Thielemann, F.-K. et al. (2011). "What are the astrophysical sites for the r-process and the production of heavy elements?" In: *Progress in Particle and Nuclear Physics* 66, pp. 346–353. DOI: 10.1016/j.ppnp.2011.01.032.

Tinsley, B. M. (1980). "Evolution of the Stars and Gas in Galaxies". In: *FCPh* 5, pp. 287–388.

Travaglio, Claudia et al. (2004). "Galactic Evolution of Sr, Y, And Zr: A Multiplicity of Nucleosynthetic Processes". In: *ApJ* 601.2, pp. 864–884. DOI: 10.1086/380507. arXiv: astro-ph/0310189 [astro-ph].

Troja, E. et al. (2017). "The X-ray counterpart to the gravitational-wave event GW170817". In: *Nature* 551, pp. 71–74. DOI: 10.1038/nature24290. arXiv: 1710.05433 [astro-ph.HE].

Wanajo, S. (2013). "The r-process in Proto-neutron-star Wind Revisited". In: *ApJL* 770, L22, p. L22. DOI: 10.1088/2041-8205/770/2/L22. arXiv: 1305.0371 [astro-ph.SR].

Wapstra, A. H. and G. Audi (1985). "The 1983 atomic mass evaluation (I). Atomic mass table". In: *NuPhA* 432.1, pp. 1–54. DOI: 10.1016/0375-9474(85)90283-0.

Woosley, S. and T. Janka (2005). "The physics of core-collapse supernovae". In: *Nature Physics* 1, pp. 147–154. DOI: 10.1038/nphys172. eprint: astro-ph/0601261.

Worley, C. C. et al. (2013). "Ba and Eu abundances in M 15 giant stars". In: *A&A* 553, A47, A47. DOI: 10.1051/0004-6361/201321097. arXiv: 1302.6122 [astro-ph.SR].

Wright, Christopher A. et al. (2003). "CCD imaging systems for DEIMOS". In: *Proc. SPIE*. Ed. by Masanori Iye and Alan F. M. Moorwood. Vol. 4841. Society of Photo-Optical Instrumentation Engineers (SPIE) Conference Series, pp. 214–229. DOI: 10.1117/12.461881.

Chapter 2

MEASURING BARIUM ABUNDANCES IN DWARF GALAXIES USING MEDIUM-RESOLUTION SPECTRA FOR THE FIRST TIME

Duggan, G. E. et al. (2018). "Neutron Star Mergers are the Dominant Source of the r-process in the Early Evolution of Dwarf Galaxies". In: *Astrophysical Journal* 869, 50, p. 50. DOI: 10.3847/1538-4357/aaeb8e. arXiv: 1809.04597.

The following tables and figures have been updated from their published forms to include a recent published catalog (Hill et al., 2019): Tables 2.8 and 2.9 (machine-readable form only) and Figures 2.3 and 2.4.

2.1 Introduction

A large number of stars is needed to distinguish the chemical trend of a stellar population from star-to-star variations. We were able to obtain a large sample of stars, because we used multi-object, medium-resolution spectroscopy (MRS, R $\approx 5,000$). Typically barium is measured using high-resolution spectroscopy (HRS, R $> 20,000$) on single-slit spectrographs. Traditionally, precise chemical abundance measurements required equivalent width measurements of absorption lines in HRS, and because of this the Dwarf Abundances and Radial velocities Team (DART; Tolstoy et al., 2006) invested the necessary observing time to obtain HRS for tens of individual stars in Sculptor and Fornax (e.g., Lemasle et al., 2014; Starkenburg et al., 2013). To obtain a large sample of stars with moderate observing time, we used MRS which enables tens of member stars to be observed simultaneously.

The main weakness of MRS is increased line blending. The blending that occurs in MRS causes strong sky lines to contaminate a larger range of wavelengths, the continuum to be obscured, and the apparent weakening of absorption lines. Since blending prevents the continuum from being measured in the gaps between absorption/emission lines, the continuum is iteratively fitted while the abundances are measured using the synthetic spectra.

We overcome these weaknesses to take advantage of higher S/N per pixel or fainter limiting magnitude that can be achieved with a given amount of observation time ($V \lesssim 20$ mag compared to 18 mag for HRS), which increases the sample of ob-

Table 2.1: Spectroscopic Targets

Target	R.A. (J2000)	Decl. (J2000)	D (kpc)	$(m-M)_0$[a] (mag)
		Globular Clusters		
NGC 2419	$07^h38^m09^s$	$+38°52'55''$	82.6	19.83
NGC 4590 (M68)	$12^h39^m28^s$	$-26°44'39''$	10.3	15.21
NGC 6341 (M92)	$17^h17^m07^s$	$+43°8'11''$	8.3	14.65
NGC 7078 (M15)	$21^h29^m58^s$	$+12°10'1''$	10.4	15.39
		Halo Field Stars		
BD +14 550	$03^h18^m27^s$	$+15°10'38''$		
BD −00 552	$03^h28^m54^s$	$-00°25'3''$		
BD +22 626	$04^h04^m11^s$	$+23°24'27''$		
BD −13 942	$04^h38^m56^s$	$-13°20'48''$		
BD −14 1399	$06^h18^m49^s$	$-14°50'43''$		
BD +62 959	$07^h54^m29^s$	$+62°8'11''$		
BD +80 245	$08^h11^m06^s$	$+79°54'30''$		
BD +21 1969	$09^h06^m43^s$	$+20°30'36''$		
BD −20 2955	$09^h36^m20^s$	$-20°53'15''$		
BD +55 1362	$10^h04^m43^s$	$+54°20'43''$		
BD +54 1359	$10^h14^m29^s$	$+53°33'39''$		
BD +40 2408	$11^h13^m55^s$	$+39°58'40''$		
BD −04 3155	$11^h51^m50^s$	$-05°45'44''$		
BD +49 2098	$11^h58^m00^s$	$+48°12'12''$		
BD +09 2653	$12^h40^m14^s$	$+08°31'38''$		
		dSphs		
Sculptor	$01^h00^m09^s$	$-33°42'32''$	85	19.67
Fornax	$02^h39^m59^s$	$-34°26'57''$	139	20.72
Sextans	$10^h13^m03^s$	$-01°36'52''$	95	19.90
Ursa Minor	$15^h09^m11^s$	$+67°12'52''$	69	19.18
Draco	$17^h20^m19^s$	$+57°54'48''$	92	19.84

Notes.
[a] Extinction-corrected distance modulus.
References. See Harris (1996, 2010 edition, http://www.physics.mcmaster.ca/~harris/mwgc.dat) and references therein for the coordinates and distances for the globular clusters. Halo field stars coordinates are from Fulbright (2000). The remaining dSph coordinates are adopted from Mateo (1998), and the distances are adopted from the following sources: Sculptor, Pietrzyński et al. (2008); Fornax, Rizzi et al. (2007); Sextans, M. G. Lee et al. (2003); Ursa Minor, Mighell and Burke (1999); Draco, Bellazzini et al. (2002).

servable red giant branch stars. Wider spectral coverage increases the number of absorption lines observed per chemical element, which is especially important for elements with few clear absorption lines (e.g., neutron-capture elements). For barium, we use five different absorption lines in our measurements.

Both HRS and MRS require a stellar atmosphere model and stellar line analysis—either to measure abundances from equivalent widths or to generate synthetic spectra. Common simplifications for both methods are to use a one-dimensional (1D) stellar atmosphere model and to assume local thermodynamic equilibrium (LTE) throughout the star. Correcting for 3D and non-LTE effects could systematically shift barium abundance measurements by 0.1–0.3 dex (see Section 2.7), similar to the statistical uncertainties of our measurements. Unfortunately, both of these corrections are very computationally intensive and are beyond the scope of this project.

Determining chemical abundances from MRS has returned uncertainties as low as 0.1 dex for iron and α elements in dwarf galaxies (Kirby, Guhathakurta, Simon, et al., 2010). This chapter will demonstrate that we can also achieve similar uncertainties for barium abundances in dwarf galaxies. Therefore, we are able to use a multi-object spectrographs MRS without sacrificing accuracy to obtain barium abundances for a large sample of stars.

2.2 Observations

We observed a diverse sample of dwarf galaxies to probe what [Ba/Fe] measurements can tell us about the chemical enrichment mechanisms and star formation histories (SFHs) in different galaxies. Our sample includes five classical dwarf spheroidal galaxies: Fornax, Sculptor, Sextans, Draco, and Ursa Minor. These galaxies span a variety of masses ($M_* \sim 10^5 - 10^7\ M_\odot$) and durations of star formation ($\approx$ 1–11 Gyr of star formation, Weisz et al. 2014). In each of these galaxies we obtained MRS for individual red giant branch stars using DEIMOS on Keck II.

Apart from these galaxies, we also observed red giant branch stars in globular clusters and the halo of the Milky Way to compare our [Ba/Fe] measurements to those found in the literature. This comparison is used to estimate our systematic error (see Section 2.7).

The locations and distances to all spectroscopic targets are listed in Table 2.1. The details of all observations contained in this chapter are given in Table 2.2. This includes the name of the slitmask, number of slits, date, airmass, seeing, and

Table 2.2: DEIMOS Observations

Object	Slitmask	Reference[a]	No. Targets	Date	Airmass	Seeing	Exposures
			Globular Clusters				
NGC 2419[b]	n2419b	Kirby et al. (2016)	112	2012 Mar 19	1.07	0.″74	3 × 900 s
NGC 4590 (M68)[b]	n4590a	Kirby et al. (2016)	96	2014 Feb 2	1.60	0.″80	1200 s, 937 s
NGC 6341 (M92)	6341l1	Kirby et al. (2016)	177	2017 Mar 28	1.20	0.″71	6 × 1800 s, 2000 s
NGC 7078 (M15)[b]	n7078d	Kirby et al. (2016)	164	2011 Jul 29	1.03	1.″10	3 × 600 s
	n7078e	Kirby et al. (2016)	167	2011 Jul 30	1.05	0.″86	3 × 900 s
			Halo Field Stars				
BD +14 550	LVMslits	Fulbright (2000)	1	2016 Dec 30	1.18	> 1.″5	300 s
BD −00 552	LVMslits	Fulbright (2000)	1	2016 Dec 30	1.14	> 1.″5	600 s
BD +22 626	LVMslits	Fulbright (2000)	1	2016 Dec 30	1.05	> 1.″5	600 s
BD −13 942	LVMslits	Fulbright (2000)	1	2016 Dec 30	1.20	> 1.″5	300 s
BD −14 1399	LVMslits	Fulbright (2000)	1	2016 Dec 30	1.26	> 1.″5	2 × 300 s
BD +62 959	LVMslits	Fulbright (2000)	1	2016 Dec 30	1.35	> 1.″5	300 s
BD +80 245	LVMslits	Fulbright (2000)	1	2016 Dec 30	1.99	> 1.″5	2 × 600 s
BD +21 1969	LVMslits	Fulbright (2000)	1	2016 Dec 30	1.12	> 1.″5	300 s
BD −20 2955	LVMslits	Fulbright (2000)	1	2016 Dec 30	1.35	> 1.″5	300 s

Continued on next page

Table 2.2 – *Continued from previous page*

Object	Slitmask	Reference[a]	No. Targets	Date	Airmass	Seeing	Exposures
BD +55 1362	LVMslits	Fulbright (2000)	1	2016 Dec 30	1.26	> 1.″5	2 × 300 s
BD +54 1359	LVMslits	Fulbright (2000)	1	2016 Dec 30	1.28	> 1.″5	2 × 300 s
BD +40 2408	LVMslits	Fulbright (2000)	1	2016 Dec 30	1.08	> 1.″5	300 s
BD −04 3155	LVMslits	Fulbright (2000)	1	2016 Dec 30	1.32	> 1.″5	300 s
BD +49 2098	LVMslits	Fulbright (2000)	1	2016 Dec 30	1.18	> 1.″5	300 s
BD +09 2653	LVMslits	Fulbright (2000)	1	2016 Dec 30	1.25	> 1.″5	300 s
			dSphs				
Sculptor[b]	bscl1	Kirby et al. (2009)	86	2011 Jul 31	1.72	0.″75	4 × 1200 s, 900 s
	bscl2	Kirby et al. (2009)	106	2011 Aug 6	1.82	0.″74	2 × 1200 s, 2 × 840 s
	bscl6	Kirby et al. (2009)	91	2011 Aug 4	1.72	0.″83	4 × 1200 s
Fornax[b]	bfor6	Kirby et al. (2010)	169	2011 Aug 5	1.86	1.″26	2 × 800 s
				2011 Aug 6	1.83	0.″76	1200 s
				2011 Aug 7	1.90	0.″83	3 × 1200 s
Sextans	bsex2	Kirby et al. (2010)	85	2016 Jan 30	1.10	...	2 × 1800 s
				2016 Jan 31	1.11	...	2 × 1800 s, 1000 s
	bsex3	Kirby et al. (2010)	85	2016 Jan 29	1.55	...	6 × 1550 s

Continued on next page

Table 2.2 – *Continued from previous page*

Object	Slitmask	Reference[a]	No. Targets	Date	Airmass	Seeing	Exposures
Ursa Minor[b]	bumi1	Kirby et al. (2010)	125	2011 Jul 29	1.52	0.″57	600 s, 4 × 1200 s
	bumi2	Kirby et al. (2010)	134	2011 Jul 31	1.68	0.″73	4 × 1200 s
	bumi3	Kirby et al. (2010)	137	2011 Aug 4	1.80	0.″64	4 × 1200 s
Draco[b]	bdra1	Kirby et al. (2010)	151	2011 Jul 30	1.42	1.″18	5 × 1200 s
	bdra2	Kirby et al. (2010)	167	2011 Aug 7	1.28	0.″67	4 × 1200 s
	bdra3	Kirby et al. (2010)	140	2011 Aug 5	1.37	0.″98	5 × 1200 s

Notes.

[a] This is the reference for the slitmask design (when applicable), star selection, and membership verification.

[b] These observations were originally published in Kirby et al. (2015).

exposure time of all observations. This table also includes references for star selection and membership verification.

Star Selection and Member Verification

We relied on the star selection, member verification, and stellar parameters found in the literature. The details of how these stars were selected and how membership was determined are found in the references listed in Table 2.2. Here we outline these methods in two groups, which are separated by the concentration of the desired stars: targets observed with A) multi-object or B) single-object slitmasks.

A) Multi-object slitmasks were used to observe all dwarf galaxies and globular clusters. In general, multi-object slitmasks were designed using the dsimulator software package[1]. Stars were prioritized to be included on the slitmask based on their overall brightness and the likelihood they are on the red giant branch—determined using their surface gravity ($\log g$) and position on the color–magnitude diagram. The stars were then verified as members of the galaxy or globular cluster based on radial velocity measurements.

B) Single slit spectroscopy was used to obtain observations of Milky Way halo stars. Halo stars were selected from Fulbright (2000), who verified that the stars belonged to the Milky Way halo using proper motion measurements. To exclude dwarf stars from our sample, we applied an additional constraint by only including stars with $\log g < 3.6$, adopting Fulbright's measurements of surface gravity.

Spectroscopic Configuration and Reduction

Previous work (e.g., Kirby, Guhathakurta, Simon, et al. 2010) utilized the 1200 lines mm^{-1} DEIMOS grating from 6400–9000 Å (with a spectral resolution of $R \approx 6500$ at 8500 Å with 0.″7 slits). However, the optical barium absorption lines are bluer (4554–6497 Å) than can be observed efficiently with this grating, which has a blaze wavelength of 7760 Å. Therefore, to measure individual barium abundances for each star, we chose a lower resolution grating that allowed bluer wavelengths to be observed. We used the 900ZD DEIMOS grating (900 lines mm^{-1}), which has a blaze wavelength of 5500 Å. This configuration can yield up to 80–150 spectra per slitmask with medium resolution ($\approx$ 1.96 Å FWHM or R $\approx$ 2550 at 5000 Å with 0.″7 slits). A central wavelength of 5500 Å coupled with an order-blocking filter (GG400) results in a spectral range of 4000–7200 Å. Kr, Ne, Ar, and Xe arc lamps

[1] https://www2.keck.hawaii.edu/inst/deimos/dsim.html

Table 2.3: Adopted Solar Composition

Element	(X/H) = 12 + log ϵ_X
Mg	7.58
Fe	7.52
Ba	2.13
Eu	0.51

Note. Solar abundances are from Anders and Grevesse (1989), except for iron which is from C. Sneden, Kraft, Prosser, et al. (1992). Elemental abundance is defined as: (X/H) = 12 + log ϵ_X = 12 + log(n_X) − log(n_H).

were used for wavelength calibration, and a quartz lamp was used for flat fielding.

We reduced all observations using the `spec2d` pipeline (Newman et al., 2013; Cooper et al., 2012). This pipeline automatically determines the wavelength solution using the spectral arcs. However, these wavelength solutions were not sufficiently accurate, because the arc lamps have few detectable emission lines with wavelengths less than $\approx$ 5000 Å at the exposure times that we used. To improve the wavelength solution, synthetic spectra were generated and cross-correlated against the observed spectra at Hα, $H\beta$, and Hγ in windows of 20Å. A line was fit to establish the wavelength correction ($\Delta\lambda$) as a function of wavelength (λ). This solution precludes the ability to measure absolute radial velocities, but our only focus for this work is to measure barium abundances.

We corrected for the global continuum by first fitting a spline to the observed spectrum with a break point every 200 pixels (88 Å) with an upper and lower threshold of 5σ and 0.1σ, respectively. Then, we divided the observed spectrum by the resulting spline fit to correct for the global continuum. We later refine the local continuum determination during the barium abundance measurements (Section 2.5).

2.3 Stellar Parameters

We measure barium abundances by first adopting stellar parameter measurements found in the literature, specifically the effective temperature ($T_{\rm eff}$), surface gravity (log g), metallicity ([Fe/H]), and α-to-iron ratio ([α/Fe]). Abundances presented in this chapter are referenced to solar (e.g., [Fe/H] = $(\mathrm{Fe/H})_* - (\mathrm{Fe/H})_\odot$). Our definition of the solar elemental abundances can be found in Table 2.3.

For dwarf galaxies and globular clusters, we adopted the parameter measurements from Kirby, Guhathakurta, Simon, et al. (2010) and Kirby, Guhathakurta, Zhang, et al. (2016), respectively. See Kirby, Guhathakurta, Simon, et al. (2010) and Kirby, Guhathakurta, Zhang, et al. (2016) for a full description of those measurements, which we briefly summarize here. The surface gravity and initial value of $T_{\rm eff}$ were estimated from photometry. Then $T_{\rm eff}$, [Fe/H], and [α/Fe] were measured by matching the synthetic spectra to the observed spectra. The microturbulent velocity (ξ) of the stellar atmosphere was calculated from the surface gravity (Equation 2.1)[2].

$$\xi(\mathrm{km\,s^{-1}}) = (2.13 \pm 0.05) - (0.23 \pm 0.03) \log g \tag{2.1}$$

For Milky Way halo stars, we adopted $T_{\rm eff}$, $\log g$, [Fe/H], and [α/Fe] found by Fulbright (2000). As with the globular cluster and dwarf galaxy stars, the [α/Fe] used is the average abundance measured for α elements (i.e., Mg, Si, Ca, and Ti). We replaced the microturbulent velocity published by Fulbright (2000) with the results from Equation 2.1. We shifted the spectra to the rest frame based on the radial velocity measurements found by Fulbright (2002) before fine-tuning the wavelength solution using the Balmer lines (as described in Section 2.2).

Now that we have discussed the sources of $T_{\rm eff}$, $\log g$, [Fe/H], and [α/Fe], we will describe how we measure [Ba/Fe] from our DEIMOS observations using synthetic spectra.

2.4 Synthetic Spectra

Synthetic spectra were calculated for each combination of stellar parameters to measure [Ba/Fe] from −2.0 to 1.0 dex. Table 2.4 outlines our spectral grid by listing the range and step size for each parameter used to generate the synthetic spectra. For stars that had [Ba/Fe] above 1.0 dex or below −2.0 dex, we computed additional synthetic spectra as needed.

To measure [Ba/Fe], we only needed short segments (20 Å) of synthetic spectra centered at five optical barium absorption lines: 4554.0, 4934.2, 5853.7, 6141.7, and 6496.9 Å.

MOOG (a spectral synthesis code, C. A. Sneden, 1973; C. Sneden, Bean, et al., 2012) generates synthetic spectra for a set of parameters assuming local thermal

[2]This formula for the microturbulent velocities is described by Kirby, Guhathakurta, Bolte, et al. (2009), who derived it by fitting spectroscopically measured microturbulent velocities and surface gravities from red giant branch stars in globular clusters in the literature.

Table 2.4: Barium Synthetic Spectra Grid

Parameter	Minimum Value	Maximum Value	Step
$T_{\rm eff}$ (K)	3500	5600	100
	5600	8000	200
$\log g$ (g in cm s^{-2})	0.0 ($T_{\rm eff} <$ 7000 K)	5.0	0.5
	0.5 ($T_{\rm eff} \geq$ 7000 K)	5.0	0.5
[Fe/H]	−5.0	0.0	0.1
[α/Fe]	−0.8	1.2	0.1
[Ba/Fe]	−2.0	1.0	0.1

equilibrium (LTE). We modified the 2014 version of MOOG to reduce the computation time by stripping out all functionality except the spectral synthesis routine and by parallelizing it. MOOG relies on a stellar atmosphere model and a list of atomic and molecular absorption lines (i.e., line list).

We used ATLAS9 (R. Kurucz, 1993), a collection of 1-dimensional plane-parallel stellar atmosphere models, which were interpolated to match our fine spectral grid (see Kirby, Guhathakurta, Bolte, et al. 2009 for more details). Stellar atmosphere models with matching [α/Fe] were used to calculate the synthetic spectra because α elements are a significant source of free electrons, which affect the opacity and therefore the atmospheric structure.

Line List

The line list used to calculate the synthetic spectra was compiled from a few different sources. The bulk of the line list was generated using the Vienna Atomic Line Database (VALD, Ryabchikova et al., 2015), which includes atomic lines and CH, MgH, SiH, and C_2 molecular lines. In addition, CN lines were included from C. Sneden, Lucatello, et al. (2014). To avoid unnecessary computation time, we only included lines of neutral and singly ionized species with excitation potentials less than 10 eV and oscillator strengths ($\log gf$) greater than −5.0. The format of the line list can be seen in Table 2.5. For each absorption line, the species, wavelength, excitation potential, and $\log gf$ are listed.

The line list was calibrated against spectra of the Sun and Arcturus to ensure the synthetic spectra match high quality (R≈150,000 with S/N≈1,000) observed spec-

Table 2.5: Spectral Line List

Species	Wavelength (Å)	Excitation Potential (eV)	$\log gf$
V I	4543.0096	2.7080	-2.712
Sc I	4543.0282	2.2957	-4.032
Cr I	4543.0796	5.2394	-2.972
CN	4543.0821	0.4159	-4.012
C_2	4543.0891	1.9158	-4.781
CN	4543.1178	0.9947	-2.429
CN	4543.1190	0.9947	-2.583
CN	4543.1226	0.9947	-3.730
Ti I	4543.1393	3.4238	-3.781
S I	4543.1789	9.4169	-2.534

Note. The first ten lines of the line list are shown here. The line list is published in its entirety in the correct format for MOOG (C. A. Sneden, 1973; C. Sneden, Bean, et al., 2012) in the machine-readable format.
(This table is available in its entirety in machine-readable form.)

tra. The observed Arcturus and solar spectra are both from Hinkle et al. (2000)[3]. The synthetic spectra were calculated (using MOOG and ATLAS9 stellar atmosphere models) with the following stellar parameters: Sun ($T_{\rm eff}$ = 5777 K, $\log g$ = 4.44, [Fe/H] = 0, [α/Fe] = 0), and Arcturus ($T_{\rm eff}$ = 4286 K, $\log g$ = 1.66, [Fe/H] = −0.52, [α/Fe] = 0.26, Ramírez and Allende Prieto 2011). The oscillator strengths of some of the lines in the line list were adjusted to better match the synthetic spectra to the observations. After the calibration was finished, the standard deviation of the absolute difference of the observed and synthetic flux is less than 4%. We smoothed the spectra to match the resolution of the DEIMOS observations and found that the dispersion decreased to less than 1%. The accuracy of the line list other than in the immediate region of the barium lines is only important for correcting the local continuum. For this purpose, 1% agreement assures that the line list will not be the dominant source of error.

We adopted McWilliam's (1998) line list for the five strong barium lines. This list accounts for hyper-fine and isotope splitting. We adopted the solar system barium isotope ratios from Anders and Grevesse (1989). The impact of this assumption was tested by measuring the change in [Ba/Fe] when assuming pure *r*-process and *s*-process isotope ratios from C. Sneden, Cowan, and Gallino (2008) in eight stars from

[3] ftp.noao.edu/catalogs/arcturusatlas/visual/

Sculptor that spanned the stellar parameters probed. We found a maximum change in [Ba/Fe] of 0.04 dex and an average change of 0.02 dex and 0.008 dex for r-process and s-process ratios, respectively. Compared to the measurement uncertainties in our barium measurements (≈ 0.2 dex), isotope ratios are not a significant source of error.

2.5 Barium Measurement Technique

We interpolated the synthetic spectra from our grid to match the exact parameters published for a given star ($T_{\rm eff}$, $\log g$, [Fe/H], and [α/Fe]) and smoothed them to match the resolution of the observed spectrum ($\sigma = 0.73$ Å Gaussian kernel). The local continuum was corrected by fitting a line to each 20 Å segment centered on a barium line with 1 Å on either side of the barium line masked out. The optimal barium abundance was measured by matching the synthetic spectra for various values of [Ba/Fe] to the observed spectrum. The best match was determined using a Levenberg-Marquardt fitting algorithm (via scipy.optimize.curve_fit, Jones, Oliphant, Peterson, et al. 2001). All barium lines are fit simultaneously, which is a key reason why we are able to measure accurate barium abundances in spectra with relatively low spectral resolution and S/N. If a given line doesn't provide a very useful constraint, due to noise or other issues, the fit relies on the other clearer lines. Most stars are measured using five barium lines, but occasionally the 5853.7 Å barium line falls in the DEIMOS chip gap, resulting in four barium lines being used. Figure 2.1 demonstrates a [Ba/Fe] fit for a single star. The top left panel shows the reduced chi-squared as a function of [Ba/Fe]. The remaining five panels each display a wavelength segment centered on a barium absorption line. The [Ba/Fe] error quoted in this figure does not include the systematic error. See Section 2.7 for a discussion on how the systematic uncertainty in [Ba/Fe] is determined. The figure demonstrates that the barium measurement is well constrained and has a statistical error similar to high-resolution studies.

2.6 The Catalog

After we measured all the member stars in our sample, our catalog contains barium abundance measurements of 243 stars belonging to five dwarf galaxies, making this the largest self-consistent sample of dwarf galaxy barium abundances measured to date. Table 2.6 gives the multi-element abundance catalog for dwarf spheroidal galaxy (dSph) stars where [Ba/Fe] has been measured with uncertainties less than 0.28 dex. One advantage of this catalog of barium abundances is that this large

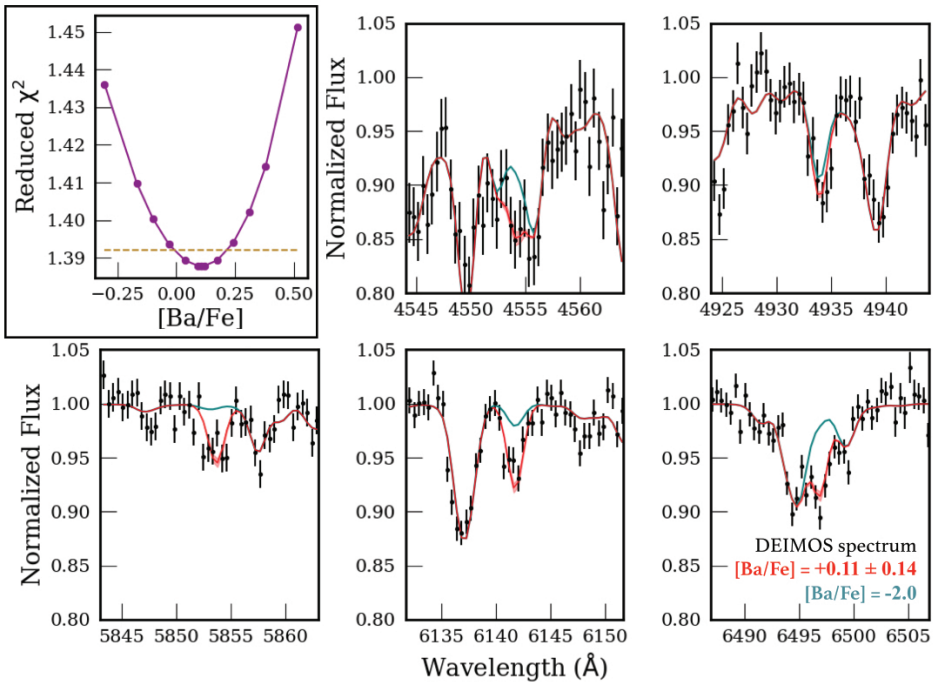

Figure 2.1: Example barium measurement for a single star in Draco. A DEIMOS medium-resolution spectrum (black) is shown alongside two synthetic spectra: the best-fit synthetic spectrum with the statistical error ranged shaded ([Ba/Fe] = +0.11 ± 0.14 dex, red) and one with [Ba/Fe] = −2.0 dex (blue). The top left panel shows the quality of the fit by comparing the reduced χ^2 for synthetic spectra at a range of [Ba/Fe] values (purple). The horizontal dotted brown line indicates the one sigma uncertainty of the measurement. While most individual absorption lines are not highly significant, the simultaneous fit of five barium lines enables uncertainties of ≈ 0.2 dex.

sample of stars is measured using the same assumptions in an automated way. This means that the catalog is internally consistent. The next section shows the consistency we achieve when comparing our [Ba/Fe] measurements to other measurements found in the literature, but it should be kept in mind that those literature measurements entail heterogeneous observations and measurement techniques.

2.7 Systematic Uncertainty

Beyond the [Ba/Fe] statistical errors returned by our fitting algorithm, we need to consider the systematic error of our measurement. The [Ba/Fe] statistical errors reflect the noise in the spectrum and how precisely the synthetic spectrum matches the observed spectrum. Technically, the statistical error reported is the square root of the diagonal values of the covariance matrix generated by Python's scipy.optimize.curve_fit (Jones, Oliphant, Peterson, et al., 2001) function when

Table 2.6: DEIMOS Multi-Element Abundances Catalog of dSph Stars

Name	R.A.	Decl.	$T_{\rm eff}$ (K)	$\log g$ (g in cm s^{-2})	ξ (km s^{-1})	[Fe/H] (dex)	[α/Fe] (dex)	[Ba/Fe] (dex)
615574	17h20m07.44s	+57d54m32.7s	4767 ± 46	1.44	1.80	−1.90 ± 0.10	−0.30 ± 0.18	+0.01 ± 0.24
622253	17h19m57.29s	+57d55m04.6s	4536 ± 23	1.14	1.87	−1.36 ± 0.10	−0.18 ± 0.09	+0.63 ± 0.13
649595	17h20m01.59s	+57d57m04.6s	4500 ± 34	0.87	1.94	−1.89 ± 0.10	−0.04 ± 0.10	+0.04 ± 0.16
648189	17h19m57.91s	+57d56m58.4s	4479 ± 27	0.81	1.95	−2.16 ± 0.10	+0.11 ± 0.09	−0.16 ± 0.16
588559	17h20m13.51s	+57d51m59.3s	4447 ± 23	0.77	1.96	−1.97 ± 0.10	+0.00 ± 0.09	−0.56 ± 0.15
660453	17h20m05.66s	+57d57m52.8s	4363 ± 24	0.73	1.97	−2.01 ± 0.10	+0.05 ± 0.09	+0.16 ± 0.15
598482	17h20m16.12s	+57d52m56.1s	4418 ± 49	0.77	1.96	−3.02 ± 0.10	+0.14 ± 0.18	−1.39 ± 0.24
676918	17h20m03.97s	+57d59m08.3s	4255 ± 16	0.40	2.05	−1.66 ± 0.10	−0.08 ± 0.09	+0.09 ± 0.13
640120	17h20m05.78s	+57d56m23.4s	4419 ± 27	0.50	2.02	−2.21 ± 0.10	+0.19 ± 0.09	−0.09 ± 0.13
653393	17h19m58.88s	+57d57m20.9s	4242 ± 20	0.12	2.11	−2.41 ± 0.10	+0.00 ± 0.09	−1.30 ± 0.14

Note. The errors reported here already include the systematic errors for [Fe/H], [α/Fe], and [Ba/Fe] found in Table 2.11. Stars are only included if the errors for [Fe/H], [α/Fe], and [Ba/Fe] are less than 0.28 dex.
(This table is available in its entirety in machine-readable form.)

fitting synthetic spectra to the observed spectrum. The [Ba/Fe] systematic error could be caused by the assumptions used in the spectral synthesis code (e.g., non-LTE effects), details of the method used to measure abundances, the line list, and how errors in other stellar parameters impact the [Ba/Fe] measured. The contribution of these sources helps us to establish an error floor that is added in quadrature with the statistical errors to produce the errors reported in the catalog.

Appropriateness of the LTE Assumption

We use a spectral synthesis code that assumes local thermal equilibrium (LTE), because it greatly simplifies the computational burden. In the LTE case the opacity needs be known as a function of only temperature and density to solve for the flux. However, the impact of assuming LTE is perhaps the most significant assumption of all the assumptions made in the spectral synthesis code. Assuming LTE is valid only when the radiation field is closely coupled to the matter, which occurs through collisions between atoms and electrons. Therefore LTE holds at high densities.

Several studies have carefully measured barium without assuming LTE (i.e., non-LTE) and compared them to LTE abundances published in the literature. For example, Andrievsky, Spite, et al. (2009) and Andrievsky, Korotin, et al. (2017) found that the difference between [Ba/Fe] measured with and without assuming LTE varies from negligible to very significant ($\lesssim 0.8$ dex). The impact of assuming LTE on barium abundance measurements is primarily dependent on the $T_{\rm eff}$ and [Ba/H] of the star in question (Andrievsky, Spite, et al., 2009). In addition, the details of the measurement (e.g., how many and which absorption lines are used) also plays a role on how sensitive the abundance measurements are to LTE effects.

To test the impact of assuming LTE with our observations, we measured a small, representative subset of stars with and without assuming LTE. We selected twelve stars that spanned the range of $T_{\rm eff}$ and [Ba/H] seen in our full sample. Both [Ba/Fe] measurements used the same DEIMOS spectra and stellar parameters. Andrievsky, Korotin, et al. (2017) describes the detailed methods of the non-LTE barium measurements. Our [Ba/Fe] measurements assuming LTE are consistent with the non-LTE measurements, as seen in Figure 2.2. The results are also reported in Table 2.7. Given that the impact of assuming LTE on [Ba/Fe] is well within the statistical uncertainties, no additional systematic uncertainty is needed to account for the effect of assuming LTE.

Table 2.7: Non-LTE Effects

dSph	Name	$T_{\rm eff}$ (K)	$\log g$ (g in cm s^{-2})	ξ (km s^{-1})	[Fe/H] (dex)	[α/Fe] (dex)	[Ba/Fe]$_{\rm LTE}$ (dex)	[Ba/Fe]$_{\rm non\text{-}LTE}$ (dex)
For	74926	3747 ± 11	0.21	2.09	−1.03 ± 0.10	−0.20 ± 0.10	+0.39 ± 0.19	+0.34
For	64059	3794 ± 12	0.32	2.07	−1.05 ± 0.10	−0.21 ± 0.10	+0.01 ± 0.19	+0.16
For	58973	3856 ± 11	0.36	2.06	−1.14 ± 0.10	−0.09 ± 0.10	+0.13 ± 0.17	+0.10
For	55262	4016 ± 19	0.45	2.04	−0.91 ± 0.10	+0.32 ± 0.13	+0.43 ± 0.17	+0.32
Scl	1018551	4182 ± 20	0.53	2.02	−1.72 ± 0.10	+0.14 ± 0.09	−0.05 ± 0.14	−0.05
Scl	1008522	4230 ± 14	0.55	2.01	−2.01 ± 0.10	+0.11 ± 0.09	+0.05 ± 0.13	+0.05
653393	4242 ± 20	0.12	2.11	−2.41 ± 0.10	+0.00 ± 0.09	−1.30 ± 0.14	−1.20	
Scl	1003537	4280 ± 18	0.58	2.01	−2.26 ± 0.10	+0.21 ± 0.09	−0.32 ± 0.13	−0.33
Scl	1013218	4622 ± 44	1.49	1.79	−1.55 ± 0.10	−0.06 ± 0.11	+1.51 ± 0.11	+1.35
Scl	1016539	4614 ± 51	1.40	1.81	−1.76 ± 0.11	+0.17 ± 0.13	+0.18 ± 0.19	+0.19
Scl	1010313	4770 ± 52	1.61	1.76	−2.78 ± 0.13	+0.47 ± 0.17	−0.43 ± 0.21	−0.35
UMi	Pal119	5075 ± 48	2.00	1.67	−1.83 ± 0.11	−0.36 ± 0.23	+0.75 ± 0.21	+0.74

(This table is available in machine-readable form.)

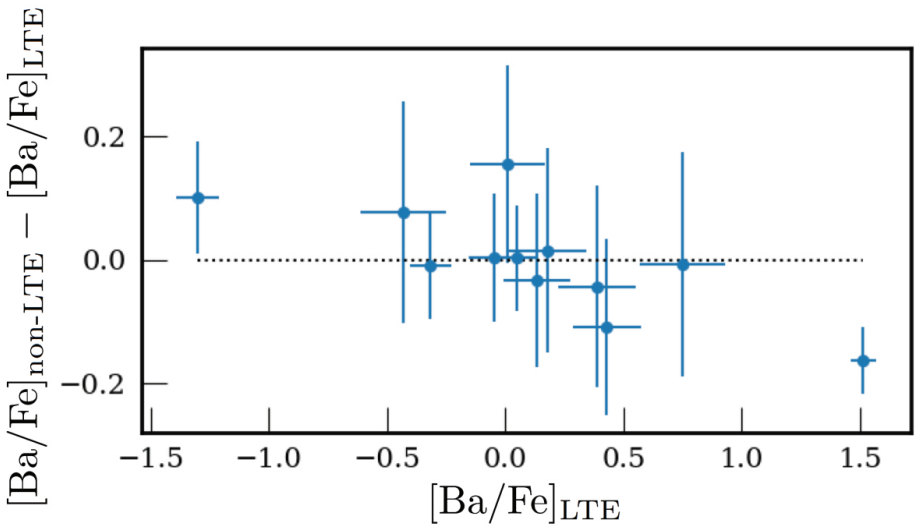

Figure 2.2: Comparison between our [Ba/Fe] measurements assuming LTE and without this assumption (i.e., non-LTE) using the same spectra and stellar parameters. These twelve representative stars show that the effect of assuming LTE is mostly within our statistical uncertainties.

Comparison to Other Catalogs

We must account for the systematic error introduced by any inaccuracies in the synthetic spectra and in the determination of stellar parameters. One way to account for this is to compare [Ba/Fe] measured for stars that overlap between our catalog and other catalogs published in the literature. All abundances have been shifted to the same solar abundance scale, which is described in Table 2.3. Table 2.8 highlights the different methods used by each literature source. Some of the differences between the measurements reflect the diversity of measurement techniques. In the following we refer to the literature sources as HRS because they all utilize high-resolution spectra. An advantage of our MRS sample is the uniformity of the acquisition and analysis of the spectra.

We compare a total of 74 stars that span [Ba/Fe] values from −1.2 to 0.8 dex. The stellar parameters and [Ba/Fe] measurements for both MRS and HRS methods are contained in Table 2.9. Figure 2.3 compares our barium abundances ($[Ba/Fe]_{MRS}$) to the barium abundances published in the literature ($[Ba/Fe]_{HRS}$). The barium abundances from MRS and HRS are largely consistent across the more than 1 dex span of [Ba/Fe] probed, but the difference ($[Ba/Fe]_{MRS} - [Ba/Fe]_{HRS}$) has a negligible offset between the MRS and HRS [Ba/Fe] measurements (0.001 dex). However, the difference ($[Ba/Fe]_{MRS} - [Ba/Fe]_{HRS}$) has a significant scatter.

Table 2.8: Previously Published HRS Abundance Methods

Reference	System	Atm.[a]	Code[b]	$T_{\rm eff}$[c]	log g[d]	ξ[e]
			Halo Field Stars			
Fulbright (2000)		ATLAS9	MOOG	spec	spec	spec
			Globular Clusters			
Lee et al. (2005)	M68	ATLAS9	MOOG	spec	spec[g]	spec
Cohen & Kirby (2012)	NGC 2419	ATLAS9	MOOG	phot	phot	spec
Venn et al. (2012)	M68	MARCS	MOOG	spec	phot	spec
Worley et al. (2013)	M15	ATLAS9	MOOG	phot	phot	spec[f]
			dSph			
Shetrone et al. (2001, 2003)	many	MARCS	MOOG	spec	spec	spec
Sadakane et al. (2004)	Ursa Minor	ATLAS9	SPTOOL	spec	spec	spec
Aoki et al. (2007)	Ursa Minor	ATLAS9	Tsuji	spec	spec	spec
Cohen & Huang (2009, 2010)	Draco, Ursa Minor	ATLAS9	MOOG	spec	spec	spec
Tsujimoto et al. (2017)	Draco	ATLAS9	Tsuji	phot	phot	spec
Letarte et al. (2018)	Fornax	MARCS	CALRAI	phot	phot	spec
Hill et al. (2019)	Sculptor	OS-MARCS	CALRAI	spec	spec	spec

[a] ATLAS9: R. Kurucz (1993), Castelli and R. L. Kurucz (2004), `http://kurucz.harvard.edu/grids.html`; MARCS: Gustafsson, Bell, et al. (1975), Gustafsson, Edvardsson, Eriksson, Mizuno-Wiedner, et al. (2003), and Gustafsson, Edvardsson, Eriksson, Jørgensen, et al. (2008); OSMARCS: Plez, Brett, and Nordlund (1992), Edvardsson et al. (1993), and Asplund et al. (1997).
[b] MOOG: C. A. Sneden (1973); CALRAI: Spite (1967); SPTOOL: Takeda (1995); Tsuji: Tsuji (1978), Wako Aoki et al. (2009).
[c] phot: model isochrones or empirical color-$T_{\rm eff}$ relation; spec: Fe I excitation equilibrium.
[d] phot: model isochrones or $T_{\rm eff}$, with assuming a stellar mass and determining the luminosity from bolometric corrections; spec: Fe I and Fe II ionization balance.
[e] spec: removing abundance trends as a function of equivalent width.
[f] A log g–ξ relation derived from a subset of stars was applied to the full sample.
[g] Photometric values were also published, but we have adopted the abundances measured with the spectroscopic values.

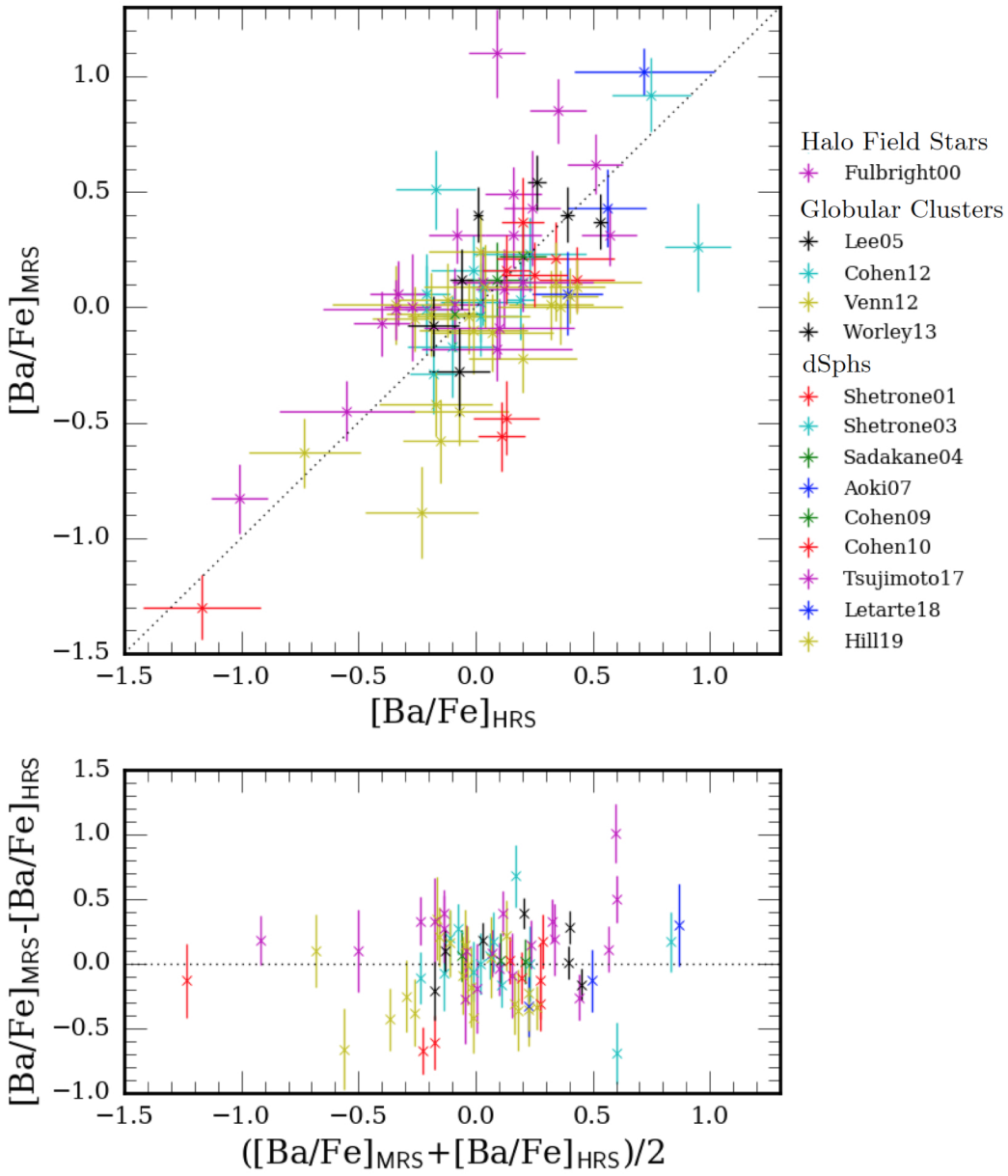

Figure 2.3: Comparison of our medium-resolution spectroscopy (MRS) to high-resolution spectroscopy (HRS) abundance measurements for 74 stars. See the legend of this figure or Table 2.9 for the sources of the HRS measurements.

Table 2.9: Comparison Between High-Resolution and DEIMOS Abundances

System	Name	HRS Reference	$[Fe/H]_{MRS}$ (dex)	$[Ba/Fe]_{MRS}$ (dex)	$[Fe/H]_{HRS}$ (dex)	$[Ba/Fe]_{HRS}$ (dex)
NGC 2419	N2419-S1004	Cohen and Kirby (2012)	-2.15 ± 0.09	-0.17 ± 0.22	-2.15 ± 0.14	-0.10 ± 0.19
NGC 2419	N2419-S1065	Cohen and Kirby (2012)	-2.11 ± 0.09	-0.01 ± 0.19	-2.10 ± 0.15	-0.21 ± 0.09
NGC 2419	N2419-S1131	Cohen and Kirby (2012)	-2.12 ± 0.08	$+0.09 \pm 0.17$	-2.10 ± 0.15	$+0.03 \pm 0.05$
NGC 2419	N2419-S1166	Cohen and Kirby (2012)	-2.04 ± 0.08	-0.29 ± 0.17	-2.07 ± 0.13	-0.18 ± 0.10
NGC 2419	N2419-S1209	Cohen and Kirby (2012)	-2.29 ± 0.08	-0.04 ± 0.17	-2.32 ± 0.11	$+0.02 \pm 0.16$
NGC 2419	N2419-S1305	Cohen and Kirby (2012)	-2.21 ± 0.09	$+0.03 \pm 0.17$	-2.25 ± 0.18	$+0.19 \pm 0.06$
NGC 2419	N2419-S1814	Cohen and Kirby (2012)	-2.20 ± 0.08	$+0.16 \pm 0.15$	-2.26 ± 0.14	-0.01 ± 0.18
NGC 2419	N2419-S223	Cohen and Kirby (2012)	-2.23 ± 0.08	$+0.23 \pm 0.16$	-2.19 ± 0.15	$+0.23 \pm 0.24$
NGC 2419	N2419-S406	Cohen and Kirby (2012)	-2.10 ± 0.09	$+0.06 \pm 0.17$	-2.10 ± 0.13	-0.21 ± 0.10
NGC 2419	N2419-S458	Cohen and Kirby (2012)	-2.10 ± 0.09	$+0.51 \pm 0.17$	-2.15 ± 0.15	-0.17 ± 0.17

Note. Some columns (e.g., $T_{\rm eff}$, $\log g$, ξ and [α/Fe] for both MRS and HRS) are suppressed in the printed edition, and only the first ten lines are shown. Although the Milky Way halo field stars (Fulbright, 2000) were measured with the same stellar parameters (e.g., $T_{\rm eff}$, $\log g$, [Fe/H], [α/Fe]) in both methods, stars in the dwarf galaxies and globular clusters have different stellar parameters in each method. Stars are only included if the errors for [Fe/H], [α/Fe], and [Ba/Fe] are less than 0.28 dex. (This table is available in machine-readable form.)

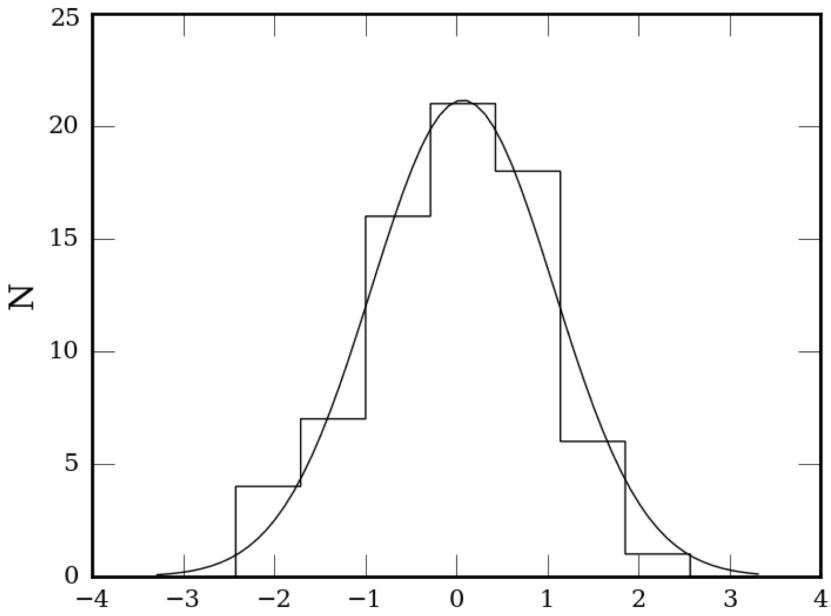

Figure 2.4: Distribution of differences between our medium-resolution spectroscopy (MRS) and high-resolution spectroscopy (HRS) measurements of [Ba/Fe] divided by the estimated error of the difference. The histogram contains 74 stars with a measured $\sigma_{\mathrm{sys}} = 0.21$. The curve is a Gaussian with $\sigma = 1$.

The standard deviation of the offset between the MRS and HRS [Ba/Fe] measurements provides a metric to determine the systematic uncertainty. Assuming the uncertainties published in the HRS [Ba/Fe] measurements are prefect representations of the true error, we solved for the systematic uncertainty required to standardize the offset. This is done by solving Equation 2.2 for the systematic error (σ_{sys}).

$$\mathrm{stddev}\left(\frac{[\mathrm{Ba/Fe}]_{\mathrm{MRS}} - [\mathrm{Ba/Fe}]_{\mathrm{HRS}}}{\sqrt{\sigma^2_{\mathrm{HRS}} + \sigma^2_{\mathrm{MRS}} + \sigma^2_{\mathrm{sys}}}}\right) = 1 \tag{2.2}$$

Thus, σ_{sys} is the error required to be added in quadrature with the MRS statistical error to force the dispersion between MRS and HRS to be unity. By comparing the MRS and HRS measurements of 74 stars, we measure $\sigma_{\mathrm{sys}} = 0.21$ dex. The resulting error distribution is shown in Figure 2.4.

Intrinsic Dispersion

With some exceptions (e.g., M15; C. Sneden, Kraft, M. D. Shetrone, et al., 1997), most globular clusters are expected to have no internal variation in heavy elements.

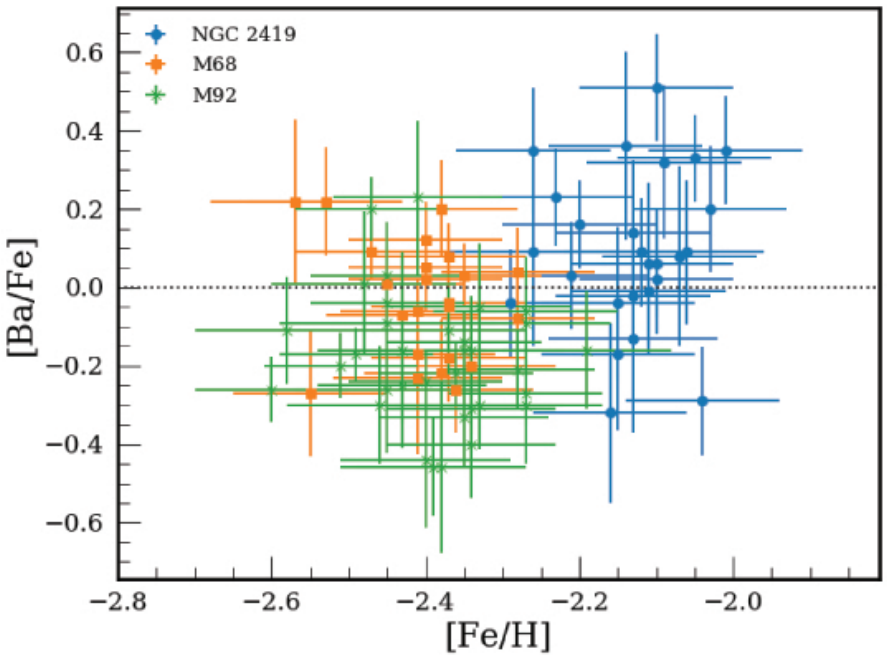

Figure 2.5: We have measured [Ba/Fe] for 26, 23, and 34 stars in NGC 2419, M68, and M92, respectively. This sample is used to constrain the systematic uncertainty of our measurement.

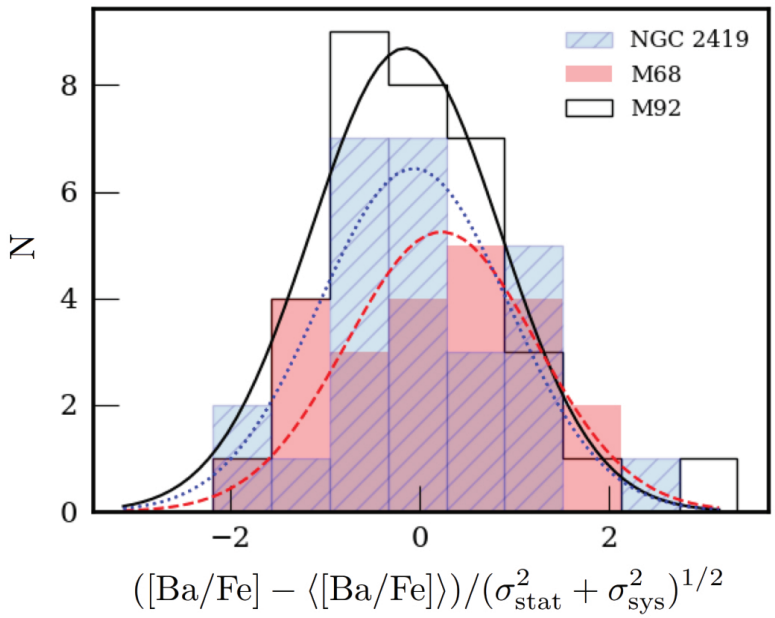

Figure 2.6: Distribution of differences from the average [Ba/Fe] measured in each globular cluster divided by the estimated error of the difference. By setting the intrinsic dispersion of NGC 2419, M68, and M92 to zero, we measured $\sigma_{\mathrm{sys}} = 0.11$, 0.07, and 0.09, respectively. The curves are Gaussians with $\sigma = 1$.

Here we measure the systematic error that would be required to ensure there is no intrinsic dispersion of [Ba/Fe] in a globular cluster. This measurement was done with NGC 2419, M68, and M92 using Equation 2.3, where ⟨[Ba/Fe]⟩ is the average abundance. This assumes that these globular clusters do not have intrinsic dispersion in [Ba/Fe], which may or may not be the case (e.g., Roederer and C. Sneden, 2011; Cohen, 2011), so the systematic uncertainty returned is an upper limit. By standardizing the offset (see Equation 2.3) of the ≈ 30 stars for which we were able to measure [Ba/Fe] in each globular cluster, we measure a $\sigma_{\rm sys}$ = 0.11, 0.07, and 0.09 dex for NGC 2419, M68, and M92, respectively. The abundances can be seen in Figure 2.5, and they are included in Table 2.10. The error distribution when including the measured systematic errors are shown in Figure 2.6.

$$\text{stddev}\left(\frac{\text{[Ba/Fe]} - \langle\text{[Ba/Fe]}\rangle}{\sqrt{\sigma_{\rm stat}^2 + \sigma_{\rm sys}^2}}\right) = 1 \tag{2.3}$$

Barium Abundance Error Floor

By comparing our [Ba/Fe] measurements to HRS measurements in the literature, we measure σ_{sys} = 0.21. By forcing the [Ba/Fe] measurements of ≈ 30 stars in NGC 2419, M68, and M92 to have no intrinsic dispersion, we measure σ_{sys} = 0.11, 0.07, and 0.09, respectively. There is a clear discrepancy between the systematic error measured from the HRS comparison and the globular clusters. The HRS comparison relies on a heterogeneous collection of literature sources, with different spectrographs, line lists, and analysis codes. Some or most of the systematic error determined from HRS comes from this heterogeneity. On the other hand, the globular cluster analysis is internal to our own homogeneous study. Therefore, we set our systematic error at 0.1 dex for [Ba/Fe]. For context, the statistical errors of our measurements range from 0.1 to 0.28 dex with an average of 0.19 dex. All of the abundance error floors used in our catalog can be seen in Table 2.11.

Table 2.10: DEIMOS Multi-Element Abundances Catalog of Globular Cluster Stars

Name	R.A.	Decl.	$T_{\rm eff}$ (K)	$\log g$ (g in cm s^{-2})	ξ (km s^{-1})	[Fe/H] (dex)	[α/Fe] (dex)	[Ba/Fe] (dex)
Stet-M92-S1081	$17^{\rm h}16^{\rm m}59^{\rm s}$	+43°7′10″	4971 ± 23	2.06	1.66	−2.45 ± 0.10	+0.31 ± 0.09	+0.03 ± 0.17
Stet-M92-S1377	$17^{\rm h}17^{\rm m}02^{\rm s}$	+43°6′56″	5429 ± 34	3.25	1.37	−2.35 ± 0.11	+0.23 ± 0.12	−0.33 ± 0.16
Stet-M92-S1416	$17^{\rm h}17^{\rm m}03^{\rm s}$	+43°6′37″	4983 ± 20	2.06	1.65	−2.37 ± 0.10	+0.25 ± 0.09	−0.11 ± 0.15
Stet-M92-S1622	$17^{\rm h}17^{\rm m}02^{\rm s}$	+43°9′32″	4781 ± 30	1.69	1.74	−2.35 ± 0.10	+0.24 ± 0.09	−0.16 ± 0.14
Stet-M92-S1687	$17^{\rm h}17^{\rm m}05^{\rm s}$	+43°7′32″	5431 ± 25	2.92	1.45	−2.27 ± 0.10	+0.33 ± 0.10	−0.30 ± 0.18
Stet-M92-S2476	$17^{\rm h}17^{\rm m}08^{\rm s}$	+43°11′27″	5162 ± 26	2.48	1.56	−2.49 ± 0.10	+0.36 ± 0.09	−0.17 ± 0.12
Stet-M92-S2492	$17^{\rm h}17^{\rm m}12^{\rm s}$	+43°7′29″	5721 ± 29	3.52	1.31	−2.19 ± 0.11	+0.22 ± 0.12	−0.16 ± 0.18
Stet-M92-S2732	$17^{\rm h}17^{\rm m}11^{\rm s}$	+43°10′35″	5428 ± 27	3.33	1.35	−2.33 ± 0.11	+0.04 ± 0.13	−0.30 ± 0.15
Stet-M92-S2736	$17^{\rm h}17^{\rm m}11^{\rm s}$	+43°10′29″	5053 ± 23	2.15	1.63	−2.47 ± 0.10	+0.31 ± 0.09	+0.20 ± 0.13
Stet-M92-S2977	$17^{\rm h}17^{\rm m}13^{\rm s}$	+43°11′19″	5495 ± 29	3.36	1.35	−2.27 ± 0.11	+0.27 ± 0.12	−0.09 ± 0.17

Note. The errors reported here already include the systematic errors for [Fe/H], [α/Fe], and [Ba/Fe] found in Table 2.11. Stars are only included if the errors for [Fe/H], [α/Fe], and [Ba/Fe] are less than 0.28 dex.
(This table is available in machine-readable form.)

Table 2.11: Abundance Error Floor

Abundance	Error Floor
[Fe/H]	0.101
[α/Fe]	0.084
[Ba/Fe]	0.100

Note. These systematic errors are included in the errors given in Table 2.6.

References

Anders, E. and N. Grevesse (1989). "Abundances of the elements - Meteoritic and solar". In: *GeoCoA* 53, pp. 197–214. DOI: 10.1016/0016-7037(89)90286-X.

Andrievsky, S. M., S. A. Korotin, et al. (2017). "Barium abundance in the central part of the dSph Fornax galaxy". In: *arXiv e-prints*, arXiv:1710.04930, arXiv:1710.04930. arXiv: 1710.04930 [astro-ph.GA].

Andrievsky, S. M., M. Spite, et al. (2009). "Evolution of the barium abundance in the early Galaxy from a NLTE analysis of the Ba lines in a homogeneous sample of EMP stars". In: *A&A* 494, pp. 1083–1090. DOI: 10.1051/0004-6361:200810894. arXiv: 0902.0450 [astro-ph.GA].

Aoki, Wako et al. (2009). "Lithium Abundances of Extremely Metal-Poor Turnoff Stars". In: *ApJ* 698, pp. 1803–1812. DOI: 10.1088/0004-637X/698/2/1803. arXiv: 0904.1448 [astro-ph.SR].

Aoki, W. et al. (2007). "First Determination of the Actinide Thorium Abundance for a Red Giant of the Ursa Minor Dwarf Galaxy". In: *PASJ* 59, pp. L15–L19. DOI: 10.1093/pasj/59.3.L15. arXiv: 0704.3104.

Asplund, M. et al. (1997). "Line-blanketed model atmospheres for R Coronae Borealis stars and hydrogen-deficient carbon stars." In: *A&A* 318, pp. 521–534.

Bellazzini, M. et al. (2002). "The Draco and Ursa Minor Dwarf Spheroidal Galaxies: A Comparative Study". In: *AJ* 124, pp. 3222–3240. DOI: 10.1086/344794. eprint: astro-ph/0209391.

Castelli, F. and R. L. Kurucz (2004). "New Grids of ATLAS9 Model Atmospheres". In: *ArXiv Astrophysics e-prints*. eprint: astro-ph/0405087.

Cohen, J. G. (2011). "No Heavy-element Dispersion in the Globular Cluster M92". In: *ApJL* 740, L38, p. L38. DOI: 10.1088/2041-8205/740/2/L38. arXiv: 1109.2876 [astro-ph.SR].

Cohen, J. G. and W. Huang (2009). "The Chemical Evolution of the Draco Dwarf Spheroidal Galaxy". In: *ApJ* 701, pp. 1053–1075. DOI: 10.1088/0004-637X/701/2/1053. arXiv: 0906.1006 [astro-ph.GA].

– (2010). "The Chemical Evolution of the Ursa Minor Dwarf Spheroidal Galaxy". In: *ApJ* 719, pp. 931–949. DOI: 10.1088/0004-637X/719/1/931. arXiv: 1006.3538.

Cohen, J. G. and E. N. Kirby (2012). "The Bizarre Chemical Inventory of NGC 2419, An Extreme Outer Halo Globular Cluster". In: *ApJ* 760, 86, p. 86. DOI: 10.1088/0004-637X/760/1/86. arXiv: 1209.2705 [astro-ph.GA].

Cooper, M. C. et al. (2012). *spec2d: DEEP2 DEIMOS Spectral Pipeline*. Astrophysics Source Code Library. ascl: 1203.003.

Edvardsson, B. et al. (1993). "The chemical evolution of the galactic disk. I. Analysis and results." In: *A&A* 500, pp. 391–442.

Fulbright, J. P. (2000). "Abundances and Kinematics of Field Halo and Disk Stars. I. Observational Data and Abundance Analysis". In: *AJ* 120, pp. 1841–1852. DOI: 10.1086/301548. eprint: astro-ph/0006260.

– (2002). "Abundances and Kinematics of Field Stars. II. Kinematics and Abundance Relationships". In: *AJ* 123, pp. 404–412. DOI: 10.1086/324630. eprint: astro-ph/0110164.

Gustafsson, B., R. A. Bell, et al. (1975). "A grid of model atmospheres for metal-deficient giant stars. I". In: *A&A* 42, pp. 407–432.

Gustafsson, B., B. Edvardsson, K. Eriksson, U. G. Jørgensen, et al. (2008). "A grid of MARCS model atmospheres for late-type stars. I. Methods and general properties". In: *A&A* 486, pp. 951–970. DOI: 10.1051/0004-6361:200809724. arXiv: 0805.0554.

Gustafsson, B., B. Edvardsson, K. Eriksson, M. Mizuno-Wiedner, et al. (2003). "A Grid of Model Atmospheres for Cool Stars". In: *Stellar Atmosphere Modeling*. Ed. by I. Hubeny, D. Mihalas, and K. Werner. Vol. 288. Astronomical Society of the Pacific Conference Series, p. 331.

Harris, W. E. (1996). "A Catalog of Parameters for Globular Clusters in the Milky Way". In: *AJ* 112, p. 1487. DOI: 10.1086/118116.

Hill, V. et al. (2019). "VLT/FLAMES high-resolution chemical abundances in Sculptor: a textbook dwarf spheroidal galaxy". In: *A&A* 626, A15, A15. DOI: 10.1051/0004-6361/201833950. arXiv: 1812.01486 [astro-ph.GA].

Hinkle, K. et al. (2000). *Visible and Near Infrared Atlas of the Arcturus Spectrum 3727-9300 A*.

Jones, Eric, Travis Oliphant, Pearu Peterson, et al. (2001). *SciPy: Open source scientific tools for Python*. [Online; accessed 2017-01-16]. URL: http://www.scipy.org/.

Kirby, E. N., P. Guhathakurta, M. Bolte, et al. (2009). "Multi-element Abundance Measurements from Medium-resolution Spectra. I. The Sculptor Dwarf Spheroidal Galaxy". In: *ApJ* 705, pp. 328–346. DOI: 10.1088/0004-637X/705/1/328. arXiv: 0909.3092.

Kirby, E. N., P. Guhathakurta, J. D. Simon, et al. (2010). "Multi-element Abundance Measurements from Medium-resolution Spectra. II. Catalog of Stars in Milky Way Dwarf Satellite Galaxies". In: *ApJS* 191, pp. 352–375. DOI: 10.1088/0067-0049/191/2/352. arXiv: 1011.4516 [astro-ph.GA].

Kirby, E. N., P. Guhathakurta, A. J. Zhang, et al. (2016). "Lithium-rich Giants in Globular Clusters". In: *ApJ* 819, 135, p. 135. DOI: 10.3847/0004-637X/819/2/135. arXiv: 1601.01315 [astro-ph.SR].

Kirby, E. N., M. Guo, et al. (2015). "Carbon in Red Giants in Globular Clusters and Dwarf Spheroidal Galaxies". In: *ApJ* 801, 125, p. 125. DOI: 10.1088/0004-637X/801/2/125. arXiv: 1501.06908.

Kurucz, R. (1993). "ATLAS9 Stellar Atmosphere Programs and 2 km/s grid." In: *ATLAS9 Stellar Atmosphere Programs and 2 km/s grid. Kurucz CD-ROM No. 13. Cambridge, Mass.: Smithsonian Astrophysical Observatory, 1993.* 13.

Lee, J.-W., B. W. Carney, and M. J. Habgood (2005). "Chemical Abundances for Seven Giant Stars in M68 (NGC 4590): A Globular Cluster with Abnormal Silicon and Titanium Abundances". In: *AJ* 129, pp. 251–266. DOI: 10.1086/426338. eprint: astro-ph/0409706.

Lee, M. G. et al. (2003). "Deep Wide-Field BVI CCD Photometry of the Sextans Dwarf Spheroidal Galaxy". In: *AJ* 126, pp. 2840–2866. DOI: 10.1086/379171.

Lemasle, B. et al. (2014). "VLT/FLAMES spectroscopy of red giant branch stars in the Fornax dwarf spheroidal galaxy". In: *A&A* 572, A88, A88. DOI: 10.1051/0004-6361/201423919. arXiv: 1409.7703.

Letarte, B. et al. (2018). "A high-resolution VLT/FLAMES study of individual stars in the centre of the Fornax dwarf spheroidal galaxy (Corrigendum)". In: *A&A* 613, p. C1. DOI: 10.1051/0004-6361/200913413e. URL: https://doi.org/10.1051/0004-6361/200913413e.

Mateo, M. L. (1998). "Dwarf Galaxies of the Local Group". In: *ARA&A* 36, pp. 435–506. DOI: 10.1146/annurev.astro.36.1.435. eprint: astro-ph/9810070.

McWilliam, A. (1998). "Barium Abundances in Extremely Metal-poor Stars". In: *AJ* 115, pp. 1640–1647. DOI: 10.1086/300289.

Mighell, K. J. and C. J. Burke (1999). "WFPC2 Observations of the Ursa Minor Dwarf Spheroidal Galaxy". In: *AJ* 118, pp. 366–380. DOI: 10.1086/300923. eprint: astro-ph/9903065.

Newman, J. A. et al. (2013). "The DEEP2 Galaxy Redshift Survey: Design, Observations, Data Reduction, and Redshifts". In: *ApJS* 208, 5, p. 5. DOI: 10.1088/0067-0049/208/1/5. arXiv: 1203.3192.

Pietrzyński, G. et al. (2008). "The Araucaria Project: the Distance to the Sculptor Dwarf Spheroidal Galaxy from Infrared Photometry of RR Lyrae Stars". In: *AJ* 135, pp. 1993–1997. DOI: 10.1088/0004-6256/135/6/1993. arXiv: 0804.0347.

Plez, B., J. M. Brett, and A. Nordlund (1992). "Spherical opacity sampling model atmospheres for M-giants. I - Techniques, data and discussion". In: *A&A* 256, pp. 551–571.

Ramírez, I. and C. Allende Prieto (2011). "Fundamental Parameters and Chemical Composition of Arcturus". In: *ApJ* 743, 135, p. 135. DOI: 10.1088/0004-637X/743/2/135. arXiv: 1109.4425 [astro-ph.SR].

Rizzi, L. et al. (2007). "The distance to the Fornax dwarf spheroidal galaxy". In: *MNRAS* 380, pp. 1255–1260. DOI: 10.1111/j.1365-2966.2007.12196.x. arXiv: 0707.0521.

Roederer, I. U. and C. Sneden (2011). "Heavy-element Dispersion in the Metal-poor Globular Cluster M92". In: *AJ* 142, 22, p. 22. DOI: 10.1088/0004-6256/142/1/22. arXiv: 1104.5055 [astro-ph.SR].

Ryabchikova, T. et al. (2015). "A major upgrade of the VALD database". In: *PhyS* 90.5, 054005, p. 054005. DOI: 10.1088/0031-8949/90/5/054005.

Sadakane, K. et al. (2004). "Subaru/HDS Abundances in Three Giant Stars in the Ursa Minor Dwarf Spheroidal Galaxy". In: *PASJ* 56, pp. 1041–1058. DOI: 10.1093/pasj/56.6.1041. eprint: astro-ph/0411332.

Shetrone, M. D., P. Côté, and W. L. W. Sargent (2001). "Abundance Patterns in the Draco, Sextans, and Ursa Minor Dwarf Spheroidal Galaxies". In: *ApJ* 548, pp. 592–608. DOI: 10.1086/319022. eprint: astro-ph/0009505.

Shetrone, M. et al. (2003). "VLT/UVES Abundances in Four Nearby Dwarf Spheroidal Galaxies. I. Nucleosynthesis and Abundance Ratios". In: *AJ* 125, pp. 684–706. DOI: 10.1086/345966. eprint: astro-ph/0211167.

Sneden, C. A. (1973). "Carbon and Nitrogen Abundances in Metal-Poor Stars." PhD thesis. THE UNIVERSITY OF TEXAS AT AUSTIN.

Sneden, C., J. Bean, et al. (2012). *MOOG: LTE line analysis and spectrum synthesis*. Astrophysics Source Code Library. ascl: 1202.009.

Sneden, C., J. J. Cowan, and R. Gallino (2008). "Neutron-Capture Elements in the Early Galaxy". In: *ARA&A* 46, pp. 241–288. DOI: 10.1146/annurev.astro.46.060407.145207.

Sneden, C., R. P. Kraft, C. F. Prosser, et al. (1992). "Oxygen abundances in halo giants. III - Giants in the mildly metal-poor globular cluster M5". In: *AJ* 104, pp. 2121–2140. DOI: 10.1086/116388.

Sneden, C., R. P. Kraft, M. D. Shetrone, et al. (1997). "Star-To-Star Abundance Variations Among Bright Giants in the Metal-Poor Globular Cluster M15". In: *AJ* 114, p. 1964. DOI: 10.1086/118618.

Sneden, C., S. Lucatello, et al. (2014). "Line Lists for the A $^2\Pi$-X $^2\Sigma^+$ (Red) and B $^2\Sigma^+$-X $^2\Sigma^+$ (Violet) Systems of CN, $^{13}C^{14}N$, and $^{12}C^{15}N$, and Application to Astronomical Spectra". In: *ApJS* 214, 26, p. 26. DOI: 10.1088/0067-0049/214/2/26. arXiv: 1408.3828 [astro-ph.SR].

Spite, M. (1967). "Étude de l'étoile χ Draconis". In: *Annales d'Astrophysique* 30, p. 211.

Starkenburg, E. et al. (2013). "The extremely low-metallicity tail of the Sculptor dwarf spheroidal galaxy". In: *A&A* 549, A88, A88. DOI: 10.1051/0004-6361/201220349. arXiv: 1211.4592.

Takeda, Y. (1995). "Self-consistent multi-parameter fitting of stellar flux spectra". In: *PASJ* 47, pp. 287–298.

Tolstoy, E. et al. (2006). "The Dwarf galaxy Abundances and Radial-velocities Team (DART) Large Programme - A Close Look at Nearby Galaxies". In: *The Messenger* 123.

Tsuji, T. (1978). "Spectral energy distributions and effective temperature scale of M-giant stars." In: *A&A* 62, pp. 29–50.

Tsujimoto, T. et al. (2017). "Enrichment in r-process Elements from Multiple Distinct Events in the Early Draco Dwarf Spheroidal Galaxy". In: *ApJL* 850, L12, p. L12. DOI: 10.3847/2041-8213/aa9886. arXiv: 1711.02121 [astro-ph.SR].

Venn, K. A. et al. (2012). "Nucleosynthesis and the Inhomogeneous Chemical Evolution of the Carina Dwarf Galaxy". In: *ApJ* 751, 102, p. 102. DOI: 10.1088/0004-637X/751/2/102. arXiv: 1204.0787.

Weisz, D. R. et al. (2014). "The Star Formation Histories of Local Group Dwarf Galaxies. II. Searching For Signatures of Reionization". In: *ApJ* 789, 148, p. 148. DOI: 10.1088/0004-637X/789/2/148. arXiv: 1405.3281.

Worley, C. C. et al. (2013). "Ba and Eu abundances in M 15 giant stars". In: *A&A* 553, A47, A47. DOI: 10.1051/0004-6361/201321097. arXiv: 1302.6122 [astro-ph.SR].

Chapter 3

NEUTRON STAR MERGERS ARE THE DOMINANT SOURCE OF THE R-PROCESS IN THE EARLY EVOLUTION OF DWARF GALAXIES

Duggan, G. E. et al. (2018). "Neutron Star Mergers are the Dominant Source of the r-process in the Early Evolution of Dwarf Galaxies". In: *Astrophysical Journal* 869, 50, p. 50. DOI: 10.3847/1538-4357/aaeb8e. arXiv: 1809.04597.

The following figures have been updated from their published forms to include a recent published catalog (Hill et al., 2019): Figures 3.2 and 3.3.

ABSTRACT

There are many candidate sites of the r-process: core-collapse supernovae (including rare magnetorotational core-collapse supernovae), neutron star mergers, and neutron star/black hole mergers. The chemical enrichment of galaxies—specifically dwarf galaxies—helps distinguish between these sources based on the continual build-up of r-process elements. This technique can distinguish between the r-process candidate sites by the clearest observational difference: how quickly these events occur after the stars are created. The existence of several nearby dwarf galaxies allows us to measure robust chemical abundances for galaxies with different star formation histories. Dwarf galaxies are especially useful because simple chemical evolution models can be used to determine the sources of r-process material. We have measured the r-process element barium with Keck/DEIMOS medium-resolution spectroscopy. We present the largest sample of barium abundances (almost 250 stars) in dwarf galaxies ever assembled. We measure [Ba/Fe] as a function of [Fe/H] in this sample and compare with existing [α/Fe] measurements. We have found that a large contribution of barium needs to occur at more delayed timescales than core-collapse supernovae in order to explain our observed abundances, namely the significantly more positive trend of the r-process component of [Ba/Fe] vs. [Fe/H] seen for [Fe/H] $\lesssim -1.6$ when compared to the [Mg/Fe] vs. [Fe/H] trend. We conclude that neutron star mergers are the most likely source of r-process enrichment in dwarf galaxies at early times.

3.1 Introduction

Galactic archaeology looks back in time by utilizing the fact that long-lived stars retain the memory of the chemical composition of the galaxy when they were born. We trace a variety of elements in stars alive today to learn about the timescales and origins of chemical enrichment in dwarf galaxies.

We will discuss three different groups of elements observable in stars. These elements were chosen because each group traces different stellar events. The first group is the α elements (e.g., Mg). These elements are created and ejected in core-collapse supernovae (CCSNe) with a short delay time ($4 - 25$ Myr). The delay time is defined as the time between the star being born and the star ejecting enriched material into the ISM. The second group is iron. Iron is produced in large amounts by SNe Ia with a relatively long delay time ($0.04 - 14$ Gyr, Maoz and Graur, 2017) described by a delay time distribution. In addition, there are moderate amounts of iron that are generated in each CCSNe. Finally, elements heavier than iron are formed through neutron-capture processes. Determining the dominant origin of neutron-capture elements is still an active area of study and is the focus of this chapter. Because the origin is unknown, the delay time is also unknown.

The ratio of α elements to iron ([α/Fe]) is commonly used as a chemical clock (Tinsley, 1980). If we know the exact amount of each element released during each process (also referred to as the yield), [α/Fe] can tell us the ratio of CCSNe to SNe Ia as a function of time. Starting from a star formation history (SFH), one can convert time into an iron abundance by assuming an initial mass function (IMF) and supernovae iron yields. As a stellar population ages, the rate of CCSNe changes compared to SNe Ia because of their different lifetimes. The [α/Fe] starts out high at low [Fe/H] (or early times) because CCSNe quickly eject a large amount of α elements with small amounts of iron (Nomoto et al., 2006). Then [α/Fe] dramatically declines as time passes and [Fe/H] increases, because SNe Ia start to explode and eject large amounts of iron (Iwamoto et al., 1999). The plot of [α/Fe] vs. [Fe/H] has been used in many studies of galactic evolution, typically by using [Mg/Fe] as an indicator of the total [α/Fe] (e.g., Gilmore and Wyse, 1991; M. D. Shetrone, P. Côté, and Sargent, 2001; Venn et al., 2004; Kirby, Cohen, et al., 2011; Bensby, Feltzing, and Oey, 2014).

Using neutron-capture elements as a chemical clock is less common, but may be the key to distinguish the dominant origin of neutron-capture elements. This chapter uses barium as a tracer of all neutron-capture elements, because barium is arguably

the easiest neutron-capture element to measure due to its several strong absorption lines available in the optical. The [Ba/Fe] indicates what levels of barium are being ejected into the ISM compared to SNe Ia throughout time. Combining the [Ba/Fe] vs. [Fe/H] 'chemical clock' with abundances of another neutron-capture element (e.g., europium), clarifies the origin of neutron-capture elements even further. The ratio of these two different neutron-capture elements ([Ba/Eu]) tells us the percentage of all neutron-capture elements produced by the two different neutron-capture processes: the *s*- and the *r*-process.

We know that for heavy neutron-capture elements—such as barium—the *s*-process is produced by AGB stars, with trace amounts possibly produced in massive stars (e.g., Karakas and Lattanzio, 2014). Unlike the *s*-process, there is little consensus on the astrophysical origin of the *r*-process, but the origin has been isolated to various explosions or mergers. See Section 1.1 for a thorough discussion of the *s*- and *r*-process.

3.2 Distinguishing Between Dominant R-Process Candidates Based on Timescales for the First Time

We have narrowed down our search for the dominant source of *r*-process enrichment in galaxies to a rare form of core-collapse supernovae (i.e., MRSNe) or NSMs in Section 1.2. The simulations of these two candidate sites are so poorly constrained that distinguishing between MRSNe and NSMs by comparing detailed abundance patterns is extremely challenging (e.g., Ji and Frebel, 2018). The clearest way to definitively distinguish between MRSNe and NSMs is by their different timescales.

The chemical enrichment of galaxies—specifically dwarf galaxies—enables us to distinguish between these sources based on their timescales. This is possible because we observe the continual build-up of *r*-process elements, and this type of study is an essential counterpart to the characterization of individual events. Specifically, we are sensitive to the enrichment timescale, which is the key distinguishing characteristic between MRSNe and NSMs. Robust chemical abundance trends can be measured for nearby dwarf galaxies, because their nearness and intact stellar populations allow us to average the abundances of many individually resolvable stars. Determining the sources of chemical enrichment from our observed abundance trends in dwarf galaxies is possible, because (1) their small masses make them very sensitive to feedback mechanisms, (2) the lack of major mergers helped preserve their stellar populations, and (3) their small sizes result in nearly instanta-

neous mixing compared to the chemical enrichment timescale (Escala et al., 2018). All of these properties make dwarf galaxies the perfect test sites to observe the simplest form of galactic chemical evolution. The existence of several nearby dwarf galaxies provides additional diagnostic power, because we can measure the chemical enrichment for galaxies with different star formation histories. The lessons learned in dwarf galaxies can then be applied to larger, more complex galaxies.

The usefulness of dwarf galaxies for determining the characteristics of *r*-process enrichment can be seen in Ji, Frebel, et al.'s 2016 study of the ultra-faint dwarf (UFD) galaxy Reticulum II. Several stars in Reticulum II have very high levels of enrichment in barium and europium. No other similarly enhanced stars were found in the other nine UFD galaxies considered. This indicates that a rare event occurred that dramatically increased the neutron-capture enrichment in Reticulum II. The [Ba/Eu] confirms that this enrichment was created by the *r*-process. Ji, Frebel, et al. (2016) calculated that this high enrichment could be caused by a single event in the small UFD galaxy. This rules out a typical CCSN, because CCSNe are so frequent that we would see this effect in many UFD galaxies . Both MRSNe and NSMs are predicted to be rare and produce a large amount of *r*-process enrichment. As we have mentioned before, the main observable difference between MRSNe and NSMs is their timescales. The short SFH of Reticulum II challenges whether it is possible to have a NSM occur while stars are still forming. However, because we are discussing a single rare event, it is possible an unusually quick NSM occurred in Reticulum II. Therefore we need to see enrichment occur in larger mass dwarf galaxies, so that many of these rare prolific *r*-process events have occurred and we have some statistical certainty if we need an event with a short (MRSNe) or long (NSMs) timescale.

In order to break this degeneracy between NSMs and MRSNe, we need a large sample of stars in many moderately-sized dwarf galaxies. We have measured barium with DEIMOS medium-resolution spectroscopy (Faber et al., 2003), and will present the largest sample of barium abundances (almost 250 stars) in dwarf galaxies ever assembled.

3.3 Sample of Barium Abundances in Dwarf Galaxies

We can observe neutron-capture abundance trends for several galaxies for the first time, because we have the largest sample of barium abundance measurements in dwarf galaxies ever assembled. We measured barium abundances in ≈250 stars

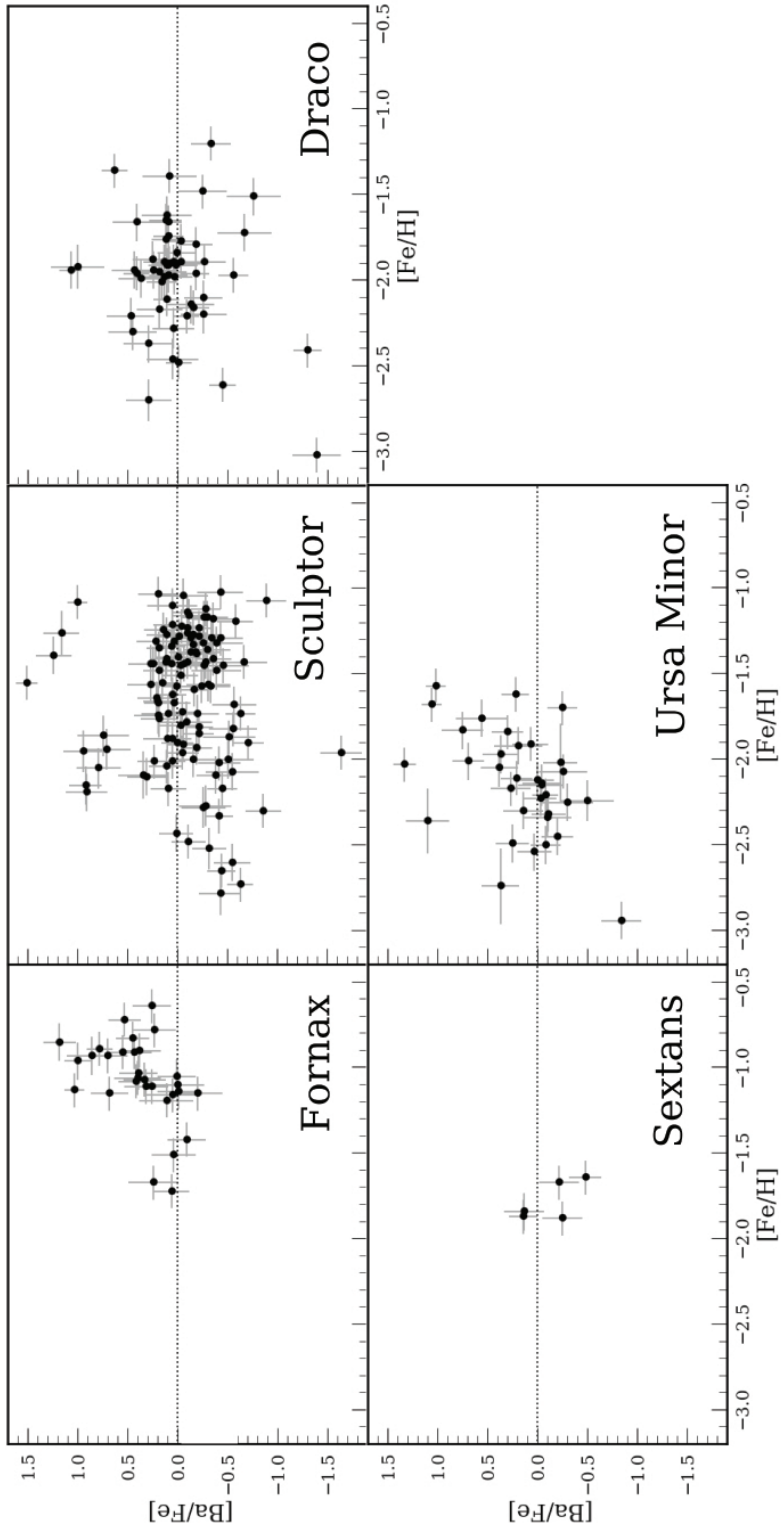

Figure 3.1: Barium abundance measurements in Fornax, Sculptor, Draco, Sextans, and Ursa Minor dwarf galaxies. This is the largest sample of barium measurements in dwarf galaxies ever assembled with a total of 243 stars. Our discussion focuses on the abundance trends seen for each galaxy. In this discussion, we neglect the high [Ba/Fe] outliers that are most clearly seen in Sculptor. These stars are likely to have been enriched by an AGB companion.

with more than 30 red giant branch stars in each of Draco, Sculptor, Fornax, and Ursa Minor, in addition to five stars in Sextans (Figure 3.1). This catalog of abundances increases the number of stars with barium measurements in these galaxies substantially, which can be seen by comparing the number of stars with published [Ba/Fe] currently found in the literature ($N_{\rm LIT}$) with the number of stars in our catalog (N) given in Table 3.1.

Before we discuss the abundance trends in these galaxies, it is important to discuss the very high [Ba/Fe] outliers that make up $\lesssim 10\%$ our sample. They are particularly obvious in Sculptor (10 stars with [Ba/Fe] > 0.5), but likely contaminate the other dwarf galaxies as well. We believe that many of these barium-rich outliers are stars that have been in a binary with an AGB star at some point in their evolution. That AGB companion transferred *s*-process rich material onto the surface of the secondary star. The primary star since evolved into a white dwarf, leaving us to measure the polluted secondary red giant. Some literature studies have found similarly barium-rich stars ([Ba/Fe] ≈ 0.5) and were able to use abundances of additional elements to confirm that they were enriched by an AGB companion (e.g., Honda et al., 2011). Additional elemental abundances would be required to prove that these outliers in our sample have been polluted by AGB stars, which is beyond the scope of this chapter. If these stars have been polluted, they do not represent the chemical composition of the gas from which they were born and should therefore be ignored when discussing abundance trends. However, we leave these stars in our sample because we do not have confirmation (from light elements or radial velocity variations) that these stars were enriched by an AGB companion. The outliers are relatively rare, so they do not significantly bias our results.

3.4 Why AGB Stars are Not the Dominant Source of Barium Enrichment at Early Times

In Section 1.2 we isolated the potential large contributors of barium to AGB stars for the *s*-process, and either a rare type of CCSNe (e.g., MRSNe) or NSMs for the *r*-process. We now consider the *s*-process source of barium, AGB stars, and discuss why they are not expected to be the dominant source of barium at early times.

In the solar system, barium is primarily produced by the *s*-process (85%, Simmerer et al., 2004), which mainly occurs in AGB stars. However, each AGB star produces a small amount of barium ($\lesssim 10^{-6}$ M$_\odot$ of barium from AGB stars with [Fe/H] ≈ -0.7; Karakas, Lugaro, et al. 2018). In old, metal-poor stellar populations there has

Table 3.1: Properties of Dwarf Galaxies

Galaxy	D[a] (kpc)	M_*[b] (10^5 $M_\odot$)	$\langle\tau_{SF}\rangle$[c] (Gyr)	τ_{90}[d] (Gyr)	[Ba/Eu]$_{med}$[e] (dex)	f_r[f] (%)	$\langle$[Fe/H]$\rangle$[g] (dex)	N[h]	$\langle$[Ba/Fe]$\rangle$[i] (dex)	N$_{LIT}$[j]
Fornax	147 ± 9	190 ± 50	7.4	2.3	−0.19	33%	−0.99 ± 0.01	30	0.50 ± 0.03	106
Sculptor	85 ± 4	12 ± 5	12.6	10.8	−0.27	40%	−1.68 ± 0.01	119	−0.02 ± 0.02	16
Draco	75 ± 5	9.1 ± 1.4	10.9	10.2	−0.43	58%	−1.93 ± 0.01	55	0.04 ± 0.02	24
Sextans	85 ± 3	8.5 ± 2.4	12.0	12.9	...	...	−1.93 ± 0.01	5	−0.12 ± 0.08	12
Ursa Minor	75 ± 3	5.6 ± 1.7	12.0	9.0	−0.57	80%	−2.13 ± 0.01	34	0.33 ± 0.03	20

[a] Distance from the MW (Kirby, Bullock, et al., 2014, and references therein).

[b] Stellar masses from Woo, Courteau, and Dekel (2008).

[c] Mean mass-weighted stellar age from Orban et al. (2008).

[d] Age at which 90% of the stellar mass formed from Weisz et al.'s (2014) cumulative star formation histories. Sextans is not included in Weisz et al. (2014); therefore, we use the end of star formation from Bettinelli et al. (2018). This is used as an indication of the duration of star formation.

[e] Median [Ba/Eu] measurements from the literature. See Figure 3.2 for detailed references.

[f] [Ba/Eu]$_{med}$ converted to the percentage of r-process contribution using r- and s-process abundances published by Simmerer et al. (2004), as described in Equation 3.1.

[g] Mean [Fe/H] from Kirby, Lanfranchi, et al. (2011) is weighted by the statistical uncertainty of each star.

[h] Number of stars that are members and have [Ba/Fe] measured in our catalog with errors less than 0.30 dex.

[i] Mean [Ba/Fe] of our catalog is weighted by the statistical uncertainty of each star.

[j] Number of unique stars that are members and have [Ba/Fe] measurements published in various papers. The SAGA Database (Suda et al., 2017) was primarily used to compile the literature values with recent papers added separately. This total does not include stars with upper/lower limits. See Figure 3.3 for specific references, except papers published after 2018 (e.g., Hill et al. 2019).

not been sufficient time for AGB stars to significantly contribute neutron-capture elements, and barium is instead an indicator of the r-process (e.g., Ji, Frebel, et al., 2016). Combining the knowledge currently available in the literature of the SFHs and [Ba/Eu] abundances for these dwarf galaxies confirms that AGB stars do not significantly contribute barium at early times ([Fe/H] $\lesssim -1.6$), and an r-process site is responsible for the majority of barium enrichment observed.

If the SFH is short, we will not see AGB stars contribute significantly because stars stopped forming before the bulk of the low-mass AGB stars evolved to the point of ejecting barium. Table 3.1 shows two independent tracers of the SFH: the average ages of the stars in the galaxies, $\langle \tau_{\rm SF} \rangle$, and the time at which 90% of the stars in the galaxy have been formed, τ_{90}. Both of these metrics confirm that although Fornax has had a comparably extended SFH, all of the other dwarf galaxies have short SFHs that could at most last 2–3 Gyrs. From the SFHs we would expect AGB stars to have the largest impact in Fornax because it has more extended star formation than the other dwarf galaxies. The contribution from AGB stars would only dominate the [Ba/Fe] trend in Sculptor, Ursa Minor, and Draco at late times (the iron-rich end), and therefore would not dominate barium production at low [Fe/H].

These conclusions are further confirmed by studying the [Ba/Eu] measurements found in the literature (see Figure 3.2). We convert these [Ba/Eu] ratios to the percentage of neutron-capture elements contributed by the r-process (f_r) using the pure r- and s-process abundances reported by Simmerer et al. (2004). Equation 3.1 describes this conversion. In this equation $N_{s/r} = 10^{\log \epsilon_{s/r}}$, where $\log \epsilon_{s/r}$ is from Table 10 in Simmerer et al. (2004), and f_r was restricted to remain between zero and one.

$$f_r([\mathrm{Ba/Eu}]) = \frac{\frac{N_{\mathrm{Eu}-s}}{N_{\mathrm{Ba}-s}} - 10^{-([\mathrm{Ba/Eu}]+(\mathrm{Ba/Eu})_\odot)}}{\frac{N_{\mathrm{Eu}-s}}{N_{\mathrm{Ba}-s}} - \frac{N_{\mathrm{Eu}-r}}{N_{\mathrm{Ba}-r}}} \tag{3.1}$$

The median r-process contribution in each galaxy is included in Table 3.1. The lowest r-process (i.e., the highest s-process) contributions occur in galaxies with the longest SFHs. Although we do see s-process (AGB) contribution dominate the barium contribution at higher [Fe/H] for Fornax and Sculptor, the [Ba/Eu] trends in most of these galaxies have [Ba/Eu] $\lesssim -0.4$ for [Fe/H] $\lesssim -1.6$. Sculptor is the exception to this statement (see Figure 3.2). A [Ba/Eu] value of -0.4 is equivalent to 54% of barium being contributed by the r-process. Therefore, AGB stars cannot be the dominant source of barium at early times ([Fe/H] $\lesssim -1.6$).

Isolating the R-Process Contribution of Barium

Although AGB stars are not the dominant source of barium at early times, we still need to remove their contribution to clearly study the r-process. To isolate the barium contributed by the r-process exclusively, we utilize the [Ba/Eu] measurements found in the literature to subtract the s-process contribution. We first fit a line to the [Ba/Eu] and [Fe/H] measurements found in the literature (see Figure 3.2). This line can be converted (via Equation 3.1) to the fraction of barium coming from the r-process (f_r). We can now convert [Ba/Fe] from our catalog (Figure 3.1) and the literature to include only the r-process component by $[\mathrm{Ba/Fe}]_r = [\mathrm{Ba/Fe}] + \log(f_r)$. These results are displayed in the right panels of Figure 3.3. Now that we have isolated the r-process component of barium, we can discuss the r-process barium trend that we observe.

3.5 New Critical Piece of Evidence of the Dominant R-Process Origin

The key result of this chapter is shown in Figure 3.3, where we compare [α/Fe] (specifically [Mg/Fe], Kirby, Guhathakurta, et al., 2010) as a function of [Fe/H] to the r-process component of [Ba/Fe] ($[\mathrm{Ba/Fe}]_r$) as a function of [Fe/H]. Barium results from both this catalog (black circles) and the literature values (blue) are displayed to utilize all the available information. Linear fits to Kirby, Guhathakurta, et al.'s and our catalog are shown in red with the slope of this fit printed for each galaxy. The trend is that [Mg/Fe] decreases with iron abundance because CCSNe contribute α elements before SNe Ia contribute large quantities of iron. However the barium abundances have slopes that are significantly more positive (even when accounting for the uncertainties of the slopes) for $[\mathrm{Fe/H}] \lesssim -1.6$. This can be seen in Sculptor, Draco, and Ursa Minor. When possible, we allowed the slope to differ for [Fe/H] greater than and less than -1.6. There were only enough stars above and below this [Fe/H] cutoff in Sculptor to allow this broken slope. The [Fe/H] cutoff of -1.6 was chosen because visually the slope of [Ba/Fe] vs. [Fe/H] changes in Sculptor at approximately this [Fe/H] abundance.

The fact that all of the galaxies in our sample simultaneously have a negative [Mg/Fe] vs. [Fe/H] slope and a significantly more positive $[\mathrm{Ba/Fe}]_r$ vs. [Fe/H] slope for $[\mathrm{Fe/H}] \lesssim -1.6$ leads to the conclusion that r-process barium is delayed relative to magnesium at early times. Therefore, Ba cannot come from the same source (CCSNe) as Mg.

The discrepant slopes of [Mg/Fe] and $[\mathrm{Ba/Fe}]_r$ vs. [Fe/H] are a powerful diagnostic

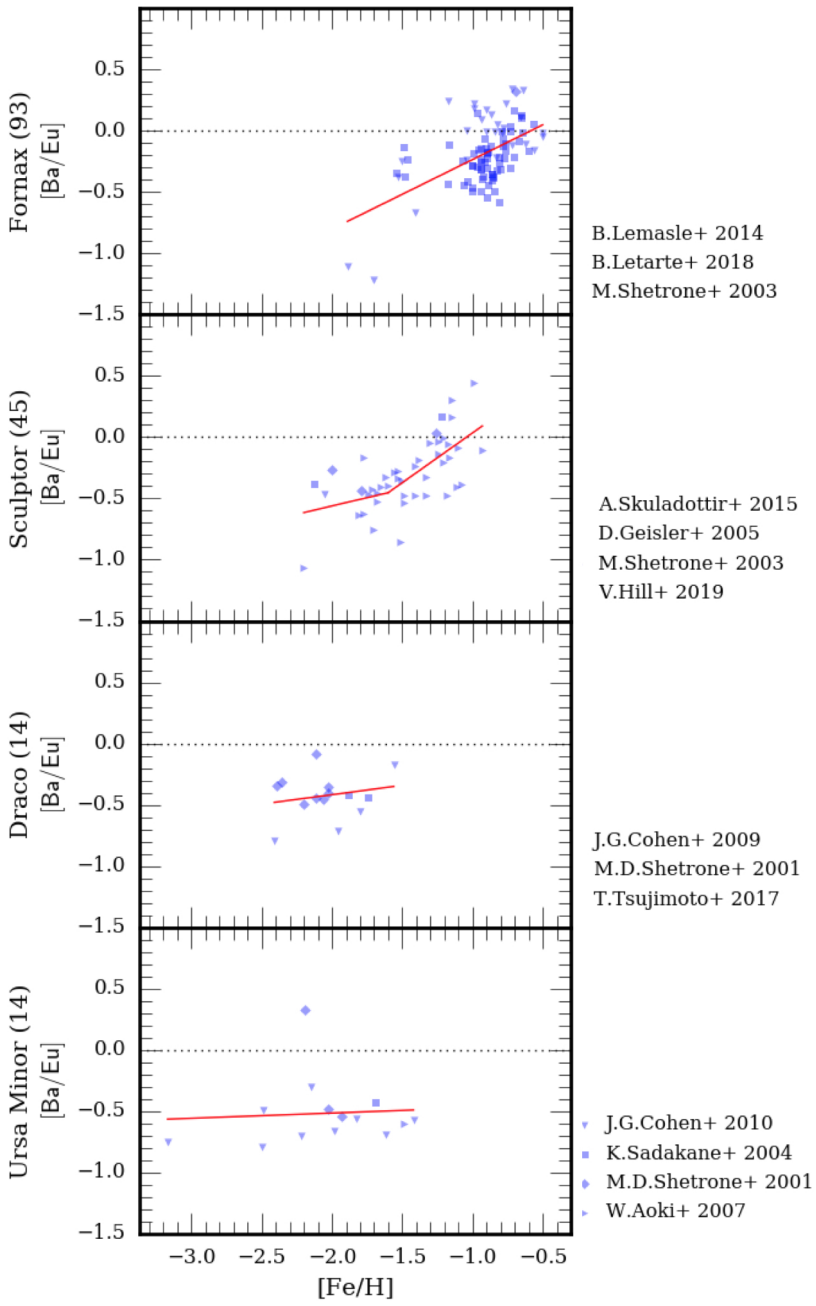

Figure 3.2: Literature [Ba/Eu] measurements for each galaxy. Sextans is not included because no [Ba/Eu] detections exist. A line ([Ba/Eu] = $A \times$ [Fe/H] + B) is fit to each galaxy's abundances to determine the fraction of barium contributed via the r-process.

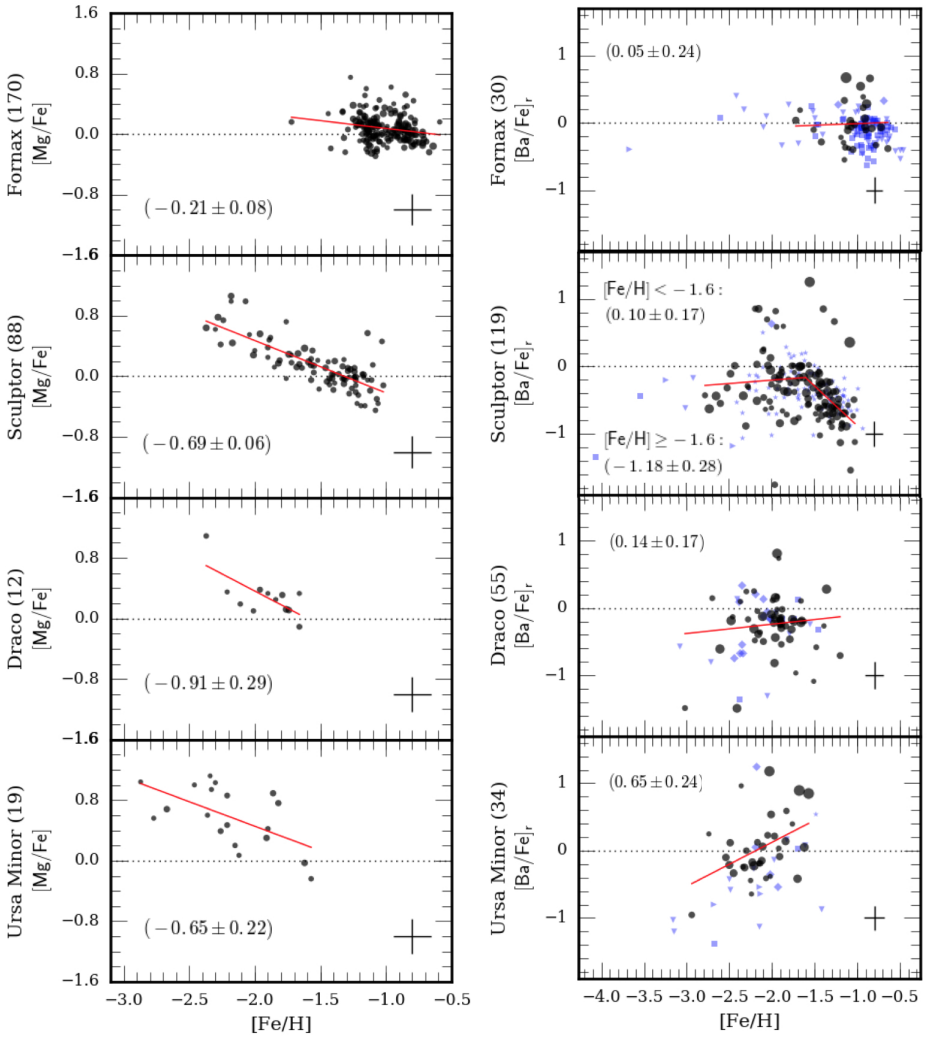

Figure 3.3: Comparison of the trend of [Mg/Fe] (Kirby, Guhathakurta, et al., 2010) and [Ba/Fe] created by the *r*-process ([Ba/Fe]$_r$) as a function of [Fe/H] for each galaxy. The current published [Ba/Fe] abundances (adjusted to include only the *r*-process component) are shown in blue with the corresponding reference listed on the side. Overplotted in black are our [Ba/Fe]$_r$ measurements. The sizes of the dots are inversely proportional to the errors, and the average errors for the stars plotted in each sub-figure are shown in the bottom right. The stars in black have abundance errors less than 0.28 dex and the total number plotted is listed in parentheses. A linear fit is shown in red, and the slope of this line is printed in the bottom left of each panel. The main conclusion is that [Mg/Fe] decreases as a function of [Fe/H] while [Ba/Fe] has a significantly more positive slope for low metallicities. This indicates that barium is contributed on a more delayed timescale than CCSNe.

feature of the r-process origin for a few different reasons. First, we are comparing consistent samples with the same techniques for these abundance measurements. Second, we are comparing abundance trends for the same galaxies. Therefore, both [Mg/Fe] and [Ba/Fe]$_r$ are subject to the same SFH, gas inflow/outflow history, and [Fe/H] trend with time. This removes the dependence of our conclusion on a galactic chemical evolution model and its myriad assumptions. Third, we see the discrepant slopes in multiple dwarf galaxies. This proves that we are seeing a global characteristic of the r-process.

Our observation of a significantly more positive slope of [Ba/Fe]$_r$ vs. [Fe/H] than [α/Fe]for low iron abundances ([Fe/H] $\lesssim -1.6$) in several dwarf galaxies, requires that the timescale for barium is substantially more delayed than the timescale for magnesium. We now consider the possible origins for barium and which source would cause the observed trends.

3.6 NSMs Could Be the Dominant Source of Barium in Dwarf Galaxies

We have concluded that dwarf galaxies are dominated by a r-process source with a timescale more delayed than CCSNe at early times ([Fe/H] $\lesssim -1.6$). Compared to ultra-faint dwarfs (Ji, Frebel, et al., 2016; Hansen et al., 2017), our sample of classical dwarf galaxies is able to probe the characteristics of an ensemble of r-process enrichment rather than isolated events. This evidence includes information about the timescale of enrichment, which enables us to distinguish whether MRSNe or NSMs are the dominant source of r-process enrichment in dwarf galaxies at early times.

First we will consider MRSNe. All CCSNe have a short lifetime, so they would cause the same negative trend that we see in the α elements, which are also released by CCSNe. Because we observe a significantly more positive [Ba/Fe]$_r$ vs. [Fe/H] slope, we can rule out MRSNe as the dominant source of barium in these dwarf galaxies.

Instead, we need a delayed barium enrichment to create a more positive [Ba/Fe]$_r$ vs. [Fe/H] slope when compared to the [Mg/Fe] vs. [Fe/H] slope. A flat [Ba/Fe]$_r$ vs. [Fe/H] trend would indicate that the r-process enrichment needs to occur on a timescale similar to SNe Ia because barium would need to be ejected into the ISM while SNe Ia are ejecting large amounts of iron. Although we see a clear increasing [Ba/Fe]$_r$ vs. [Fe/H] trend in Ursa Minor and a flat or slightly rising trend in Draco, Sculptor has a slightly negative trend for [Fe/H] $\lesssim -1.6$. It is therefore ambiguous

when the r-process enrichment needs to occur compared to SNe Ia timescales. However, we can definitively say that the timescale needs to be delayed compared to CCSNe in order to create the significantly more positive [Ba/Fe]$_r$ vs. [Fe/H] slope. Based on our observations, NSMs are the most viable source of barium enrichment in dwarf galaxies at early times. Simulations and the LIGO observation support NSMs producing r-process elements (e.g., Goriely, Bauswein, and Janka, 2011; Abbott et al., 2017; B. Côté et al., 2017).

In conclusion, our observations are matched by a source that releases barium on a timescale more delayed than CCSNe at early times. Of the sources suggested so far, neutron star mergers are the only source that satisfies this condition.

3.7 Implications

The early chemical evolution of dwarf galaxies can be used to constrain the yield and/or rate of NSMs, which we will address with a galactic chemical evolution model in a future paper. We have concluded that r-process enrichment is dominated by NSMs in the early evolution of dwarf galaxies. It is tempting to extrapolate this conclusion and apply this directly to comment on the dominant site of r-process enrichment in later evolution of dwarf galaxies and larger galaxies (such as the Milky Way).

However, we exhort readers to extrapolate to high [Fe/H] with caution. The rate of NSMs that have ejected material retained in the galaxy (and the yield or amount of ejected material that is retained per NSM) may depend on the age of the binary neutron star system and/or mass of the galaxy. To discuss the r-process trends seen in the literature at higher iron abundances, we turn to [Eu/Fe] as an indicator of the r-process, because the s-process is increasingly important in barium productions at these times. For example, Hill et al. (2019) find a declining [Eu/Fe] vs. [Fe/H] trend (see Figure 13 in Tolstoy, Hill, and Tosi 2009) in Sculptor at [Fe/H] $\gtrsim -1.6$. Comparisons to the Milky Way are more challenging due to the drastically different mass and merger history. Milky Way halo stars are largely a compilation of stars stripped from dwarf galaxies. It is therefore unsurprising that there is a large spread in [Eu/Fe]. In Milky Way disk stars ([Fe/H] $\gtrsim -1.0$) a declining [Eu/Fe] vs. [Fe/H] trend is also observed (Battistini and Bensby, 2016).

This transition from positive [r-process/Fe] vs. [Fe/H] trends at low metallicities to a declining trend at higher metallicities presents a puzzle. Although some attribute this to MRSNe (Tsujimoto and Nishimura, 2015), another possible explanation is that

NSM natal kicks cause the effective NSM rate (rate of NSMs contributing enriched material to the ISM) to decrease significantly at later times as the NSMs occur far from the galaxy (e.g., Willems and Kalogera, 2004; Bramante and Linden, 2016; Beniamini, Hotokezaka, and Piran, 2016; Safarzadeh and Scannapieco, 2017). It is important to note that the velocities of these NSM natal kicks are still unknown, and it is possible that they are large enough to remove the neutron star binary from the galaxy before a NSM can occur. Moderate NSM natal kicks that allow early NSMs to occur in the galaxy and late NSMs occur outside the galaxy would be consistent with our $[\mathrm{Ba/Fe}]_r$ measurements, specifically the significant decrease in $[\mathrm{Ba/Fe}]_r$ vs. [Fe/H] slope seen in Sculptor above and below $[\mathrm{Fe/H}] = -1.6$). Additional detections of [Eu/Fe] with $[\mathrm{Fe/H}] \lesssim -1.6$ and modeling of NSM natal kicks would be able to confirm the plausibility of this explanation.

3.8 Summary

Here we highlight the main conclusions of this chapter.

- We have confirmed medium-resolution spectroscopy as a reliable method of measuring barium.
- We have obtained the largest sample of barium abundances in dwarf galaxies.
- We have discovered that the majority of barium in dwarf galaxies is created by a delayed r-process source at early times.
- We conclude that neutron star mergers are the most likely source of barium enrichment in dwarf galaxies at early times.

In a subsequent paper we will use galactic chemical evolution models to derive qualitative conclusions concerning the sources of barium enrichment in dwarf galaxies. Specifically, we will constrain the NSM yields/rates needed to match our observations.

ACKNOWLEDGEMENTS

This material is based upon work supported by the National Science Foundation Graduate Research Fellowship under Grant No. DGE-1745301 and the National Science Foundation under Grant No. AST-1614081. We thank Alexander Ji for insightful conversation.

Facility: Keck:II (DEIMOS).

Software: MOOG (Sneden, 1973), spec2d pipeline (Cooper et al., 2012; Newman et al., 2013), scipy (Jones, Oliphant, Peterson, et al., 2001).

References

Abbott, B. P. et al. (2017). "GW170817: Observation of Gravitational Waves from a Binary Neutron Star Inspiral". In: *Physical Review Letters* 119.16, 161101, p. 161101. DOI: 10.1103/PhysRevLett.119.161101. arXiv: 1710.05832 [gr-qc].

Aoki, W., N. Arimoto, et al. (2009). "Chemical composition of extremely metal-poor stars in the Sextans dwarf spheroidal galaxy". In: *A&A* 502, pp. 569–578. DOI: 10.1051/0004-6361/200911959. arXiv: 0904.4307.

Aoki, W., S. Honda, et al. (2007). "First Determination of the Actinide Thorium Abundance for a Red Giant of the Ursa Minor Dwarf Galaxy". In: *PASJ* 59, pp. L15–L19. DOI: 10.1093/pasj/59.3.L15. arXiv: 0704.3104.

Battistini, C. and T. Bensby (2016). "The origin and evolution of r- and s-process elements in the Milky Way stellar disk". In: *A&A* 586, A49, A49. DOI: 10.1051/0004-6361/201527385. arXiv: 1511.00966 [astro-ph.SR].

Beniamini, P., K. Hotokezaka, and T. Piran (2016). "Natal Kicks and Time Delays in Merging Neutron Star Binaries: Implications for r-process Nucleosynthesis in Ultra-faint Dwarfs and in the Milky Way". In: *ApJL* 829, L13, p. L13. DOI: 10.3847/2041-8205/829/1/L13. arXiv: 1607.02148 [astro-ph.HE].

Bensby, T., S. Feltzing, and M. S. Oey (2014). "Exploring the Milky Way stellar disk. A detailed elemental abundance study of 714 F and G dwarf stars in the solar neighbourhood". In: *A&A* 562, A71, A71. DOI: 10.1051/0004-6361/201322631. arXiv: 1309.2631.

Bettinelli, M. et al. (2018). "The star formation history of the Sextans dwarf spheroidal galaxy: a true fossil of the pre-reionization era". In: *MNRAS* 476, pp. 71–79. DOI: 10.1093/mnras/sty226. arXiv: 1801.08145.

Bramante, J. and T. Linden (2016). "On the r-process Enrichment of Dwarf Spheroidal Galaxies". In: *ApJ* 826, 57, p. 57. DOI: 10.3847/0004-637X/826/1/57. arXiv: 1601.06784 [astro-ph.HE].

Cohen, J. G. and W. Huang (2009). "The Chemical Evolution of the Draco Dwarf Spheroidal Galaxy". In: *ApJ* 701, pp. 1053–1075. DOI: 10.1088/0004-637X/701/2/1053. arXiv: 0906.1006 [astro-ph.GA].

– (2010). "The Chemical Evolution of the Ursa Minor Dwarf Spheroidal Galaxy". In: *ApJ* 719, pp. 931–949. DOI: 10.1088/0004-637X/719/1/931. arXiv: 1006.3538.

Cooper, M. C. et al. (2012). *spec2d: DEEP2 DEIMOS Spectral Pipeline*. Astrophysics Source Code Library. ascl: 1203.003.

Côté, B. et al. (2017). "Advanced LIGO Constraints on Neutron Star Mergers and r-process Sites". In: *ApJ* 836, 230, p. 230. DOI: 10.3847/1538-4357/aa5c8d. arXiv: 1610.02405.

Escala, I. et al. (2018). "Modelling chemical abundance distributions for dwarf galaxies in the Local Group: the impact of turbulent metal diffusion". In: *MNRAS* 474, pp. 2194–2211. DOI: 10.1093/mnras/stx2858. arXiv: 1710.06533.

Faber, S. M. et al. (2003). "The DEIMOS spectrograph for the Keck II Telescope: integration and testing". In: *Instrument Design and Performance for Optical/Infrared Ground-based Telescopes*. Ed. by M. Iye and A. F. M. Moorwood. Vol. 4841. Proc. SPIE, pp. 1657–1669. DOI: 10.1117/12.460346.

Geisler, D. et al. (2005). ""Sculptor-ing" the Galaxy? The Chemical Compositions of Red Giants in the Sculptor Dwarf Spheroidal Galaxy". In: *AJ* 129, pp. 1428–1442. DOI: 10.1086/427540. eprint: astro-ph/0412065.

Gilmore, G. and R. F. G. Wyse (1991). "Chemical evolution with bursts of star formation - Element ratios in dwarf galaxies". In: *ApJL* 367, pp. L55–L58. DOI: 10.1086/185930.

Goriely, S., A. Bauswein, and H.-T. Janka (2011). "r-process Nucleosynthesis in Dynamically Ejected Matter of Neutron Star Mergers". In: *ApJL* 738, L32, p. L32. DOI: 10.1088/2041-8205/738/2/L32. arXiv: 1107.0899 [astro-ph.SR].

Hansen, T. T. et al. (2017). "An r-process Enhanced Star in the Dwarf Galaxy Tucana III". In: *ApJ* 838, 44, p. 44. DOI: 10.3847/1538-4357/aa634a. arXiv: 1702.07430 [astro-ph.SR].

Hill, V. et al. (2019). "VLT/FLAMES high-resolution chemical abundances in Sculptor: a textbook dwarf spheroidal galaxy". In: *A&A* 626, A15, A15. DOI: 10.1051/0004-6361/201833950. arXiv: 1812.01486 [astro-ph.GA].

Honda, S. et al. (2011). "Enrichment of Heavy Elements in the Red Giant S 15-19 in the Sextans Dwarf Spheroidal Galaxy". In: *PASJ* 63, pp. 523–529. DOI: 10.1093/pasj/63.sp2.S523. arXiv: 1103.1956 [astro-ph.SR].

Iwamoto, K. et al. (1999). "Nucleosynthesis in Chandrasekhar Mass Models for Type IA Supernovae and Constraints on Progenitor Systems and Burning-Front Propagation". In: *ApJS* 125, pp. 439–462. DOI: 10.1086/313278. eprint: astro-ph/0002337.

Jablonka, P. et al. (2015). "The early days of the Sculptor dwarf spheroidal galaxy". In: *A&A* 583, A67, A67. DOI: 10.1051/0004-6361/201525661. arXiv: 1506.08636.

Ji, A. P. and A. Frebel (2018). "From Actinides to Zinc: Using the Full Abundance Pattern of the Brightest Star in Reticulum II to Distinguish between Different r-process Sites". In: *ApJ* 856, 138, p. 138. DOI: 10.3847/1538-4357/aab14a. arXiv: 1802.07272 [astro-ph.SR].

Ji, A. P., A. Frebel, et al. (2016). "R-process enrichment from a single event in an ancient dwarf galaxy". In: *Nature* 531, pp. 610–613. DOI: 10.1038/nature17425. arXiv: 1512.01558.

Jones, Eric, Travis Oliphant, Pearu Peterson, et al. (2001). *SciPy: Open source scientific tools for Python*. [Online; accessed 2017-01-16]. URL: http://www.scipy.org/.

Karakas, A. I. and J. C. Lattanzio (2014). "The Dawes Review 2: Nucleosynthesis and Stellar Yields of Low- and Intermediate-Mass Single Stars". In: *PASA* 31, e030, e030. DOI: 10.1017/pasa.2014.21. arXiv: 1405.0062 [astro-ph.SR].

Karakas, A. I., M. Lugaro, et al. (2018). "Heavy-element yields and abundances of asymptotic giant branch models with a Small Magellanic Cloud metallicity". In: *MNRAS* 477, pp. 421–437. DOI: 10.1093/mnras/sty625. arXiv: 1803.02028 [astro-ph.SR].

Kirby, E. N., J. S. Bullock, et al. (2014). "The dynamics of isolated Local Group galaxies". In: *MNRAS* 439, pp. 1015–1027. DOI: 10.1093/mnras/stu025. arXiv: 1401.1208.

Kirby, E. N., J. G. Cohen, et al. (2011). "Multi-element Abundance Measurements from Medium-resolution Spectra. IV. Alpha Element Distributions in Milky Way Satellite Galaxies". In: *ApJ* 727, 79, p. 79. DOI: 10.1088/0004-637X/727/2/79. arXiv: 1011.5221 [astro-ph.GA].

Kirby, E. N., P. Guhathakurta, et al. (2010). "Multi-element Abundance Measurements from Medium-resolution Spectra. II. Catalog of Stars in Milky Way Dwarf Satellite Galaxies". In: *ApJS* 191, pp. 352–375. DOI: 10.1088/0067-0049/191/2/352. arXiv: 1011.4516 [astro-ph.GA].

Kirby, E. N., G. A. Lanfranchi, et al. (2011). "Multi-element Abundance Measurements from Medium-resolution Spectra. III. Metallicity Distributions of Milky Way Dwarf Satellite Galaxies". In: *ApJ* 727, 78, p. 78. DOI: 10.1088/0004-637X/727/2/78. arXiv: 1011.4937 [astro-ph.GA].

Lemasle, B. et al. (2014). "VLT/FLAMES spectroscopy of red giant branch stars in the Fornax dwarf spheroidal galaxy". In: *A&A* 572, A88, A88. DOI: 10.1051/0004-6361/201423919. arXiv: 1409.7703.

Letarte, B. et al. (2018). "A high-resolution VLT/FLAMES study of individual stars in the centre of the Fornax dwarf spheroidal galaxy (Corrigendum)". In: *A&A* 613, p. C1. DOI: 10.1051/0004-6361/200913413e. URL: https://doi.org/10.1051/0004-6361/200913413e.

Maoz, D. and O. Graur (2017). "Star Formation, Supernovae, Iron, and α: Consistent Cosmic and Galactic Histories". In: *ApJ* 848, 25, p. 25. DOI: 10.3847/1538-4357/aa8b6e. arXiv: 1703.04540 [astro-ph.HE].

Newman, J. A. et al. (2013). "The DEEP2 Galaxy Redshift Survey: Design, Observations, Data Reduction, and Redshifts". In: *ApJS* 208, 5, p. 5. DOI: 10.1088/0067-0049/208/1/5. arXiv: 1203.3192.

Nomoto, K. et al. (2006). "Nucleosynthesis yields of core-collapse supernovae and hypernovae, and galactic chemical evolution". In: *Nuclear Physics A* 777, pp. 424–458. DOI: 10.1016/j.nuclphysa.2006.05.008. eprint: astro-ph/0605725.

Orban, C. et al. (2008). "Delving Deeper into the Tumultuous Lives of Galactic Dwarfs: Modeling Star Formation Histories". In: *ApJ* 686, 1030-1044, pp. 1030–1044. DOI: 10.1086/591496. arXiv: 0805.1058.

Sadakane, K. et al. (2004). "Subaru/HDS Abundances in Three Giant Stars in the Ursa Minor Dwarf Spheroidal Galaxy". In: *PASJ* 56, pp. 1041–1058. DOI: 10.1093/pasj/56.6.1041. eprint: astro-ph/0411332.

Safarzadeh, M. and E. Scannapieco (2017). "Simulating neutron star mergers as r-process sources in ultrafaint dwarf galaxies". In: *MNRAS* 471, pp. 2088–2096. DOI: 10.1093/mnras/stx1706. arXiv: 1707.01909.

Shetrone, M. D., P. Côté, and W. L. W. Sargent (2001). "Abundance Patterns in the Draco, Sextans, and Ursa Minor Dwarf Spheroidal Galaxies". In: *ApJ* 548, pp. 592–608. DOI: 10.1086/319022. eprint: astro-ph/0009505.

Shetrone, M. et al. (2003). "VLT/UVES Abundances in Four Nearby Dwarf Spheroidal Galaxies. I. Nucleosynthesis and Abundance Ratios". In: *AJ* 125, pp. 684–706. DOI: 10.1086/345966. eprint: astro-ph/0211167.

Simmerer, J. et al. (2004). "The Rise of the s-Process in the Galaxy". In: *ApJ* 617, pp. 1091–1114. DOI: 10.1086/424504. eprint: astro-ph/0410396.

Simon, J. D. et al. (2015). "Chemical Signatures of the First Supernovae in the Sculptor Dwarf Spheroidal Galaxy". In: *ApJ* 802, 93, p. 93. DOI: 10.1088/0004-637X/802/2/93. arXiv: 1412.5176.

Skúladóttir, Á. et al. (2015). "The first carbon-enhanced metal-poor star found in the Sculptor dwarf spheroidal". In: *A&A* 574, A129, A129. DOI: 10.1051/0004-6361/201424782. arXiv: 1411.7956.

Sneden, C. A. (1973). "Carbon and Nitrogen Abundances in Metal-Poor Stars." PhD thesis. THE UNIVERSITY OF TEXAS AT AUSTIN.

Starkenburg, E. et al. (2013). "The extremely low-metallicity tail of the Sculptor dwarf spheroidal galaxy". In: *A&A* 549, A88, A88. DOI: 10.1051/0004-6361/201220349. arXiv: 1211.4592.

Suda, T. et al. (2017). "Stellar Abundances for Galactic Archaeology Database. IV. Compilation of stars in dwarf galaxies". In: *PASJ* 69, 76, p. 76. DOI: 10.1093/pasj/psx059. arXiv: 1703.10009.

Tafelmeyer, M. et al. (2010). "Extremely metal-poor stars in classical dwarf spheroidal galaxies: Fornax, Sculptor, and Sextans". In: *A&A* 524, A58, A58. DOI: 10.1051/0004-6361/201014733. arXiv: 1008.3721 [astro-ph.SR].

Tinsley, B. M. (1980). "Evolution of the Stars and Gas in Galaxies". In: *FCPh* 5, pp. 287–388.

Tolstoy, E., V. Hill, and M. Tosi (2009). "Star-Formation Histories, Abundances, and Kinematics of Dwarf Galaxies in the Local Group". In: *ARA&A* 47, pp. 371–425. DOI: 10.1146/annurev-astro-082708-101650. arXiv: 0904.4505 [astro-ph.CO].

Tsujimoto, T., T. Matsuno, et al. (2017). "Enrichment in r-process Elements from Multiple Distinct Events in the Early Draco Dwarf Spheroidal Galaxy". In: *ApJL* 850, L12, p. L12. DOI: 10.3847/2041-8213/aa9886. arXiv: 1711.02121 [astro-ph.SR].

Tsujimoto, T. and N. Nishimura (2015). "The r-process in Magnetorotational Supernovae". In: *ApJL* 811, L10, p. L10. DOI: 10.1088/2041-8205/811/1/L10. arXiv: 1509.00004.

Ural, U. et al. (2015). "An inefficient dwarf: chemical abundances and the evolution of the Ursa Minor dwarf spheroidal galaxy". In: *MNRAS* 449, pp. 761–770. DOI: 10.1093/mnras/stv294. arXiv: 1502.04133.

Venn, K. A. et al. (2004). "Stellar Chemical Signatures and Hierarchical Galaxy Formation". In: *AJ* 128, pp. 1177–1195. DOI: 10.1086/422734. eprint: astro-ph/0406120.

Weisz, D. R. et al. (2014). "The Star Formation Histories of Local Group Dwarf Galaxies. II. Searching For Signatures of Reionization". In: *ApJ* 789, 148, p. 148. DOI: 10.1088/0004-637X/789/2/148. arXiv: 1405.3281.

Willems, B. and V. Kalogera (2004). "Constraints on the Formation of PSR J0737-3039: The Most Probable Isotropic Kick Magnitude". In: *ApJL* 603, pp. L101–L104. DOI: 10.1086/383200. eprint: astro-ph/0312426.

Woo, J., S. Courteau, and A. Dekel (2008). "Scaling relations and the fundamental line of the local group dwarf galaxies". In: *MNRAS* 390, pp. 1453–1469. DOI: 10.1111/j.1365-2966.2008.13770.x. arXiv: 0807.1331.

Chapter 4

QUANTITATIVE CONSTRAINTS ON THE R-PROCESS IN DWARF GALAXIES FROM A GALACTIC CHEMICAL EVOLUTION MODEL

4.1 Introduction

It is a challenge to distinguish which of the proposed *r*-process candidate sites produced the observed *r*-process enrichment in galaxies. We tackle this question by using a galactic chemical evolution (GCE) model to match the continual build-up of *r*-process elements seen in our recently published catalog of dwarf galaxy abundances (Chapter 2).

Several studies (e.g., van de Voort et al. 2019; Shen et al. 2015; Naiman et al. 2018; Benoit Côté, Eichler, et al. 2019 and Hotokezaka, Beniamini, and Piran 2018) have used [Eu/Fe] measurements of Milky Way disk and halo stars to study the *r*-process. However, the Milky Way is a chaotic environment. Its extended SFH and complex accretion history obfuscate the interpretation of detailed abundance ratios. In an alternative approach, we look for *r*-process signatures in the simplest galaxies. Intact dwarf galaxies are simpler systems than the Milky Way halo (which includes stripped dwarf galaxies) and disk (which has experienced major mergers with other galaxies). The abundances of stars in dwarf galaxies are more difficult to obtain than the abundances of stars in our galaxy, because the dwarf galaxies lie at greater distances. However, the difficulty in observation is accompanied by a simplicity of interpretation. The stars in dwarf galaxies share a common history (e.g., of star formation, outflows, inflows). This enables a more accurate determination of NSM yields and rates than previous studies.

We have assembled the largest sample (almost 250 stars) of measurements of the *r*-process element barium in dwarf galaxies to date. Our catalog of [Fe/H], [α/Fe], and [Ba/Fe] for several dwarf galaxies allows us to test the possible origins of the *r*-process by seeing whether the proposed amounts and timescales of these contributions can match the observations. Specifically, we test if CCSNe (including rare MRSNe) or NSMs are the dominant source of *r*-process. Our method is sensitive to the clearest observational difference of CCSNe and NSMs: how quickly these events occur after the stars are born.

Many studies have used hydrodynamic simulations to study the chemical enrichment of dwarf galaxies. FIRE (e.g., Wheeler et al., 2015) and other (e.g., Revaz et al., 2016) simulations of dwarf galaxies are used to study galaxy properties with state-of-the-art physics implementations (feedback, inflows, outflows, mixing, etc.). The chemical trends of FIRE simulations can tell us about metal mixing in dwarf galaxies (Escala et al., 2018). Hydrodynamic simulations of dwarf galaxies have incorporated r-process elements in several recent studies (e.g., Safarzadeh and Scannapieco, 2017; Hirai, Wanajo, and Saitoh, 2019). However, these simulations are very computationally expensive, so a large investment is required to test many different options (yields, rates, and delay-time distributions—DTDs) for r-process contributions.

We use an analytic model (similar to models used in Benoit Côté, Eichler, et al. 2019 and Hotokezaka, Beniamini, and Piran 2018) to quickly explore various s- and r-process ejection models. We test if NSMs are even needed by increasing the predicted AGB and CCSN yields to see if they can match the trend of abundance ratios vs. metallicity for four different dwarf galaxies simultaneously. Finally, we test what level of NSM contribution is needed to match the observations. The end-goal of this research is to also test various DTDs of NSMs. The main benefits of using an analytic model is that it is computationally inexpensive, is simple enough to interpret which variable causes what impact, and which variables are required to match the observations are easy to see.

I discuss the details of our one-zone GCE model and the preliminary results that suggest a large r-process contribution from NSMs is required to reproduce the barium trends we observe in dwarf galaxies, especially at early times.

4.2 Main Assumptions and Equations

Our GCE model takes several free parameters as inputs and returns chemical abundance trends. The model has a very short computation time (tens of seconds) allowing for careful determination of parameter uncertainties through Markov Chain Monte Carlo (MCMC) analysis. It is a one-zone model and that one zone encompasses the entire galaxy and the nearby circumgalactic medium. Adjustments have been made to the GCE model used in Kirby et al. (2011) to track barium, alter the initial mass function (IMF), and vary the s- and r-process yields.

Our model tracks the total gas mass of the galaxy as a function of time (Equation 4.1). There are six free parameters in this model (A_*, α, $A_{\rm in}$, $\tau_{\rm in}$, $A_{\rm out}$, and $M_{\rm gas}(0)$),

which are highlighted in blue in the equations below. The first term of the complete chemical evolution equation ($M_{\rm gas}(0)$) is a free parameter and represents the initial gas mass of the galaxy. The star formation rate (SFR) is calculated from the original Schmidt law ($\dot{\xi}_*$, Equation 4.2, Schmidt, 1959). The functional form of the primordial gas infall rate ($\dot{\xi}_{\rm in}$, Equation 4.3) is selected to match the smooth rise and fall of the metallicity distribution function and happens to be the same form that describes dark matter accreting onto a halo (Wechsler et al., 2002). Gas outflow ($\dot{\xi}_{\rm out}$, Equation 4.4) is the material that is permanently ejected from the galaxy by supernovae. Nucleosynthetic yields ($\dot{\xi}_{\rm yield}$) are considered from AGB stars, supernovae, and (eventually) NSMs (Equations 4.5 and 4.7).

$$\xi(t) = M_{\rm gas}(0) + \int_0^t (-\dot{\xi}_* + \dot{\xi}_{\rm in} - \dot{\xi}_{\rm out} + \dot{\xi}_{\rm yield})\, dt \tag{4.1}$$

$$\dot{\xi}_* = A_* \left(\frac{M_{\rm gas}(t)}{10^6 M_\odot} \right)^{\alpha} \tag{4.2}$$

$$\dot{\xi}_{\rm in} = A_{\rm in} \left(\frac{t}{\rm Gyr} \right) e^{-t/\tau_{\rm in}} \tag{4.3}$$

$$\dot{\xi}_{\rm out} = A_{\rm out}(\dot{N}_{\rm II} + \dot{N}_{\rm Ia}) \tag{4.4}$$

$$\dot{\xi}_{\rm yield,\ initial} = \dot{\xi}_{\rm AGB} + \dot{\xi}_{\rm SNII} + \dot{\xi}_{\rm SNIa} \tag{4.5}$$

$$\Psi_{\rm Ia} = \begin{cases} 0 & t_{\rm delay} < 0.1\,{\rm Gyr} \\ A_{\rm Ia} \times \left(\frac{t_{\rm delay}}{\rm Gyr} \right)^{-1.1} & t_{\rm delay} \geq 0.1\,{\rm Gyr} \end{cases} \tag{4.6}$$

The units of $\dot{\xi}$, $A_{\rm in}$, and A_* are $\rm M_\odot\ yr^{-1}$, the units of $\dot{N}$ is $\rm yr^{-1}$, and the units of ξ, $M_{\rm gas}(0)$, and $A_{\rm out}$ are $\rm M_\odot$. The normalization of the SN Ia DTD, $A_{\rm Ia}$, has units of $\rm SNIa\,Gyr^{-1}\,M_\odot^{-1}$. The exponent α is dimensionless.

Here is an overview of how the GCE model returns abundance trends. Combining the SFH (panel a in Figure 4.1) with an IMF and the delay-times results in the rate of each event as a function of time (i.e., event frequency, panel b). Delayed recycling (assuming that stars release enriched material after a time delay) is essential for

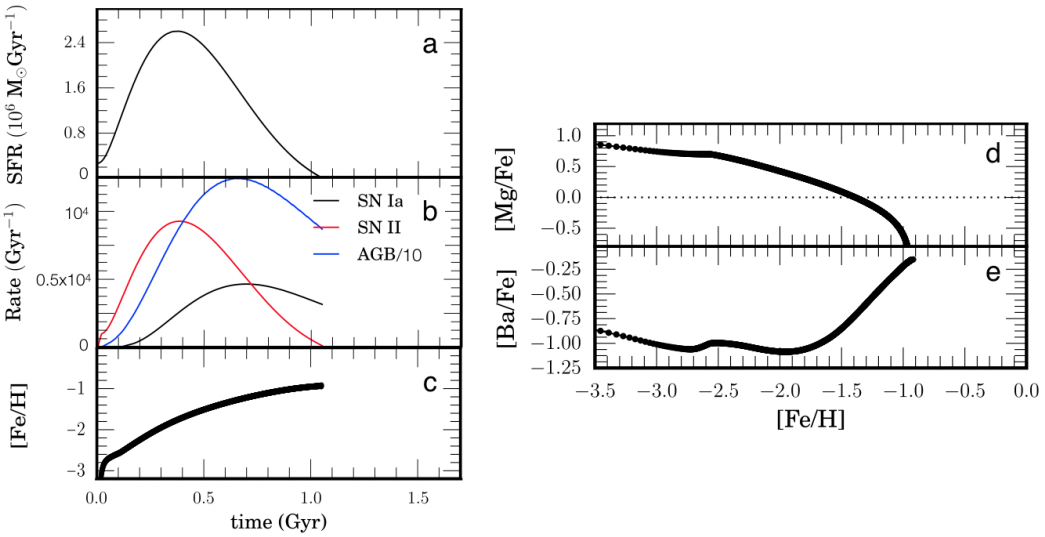

Figure 4.1: Example of our default GCE model for Sculptor without including NSMs. This depicts the SFH (panel a), event frequency (panel b), stellar metallicity as a function of time (panel c), and the resulting abundance ratios as a function of metallicity (panel d and e).

determining the *r*-process delay-time from abundance ratios. For SNe Ia we use Maoz, Sharon, and Gal-Yam (2010)'s formula shown in Equation 4.6 (where $A_{\rm Ia} = 10^{-3}$ SNIa Gyr^{-1} $M_\odot^{-1}$). The delay-time of CCSNe and AGB stars is determined from stellar lifetime equations (Padovani and Matteucci, 1993; Kodama, 1997). One of the results of the model is a relation between [Fe/H] and time (panel c). This effectively turns our chemical abundance trend into a chemical clock. Finally, the chemical yield models of each event translate the event frequency into abundance ratios (panel d and e). These abundance trends returned by the model are then iteratively fitted with the observed abundances for each galaxy using MCMC analysis.

Yields

The following yield models are used: SNe Ia (Iwamoto et al., 1999), SNe II (Nomoto et al., 2006; H. Li et al., 2014), and AGB stars (one model by Cristallo et al. 2015 and one by Fishlock et al. 2014 and Karakas and Lugaro 2016)—see Figure 4.2, 4.3, and 4.4. I have referenced H. Li et al. (2014) for the barium yield from SNe II. This estimates a few $\times 10^{-8}$ $M_\odot$ of barium per SNe II. H. Li et al. (2014) attributed this barium yield to the *r*-process, but the *s*-process in massive rotating stars (Cescutti et al., 2015) reports the same levels of barium ejecta. In our current model, we leave it ambiguous if this small barium contribution from CCSNe comes from the *s*- or *r*-process. Regardless, in Figure 4.1 panel e, the barium is coming predominately

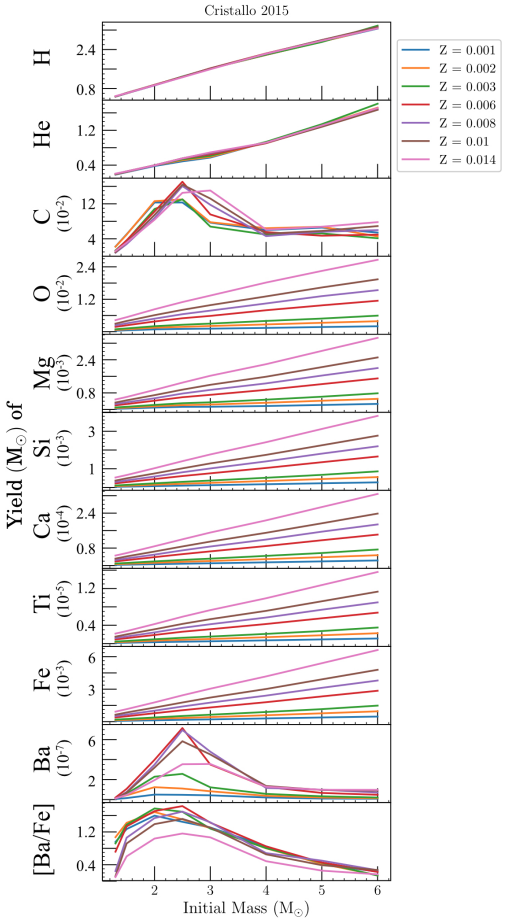

Figure 4.2: AGB yield models from Cristallo et al. (2015). Each plot shows the yields for a different element, and each line represents the yields for a given metallicity. C and Ba are the main elements created by AGB stars.

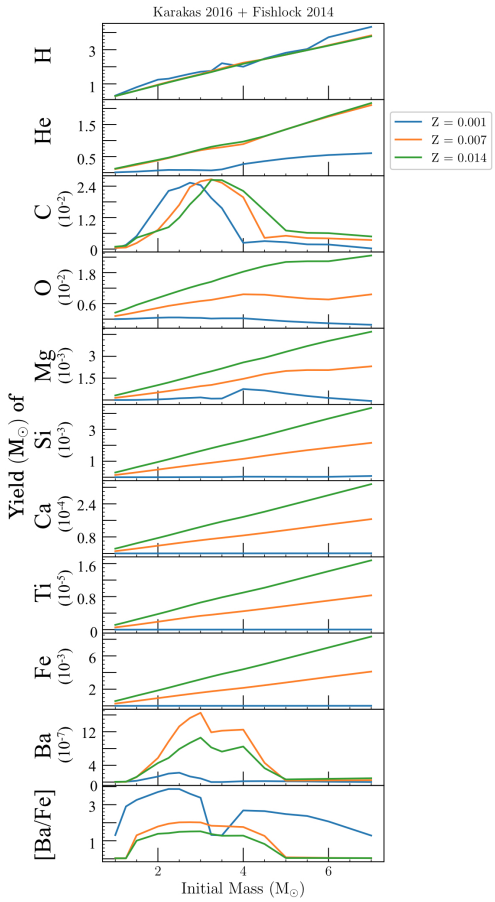

Figure 4.3: AGB yield models from Karakas and Lugaro (2016) and Fishlock et al. (2014). These two papers published AGB models at different metallicites. See Figure 4.2 for a description. These "Karakas" yields are the default AGB yields used in our GCE model and agree with the yields in Cristallo et al. (2015) within a factor of 2–4.

from AGB stars. The GCE model in Figure 4.5 only includes yields from SNe II, SNe Ia, and AGB stars. However, we will see in Section 4.3 that an additional source of barium is required (i.e., NSMs) to match the observed [Ba/Fe] measurements.

Consequences of Assumptions

Here we outline the main assumptions in our GCE model and the corresponding theoretical and observational evidence.

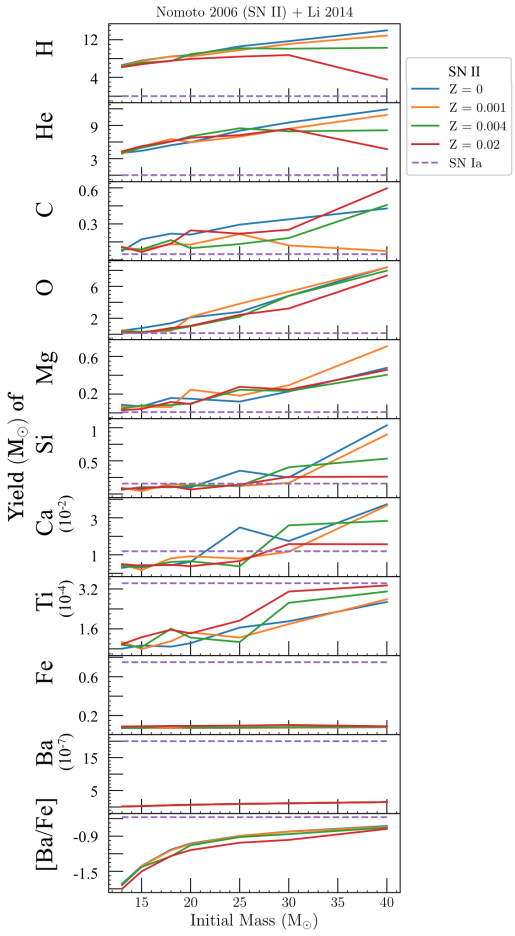

Figure 4.4: Supernova yield models from various papers. See Figure 4.2 for a description. SN II yields are from Nomoto et al. (2006)—except for barium, which is from H. Li et al. (2014). SN Ia yields are from Iwamoto et al. (1999)—except for barium, where an value of $2 \times 10^{-6}\,M_\odot$ per SN Ia is shown as a contribution from NSMs. Note, this is less than the NSM yield shown in Figure 4.9.

- Metal Mixing: The GCE model has one zone and therefore assumes complete metal mixing within our 10 Myr timestep once the elements are ejected into the ISM. Dwarf galaxies have efficient mixing for [Fe/H] and [α/Fe]. This has been verified by simulations (Emerick et al., 2018) and observations (Escala et al., 2018).

  However, there has been evidence that neutron-capture elements are less well-mixed. Simulations have found more scatter in [Ba/Fe], possibly attributed to inefficient mixing of AGB star ejecta (Emerick et al., 2018). Observations have also found intrinsic scatter in [Ba/Fe] abundances. Hill et al. (2019) found scatter in the [Ba/Fe] trend, but only at low metallicities ([Fe/H] $\lesssim$

-1.8). Ji et al. (in prep) found roughly 0.2 ± 0.1 dex of scatter in [Ba/Fe] measurements of Reticulum II, which they attributed to inhomogeneous metal mixing. Finally, we measure an upper limit of 0.18 dex scatter in [Ba/Fe] (performed as discussed in Section 4.3 in Escala et al. 2018) for the 108 stars in Sculptor with [Ba/Fe] between -1.5 and $+0.5$ dex. This abundance cut was used to prevent possible barium stars from inflating the intrinsic scatter measured.

In conclusion, there may be ~ 0.2 dex of scatter caused by inefficient mixing in [Ba/Fe] abundances. This is relatively small (comparable to our error bars), and it is not expected that this level of mixing would alter the chemical trend substantially.

- Bursty Star Formation: The GCE model approximates the gas flows as smooth functions. Because the SFR (Equation 4.2) is a simple function of gas mass, the SFR is also a smooth function. In other words, our model does not allow for discrete bursts of star formation, which can occur in dwarf galaxies (Carina, Smecker-Hane et al., 1994; de Boer et al., 2014). In simulations (e.g., El-Badry et al., 2016; Torrey et al., 2017; Orr, Hayward, and Hopkins, 2019), there can be large oscillations in the SFR, especially in the early evolution of galaxies. Significant gaps in star formation could allow the gas to enrich more rapidly between bursts of CCSNe. Our model should only be used for simple galaxies, like Sculptor, that can be approximated by a smooth SFH. The model will not do well with galaxies with more complex SFHs, like Fornax.

  Another way in which our treatment of SFH could affect our results is the treatment of gas flows and gas recycling. The gas outflows in our model permanently escape the galaxy, and the gas inflows contain metal-free, primordial gas. Our model does not account for outflows that are ejected, cool, and that re-accrete onto the galaxy.

- Galaxy Mergers: Our model assumes the entire stellar population observed is formed from either initial or accreted gas, thus does not account for any effects from galaxy mergers. Unlike Milky Way-type galaxies, major mergers are not expected in dwarf galaxies at the times these galaxies are forming stars (Wetzel, Deason, and Garrison-Kimmel, 2015).

- IMF: We test a few different IMFs (Kroupa, Tout, and Gilmore, 1993; Chabrier, 2003; Salpeter, 1955) to see if the IMF impact our results. We

find that changing the IMF alters the model barium trend by less than 0.2 dex (which is comparable to our error bars). Therefore, we do not believe this is an influential choice.

- SNe Ia DTD: The DTD of SNe Ia is highly uncertain due to limited observational evidence (Maoz, Sharon, and Gal-Yam, 2010; Maoz and Graur, 2017), and the time SNe Ia start to explode impacts the model results (Kirby et al., 2011). To include the best possible description of this important assumption, we recommend updating the SNe Ia DTD to a form based on the best available observational data (Section 4.5).

- Stellar Feedback: The model assumes that all gas outflows (Equation 4.4) are a result of supernova feedback. It further assumes that both CCSNe and SNe Ia eject the same amount of gas per supernova. This is a fair assumption because the energy released is roughly the same for both types of supernova. There is uncertainty in how well the supernova's energy is transferred to the gas, a process that depends on the gas density and opacity. To account for the differences in gas properties, A_{out} (the amount of gas ejected per supernova) is allowed to vary from galaxy-to-galaxy.

- SFH: The SFHs currently used in this model are from Kirby et al. (2011). As discussed in that paper, the SFHs returned from the MCMC fitting of [α/Fe] trends are inaccurate for some of the dwarf galaxies, especially Fornax. The impact of the SFH can be seen in Figures 4.6 and 4.12. Potential ways to improve the accuracy of the SFHs are listed in Section 4.5.

- Chemical Retention: Our model assumes that the gas ejected by stellar feedback has a well-mixed composition. It turns out that this is a poor assumption (Emerick et al., 2018). Altering the composition of ejected gas from galactic winds to account for the enrichment source is listed as a potential improvement in Section 4.5.

- Dust: We do not account for dust formation removing barium abundances from the gas in the galaxy. If a substantial amount of barium is trapped in dust, this would effectively be an additional "outflow" in our model. However, dust is not expected to form in significant quantities at the metallicities of most the stars in the dwarf galaxies (Weingartner and Draine, 2001).

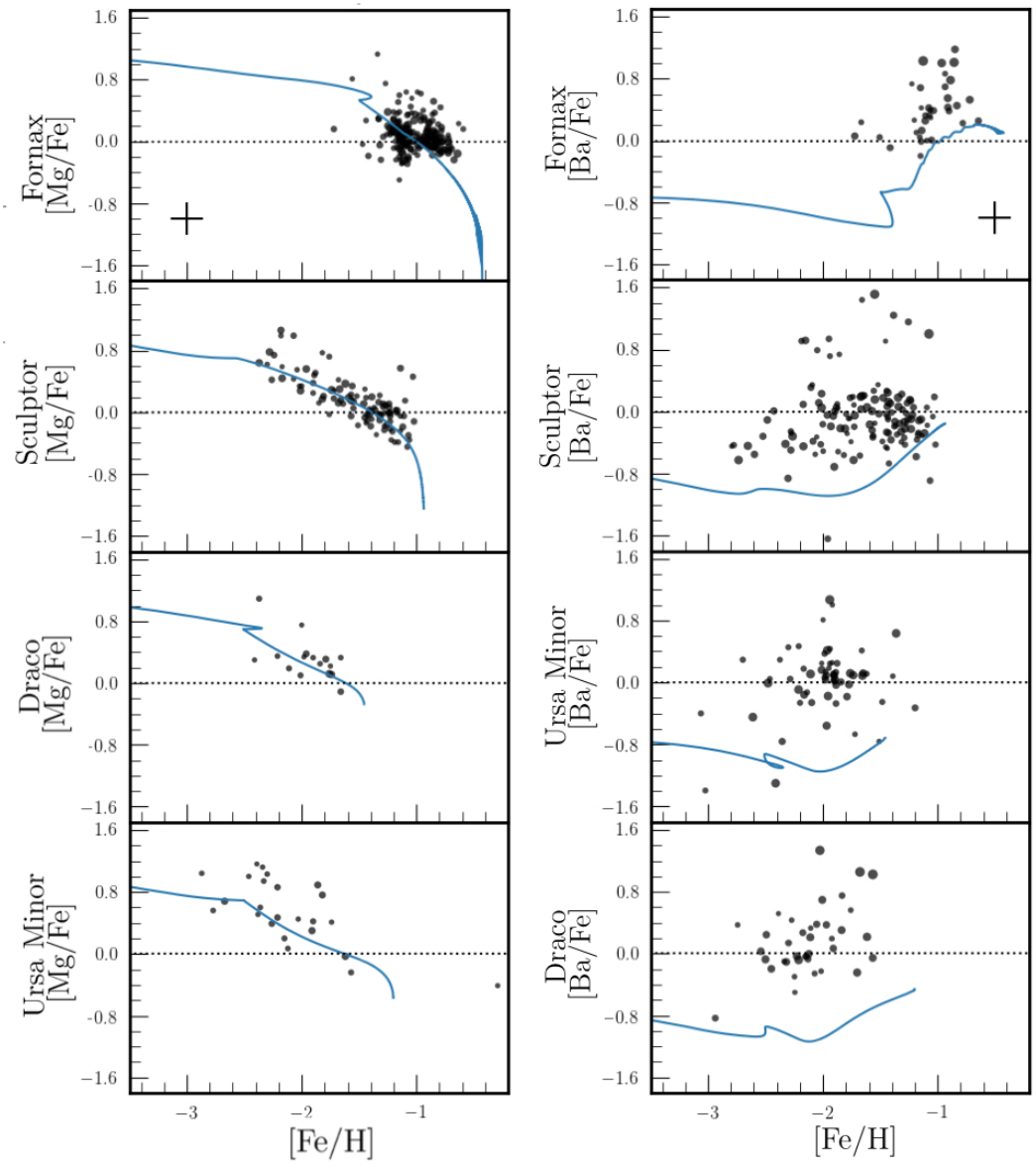

Figure 4.5: Trends of different abundance ratios as a function of metallicity in four different dwarf galaxies. Chapter 2 describes the abundance measurements (black dots). The size of the dot is inversely proportional to the error, so more reliable measurements appear larger. Our GCE models with the default parameters for each galaxy are shown as blue lines. This default model matches [Mg/Fe] trends, but underproduces [Ba/Fe] by more than 0.5 dex in every dwarf galaxy observed.

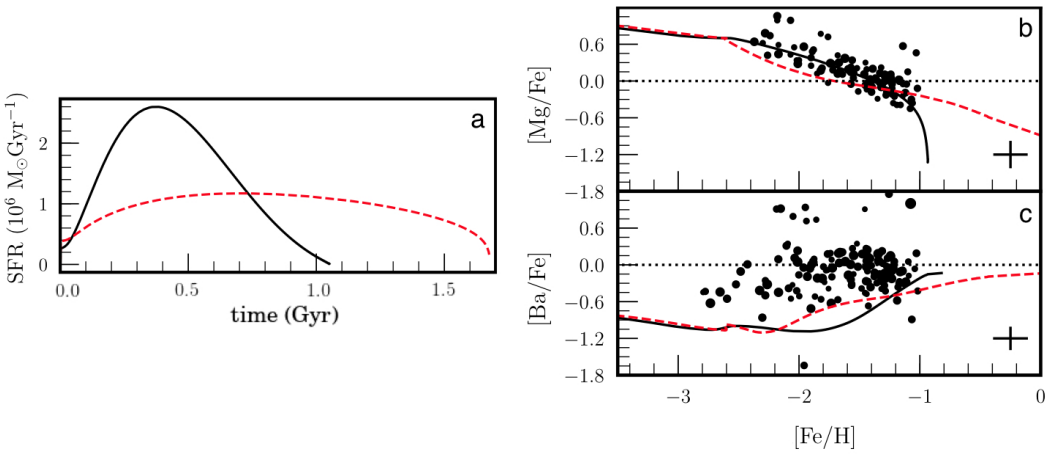

Figure 4.6: GCE models of Sculptor with two different SFHs. Changing the galaxy's star formation duration from 1 to 1.7 Gyrs (see two SFHs in panel a) alters the [Mg/Fe] and [Ba/Fe] abundances in the GCE model (panels b and c). Our abundance measurements (black dots) match the default model (solid line) for [Mg/Fe], but are offset for [Ba/Fe]. This large offset between the models and the measured barium abundances is evidence that altering the SFH within reasonable limits is unable to reconcile this disagreement.

We use this GCE model to test which *r*-process enrichment sources are essential to match the observed abundances. I do not recommend using the values of the free parameters to learn about general galaxy properties (e.g., feedback, dynamics, or star formation).

4.3 Results

We ran this model with the default galaxy parameters (from Kirby et al. 2011) and barium yields from AGB stars (Karakas and Lugaro, 2016; Fishlock et al., 2014) and CCSNe (H. Li et al., 2014). We find that, although this model matched [α/Fe] vs. [Fe/H] trends, it does not match [Ba/Fe] vs. [Fe/H] trends (Figure 4.5). The GCE model with these inputs underpredicts [Ba/Fe] by more than 0.5 dex for all four dwarf galaxies in our sample. We will discuss several alterations to the model—none of which yield a good match to the observed abundances of Ba—before we consider NSMs with the hope of creating models that simultaneously match [α/Fe] and [Ba/Fe] observations in all four dwarf galaxies.

First, we consider the impact of our assumed SFHs. In Figure 4.6, we consider two different SFHs and see the impact on the abundances predicted for Sculptor. The SFHs of these dwarf galaxies are observationally constrained by isochrone fitting to HST color–magnitude diagrams (e.g., Weisz, Zucker, et al., 2012). Within these

constraints, a significant change in Sculptor's SFH (increasing the duration of star formation from 1 to 1.7 Gyrs) alters the modeled [Ba/Fe] and [Mg/Fe] by $\lesssim 0.3$ dex. Therefore, the 0.5 dex difference in [Ba/Fe] is too large to be corrected by reasonable SFH changes alone; something else needs to be considered.

To correct for the discrepancy between the model and the observed range of abundances, we try systematically increasing the barium yield from AGB stars. Two of the most commonly used sets of AGB yields agree within a factor of 2 or 3 (Karakas and Lugaro, 2016; Fishlock et al., 2014; Cristallo et al., 2015). Therefore, we arbitrarily multiply the Karakas and Cristallo yield sets by factors of 2 and 3 to approximate a reasonable range of uncertainty in the yield predictions. Figure 4.6 shows the results of this exercise. The Karakas yields scaled up by a factor of 3 are almost able to match Fornax's [Ba/Fe] trend. However, all the models with increased AGB yields still show large discrepancies when compared to the [Ba/Fe] measurements in the other three galaxies (Figure 4.7).

Because no reasonable choice of barium yields from AGB stars can explain the observations, we turn to SN II yields of barium. Figure 4.8 shows the models resulting from arbitrarily increased SN II barium yields. Given that several rare CCSNe (e.g., MRSNe) have been proposed as sites of the r-process, these could be modeled as dramatically increasing the yield from a typical SNe II. The highest barium yield in Figure 4.8 (3×10^{-7} $M_\odot$) is roughly the yield expected from a rare CCSNe averaged out to a low-level yield per typical CCSNe (as implemented in van de Voort et al., 2019). A large contribution of barium from SNe II causes the model to have a negative slope at early times for the same reason that [Mg/Fe] has a negative slope, i.e., the short timescale of CCSNe and the increasing iron output from SNe Ia. As explained in Chapter 3, the positive [Ba/Fe] slope observed in several dwarf galaxies rules out CCSNe producing the majority of r-process enrichment.

AGB stars and CCSNe alone do not create models that match our observations. We also tested the combination of increasing both types of barium yield simultaneously. Increasing barium production from AGB stars and SNe II results in a very strong dip in [Ba/Fe] at moderate values of [Fe/H] ([Fe/H] ~ -2) in the model because (1) SNe II stop exploding and (2) AGB stars are starting to contribute—all while SNe Ia are ejecting large amounts of iron. However, this dip is not seen in the observations (Figure 4.8). Increasing the modeled barium contribution from AGB stars and/or SNe II is unable to reproduce the [Ba/Fe] values and trends observed.

Therefore, an additional source of barium needs to be included. This source must

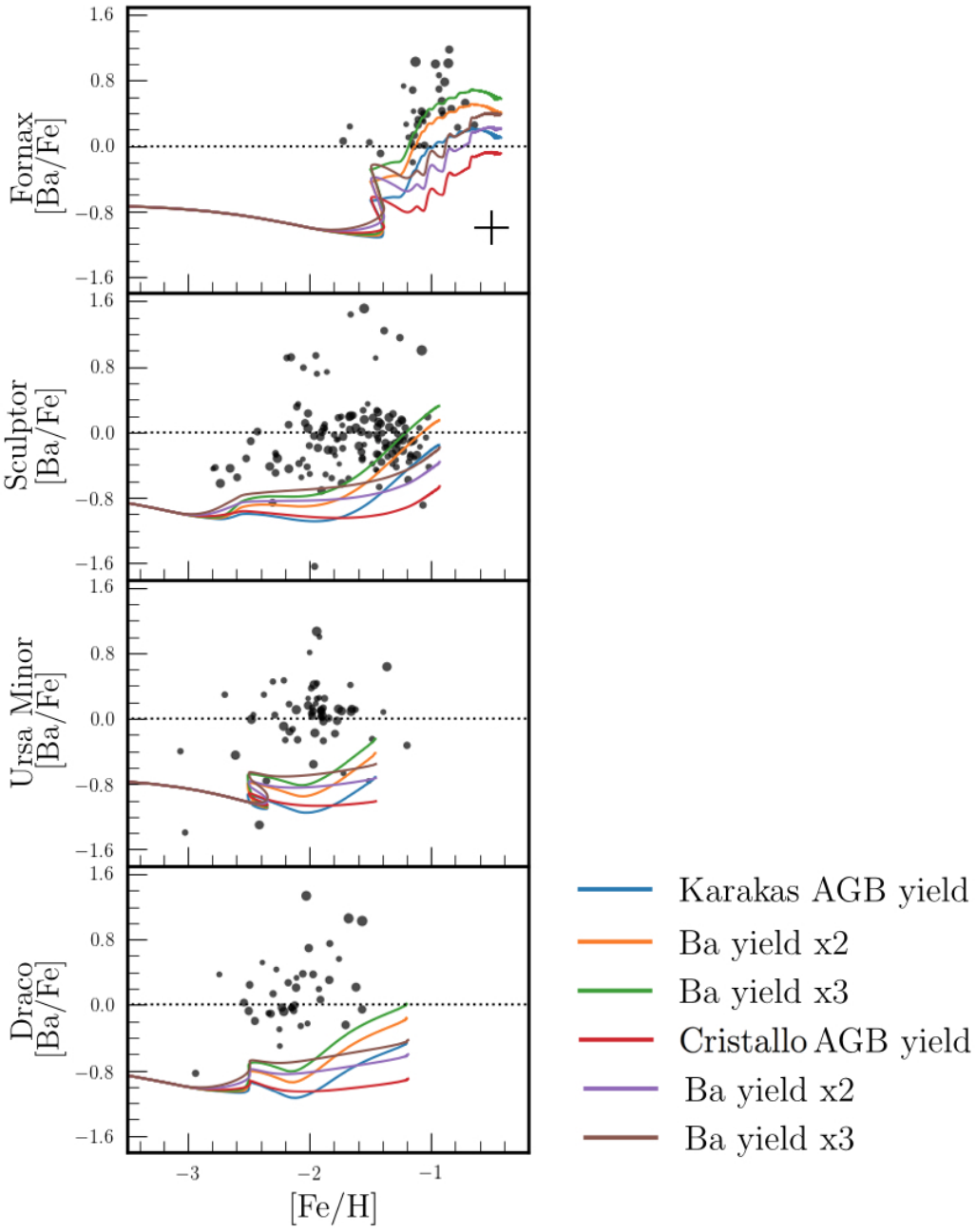

Figure 4.7: GCE model results for two different sets of AGB model yields: Karakas AGB yield (Karakas and Lugaro, 2016; Fishlock et al., 2014), and Cristallo AGB yield (Cristallo et al., 2015). The lowest metallicity AGB model ($Z = 0.001$) has a peak barium yield of $\sim 10^{-7}$ $M_{\odot}$ per AGB star for the Karakas and Cristallo models. Increasing the barium yield of these AGB models is unable to match the abundances observed (black dots) for all galaxies simultaneously.

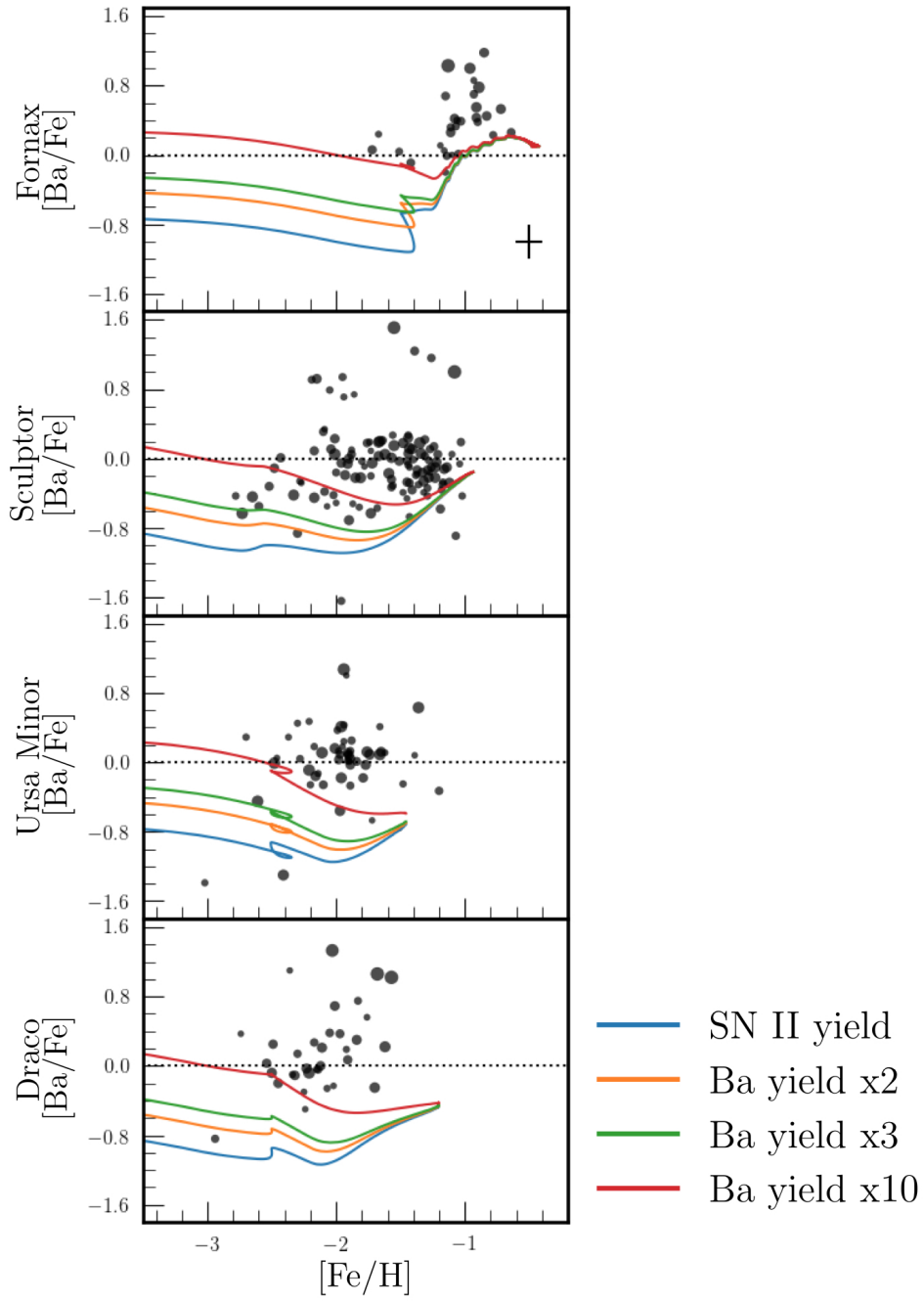

Figure 4.8: GCE models with increasing levels of barium from SNe II. The base SN II barium yield is $\sim 3 \times 10^{-8}$ $M_{\odot}$ per SN II. Increases in the contribution from massive stars (for example to simulate strong *r*-process contribution from MRSNe) generates [Ba/Fe] vs. [Fe/H] trends that do not match the observations (black dots).

have a delay time comparable to the delay time of iron in order to explain the rising trend of [Ba/Fe] vs. [Fe/H]. The most promising source with such a long delay time is NSMs.

In order to incorporate NSMs, a seventh free parameter, $\dot{\xi}_{\rm NSM}$, is added to the GCE model to fit the barium yield from NSMs:

$$\dot{\xi}_{\rm yield} = \dot{\xi}_{\rm AGB} + \dot{\xi}_{\rm SNII} + \dot{\xi}_{\rm SNIa} + \dot{\xi}_{\rm NSM} \tag{4.7}$$

The NSM DTD is still uncertain, so we approximate the DTD for NSMs to have the same shape as the DTD for SNe Ia. Simulations either model the NSM DTD as proportional to t^0 (constant), $t^{-0.5}$, t^{-1} or $t^{-1.5}$ (e.g., Shen et al., 2015; van de Voort et al., 2019; Benoit Côté, Eichler, et al., 2019). Our SNe Ia DTD is proportional to $t^{-1.1}$, i.e., within the currently considered values. Theoretically, the DTD of NSMs is expected to have a similar shape as double-degenerate SNe Ia ($\propto t^{-1}$) because the delay time in both cases is dominated by the time for the binary stars to merge. Observationally, the DTD of NSMs is constrained by the observed rate of sGRB ($\propto t^{-0.8^{+0.25}_{-0.24}}$, Wanderman and Piran 2015). In the future, we plan on testing the impact of varying the NSM DTD.

Figure 4.9 includes barium ejecta from NSMs. We are finally able to create a single set of yield models that closely matches the observations of all four galaxies simultaneously. The barium yield has been tuned until the line plotted approximately matches the observed barium abundances. The corresponding barium yield from NSMs is 1.4×10^{-5} $M_\odot$ per SN Ia.

To conclude, adding NSMs enabled our GCE model to match both the high [Ba/Fe] values and [Ba/Fe] vs. [Fe/H] trends seen in the observed abundances (Figure 4.9).

4.4 Conclusion: Important Constraints on Neutron Star Mergers

Now we have finally found a model that simultaneously overlaps with the abundance trends of all four dwarf galaxies. What can we learn from this model? First, NSMs are the most significant source of barium in dwarf galaxies, especially at low metallicities. As the previous section described, augmentations to the SFH, AGB yield, and CCSN yield are unable to reproduce the observed abundances.

Second, in all cases except for Fornax, the contribution of barium is dominated by NSMs. This can be seen in Figure 4.10, which separates out the contributions of AGB stars, CCSNe, and NSMs. Intuitively it makes sense that Fornax has a larger

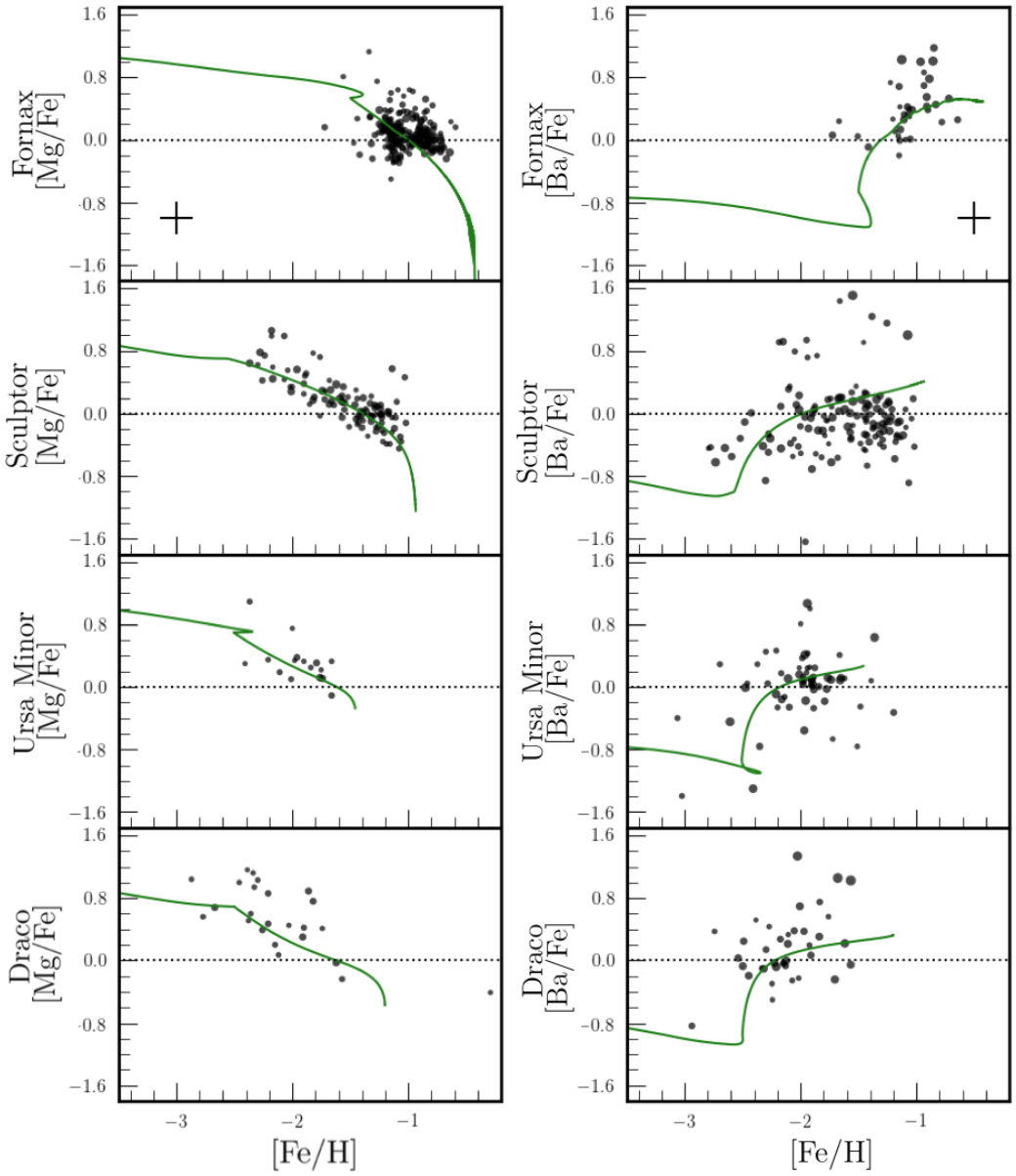

Figure 4.9: A single GCE model with barium coming from AGB stars, CCSNe, and NSMs. The NSM yield included is 1.4×10^{-5} $M_{\odot}$ per SN Ia. This model is able to match [Ba/Fe] trends for all four dwarf galaxies simultaneously.

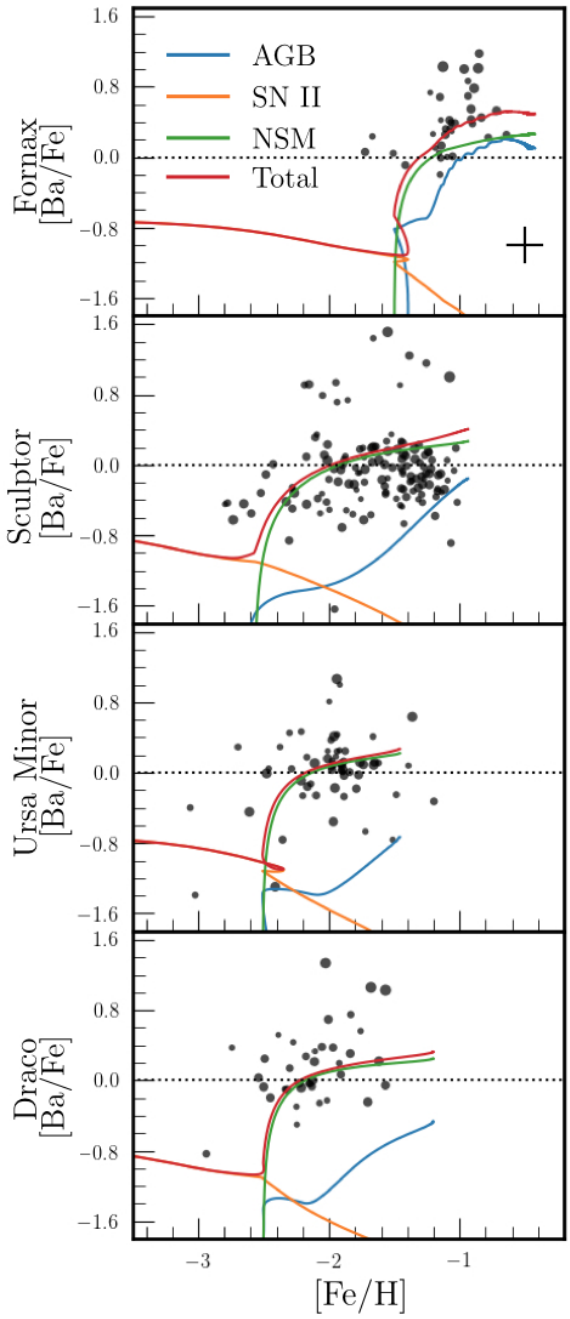

Figure 4.10: [Ba/Fe] predicted by our GCE model with contributions of three sources of barium—AGB stars (Fishlock et al., 2014; Karakas and Lugaro, 2016), SNe II (H. Li et al., 2014), and NSMs ($1.4 \times 10^{-5}\,M_{\odot}$ per SN Ia). NSMs are the dominant source of barium for Sculptor, Ursa Minor, and Draco.

contribution from AGB stars, because it has a longer period of star formation than any of the other galaxies. Fornax was forming stars for long enough for AGB stars to be an important source of barium at higher metallicites.

Third, we can employ a back-of-the-envelope calculation to see if the yield of barium from NSM is reasonable (Figure 4.9). The barium yield from NSMs is modeled as incremental amounts of barium released with each SN Ia ($\zeta_{\rm Ba,SNIa}$)[1]. To obtain a NSM rate ($\dot{N}_{\rm NSM}$, Equation 4.8) that we can easily compare with other predictions, we multiply the SN Ia rate ($\dot{N}_{\rm Ia}$, W. Li et al. 2011) by the barium production rate ($\zeta_{\rm Ba,SNIa}$, Figure 4.9) and divide by the NSM barium yield ($\zeta_{\rm Ba,NSM}$, Tanvir et al. 2017; Tanaka et al. 2017; Chornock et al. 2017; Kilpatrick et al. 2017; Benoit Côté, Fryer, et al. 2018). Our rate (Equation 4.8) overlaps with the upper half of the LIGO NSM rate ($\dot{N}_{\rm NSM,LIGO} = 320 - 4{,}740\,{\rm Gpc^{-3}\,yr^{-1}}$, Abbott et al. 2017) and is much higher than the upperlimit calculated from not finding kilonovae in PTF ($\dot{N}_{\rm NSM,PTF} \lesssim 800\,{\rm Gpc^{-3}\,yr^{-1}}$, Kasliwal et al. 2017).

$$\dot{N}_{\rm NSM} = \frac{\dot{N}_{\rm Ia} \times \zeta_{\rm Ba,SNIa}}{\zeta_{\rm Ba,NSM}} = \frac{(2.7\times10^{4})\times(1.4\times10^{-5})}{(3-15)\times10^{-5}}\,{\rm NSM\,Gpc^{-3}\,yr^{-1}} \approx 2{,}520 - 12{,}600\,{\rm NSM\,Gpc^{-3}\,yr^{-1}} \quad (4.8)$$

Finally, to see what this model says about NSMs in a given dwarf galaxy (Sculptor in this case) we estimate the total number of NSMs in the galaxy's history. The product of the total number of SNe Ia ($N_{\rm Ia}$, Equation 4.9) and the barium production rate by NSM (per SNe Ia, $\zeta_{\rm Ba,SNIa}$, Figure 4.9) returns the total gas mass of barium contributed by NSMs to the galaxy ($\xi_{\rm Ba,NSM}$, Equation 4.10). Note that this is the total gas mass of barium that needs to be ejected from NSMs during Sculptor's star forming years, but some fraction of this barium was ejected out of the galaxy. Dividing the total barium mass by the NSM yield predicted by models ($\zeta_{\rm Ba,NSM}$) returns the number of NSMs that occurred in each dwarf galaxy ($N_{\rm NSM}$, Equation 4.11). For a galaxy like Sculptor, there are enough NSMs that averaging out their contribution is acceptable.

$$N_{\rm Ia} = M_{*}\times\tau_{\rm SF}\times\int_{0}^{\tau_{\rm SF}}\Psi_{\rm Ia}dt = (1.3\times10^{6})\times(0.9)\times(2.48)\,{\rm SNIa} \approx 2{,}800\,{\rm SNe\ Ia} \quad (4.9)$$

[1]To be explicit, we are not claiming that SNe Ia produce barium. We are modeling the NSM yield as a low-level contribution per SNe Ia for convenience.

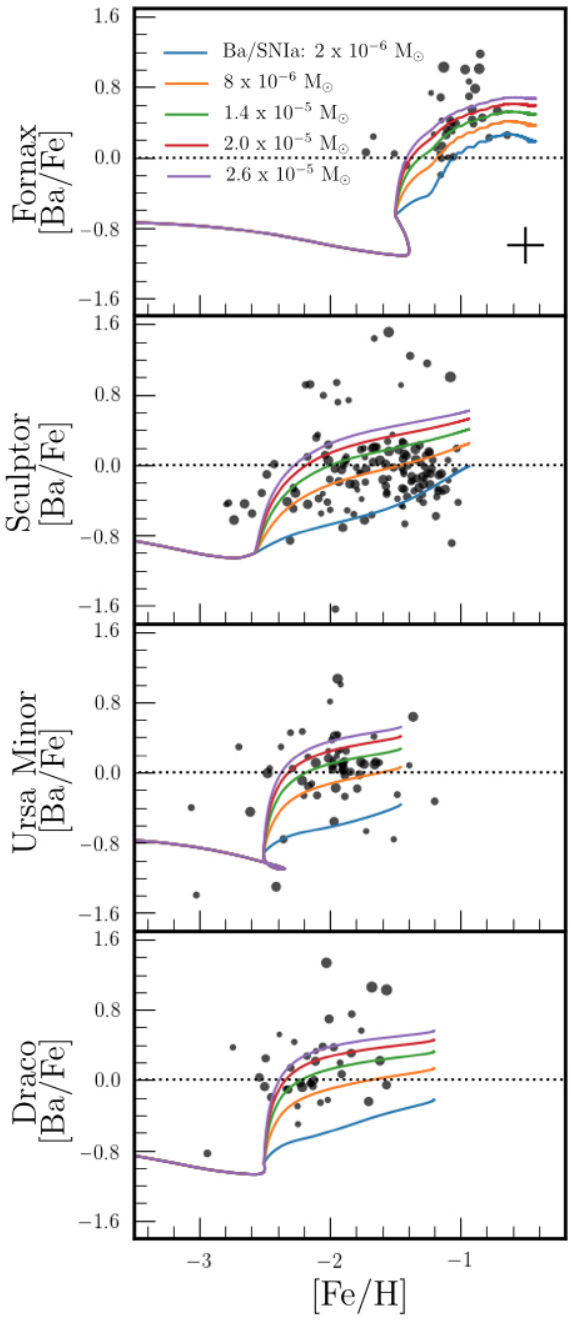

Figure 4.11: GCE models with various levels of barium contributed by NSMs. NSM barium contribution is modeled by a continual low-level barium yield ejected with each SN Ia ($\zeta_{\mathrm{Ba,SNIa}}$). Multiplying this value by the total number of SNe Ia in a given galaxy results in the total mass of barium contributed by NSMs. These models both achieve the [Ba/Fe] values and match the [Ba/Fe] vs. [Fe/H] trends observed (black dots). MCMC fitting will simultaneously find the optimum barium yield along with the variables describing galaxy properties.

$$\xi_{\mathrm{Ba,NSM}} = N_{\mathrm{Ia}} \times \zeta_{\mathrm{Ba,SNIa}} = 2800\,\mathrm{SNIa} \times (1.4 \times 10^{-5}\,\mathrm{M_\odot\,SNIa^{-1}}) \approx 0.04\,\mathrm{M_\odot} \quad (4.10)$$

$$N_{\mathrm{NSM}} = \frac{\xi_{\mathrm{Ba,NSM}}}{\zeta_{\mathrm{Ba,NSM}}} = \frac{0.04\,\mathrm{M_\odot}}{(3-15) \times 10^{-5}\,\mathrm{M_\odot\,NSM^{-1}}} \approx 270 \text{ to } 1{,}300\,\mathrm{NSMs} \quad (4.11)$$

To review, this model has lead us to several preliminary conclusions. (1) AGB stars and CCSNe alone are unable to recreate the [Ba/Fe] abundance trends observed. (2) In all three dwarf galaxies with short SFHs, NSMs are the dominant source of barium production at all times. (3) The barium yield from NSMs needed to match our observations is consistent with the current range of LIGO's predicted NSM yields and rates ($\dot{N}_{\mathrm{NSM,LIGO}}$), but is too high according to PTF's upperlimit ($\dot{N}_{\mathrm{NSM,PTF}}$). (4) The barium contribution from NSMs corresponds to 270 to 1,300 NSMs occurring in Sculptor while Sculptor was forming stars.

4.5 Next Steps

This line of research is very promising, but some next steps need to be completed before this work is ready for publication. The path forward is to improve current assumptions and better constrain the NSM yields/rates. Below I have outlined the next steps of this project.

- MCMC fitting: MCMC analysis (e.g., B. Côté et al., 2017) will match the GCE model to our observations to simultaneously fit the six free parameters and the NSM barium yield. How the models change with varying NSM yields is shown in Figure 4.11. The NSM yield can be related to the total mass of barium contributed by NSMs per dwarf galaxy (Equation 4.10). However, the GCE model needs to be made more computationally efficient before MCMC analysis is possible.

- Improve Efficiency: Although I have highlighted how time-efficient our GCE model is compared to hydrodynamic simulations, it currently takes tens of seconds to run. For MCMC fitting, the model would ideally take less than a second. By evaluating how the model spends its time, I have identified two key improvements. (1) Instead of calculating the ejecta from each source at each timestep, the model should forward-predict the chemical ejecta as the stars are made. This would replace expensive integrals with trivial array addition. (2) Remove interpolation of chemical yield grids from occurring at each timestep. Instead, create a fine grid of chemical yields at the beginning of the model.

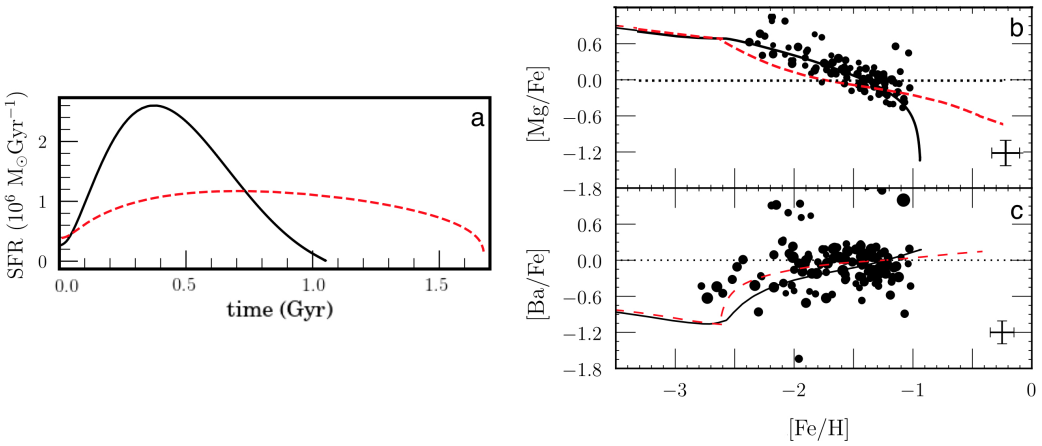

Figure 4.12: GCE models with NSM yields for two different SFHs. Changing the galaxy's star formation duration from 1 to 1.7 Gyrs (see two SFHs in panel a) alters the [Ba/Fe] abundances by $\sim$ 0.3 dex in the GCE model (panel c). Compare this figure to Figure 4.6, which does not include contribution by NSMs. The NSM contribution in this plot is 0.6×10^{-5} $M_\odot$ per SN Ia. This is a slightly lower yield than presented in Figure 4.9.

- SFH: We need to restructure the model to allow the SFH to be an input (e.g., Weisz, Dolphin, et al., 2014) and have gas inflow history be an output. Figure 4.12 shows the impact of the SFH when NSM ejecta are included. By including the most accurate SFHs, our conclusions will be more robust.

- Chemical Retention: We need to alter the composition of gas ejected from the galaxy to account for each source of enrichment. Emerick et al. (2018) found that 20% of AGB ejecta are retained by the galaxy, while only 5% of SN ejecta are retained.

- Update Yields: We should incorporate newly published yields (e.g., Karakas, Lugaro, et al., 2018), and we should also explicitly include *s*-process yields from rotating, high-mass stars (e.g., Cescutti et al., 2015; Frischknecht et al., 2016).

- NSM DTD: We are currently approximating the DTD for NSMs by substituting the DTD for SNe Ia ($\propto t^{-1.1}$, t_{min} = 100 Myr). We should instead try functional forms specifically proposed for NSMs, including t^0, t^{-1} and $t^{-1.5}$ with t_{min} = 1, 10, and 100 Myr.

- SNe Ia DTD: Update the SNe Ia DTD to the more recent description in Maoz and Graur (2017).

- *s*- vs. *r*-process Contribution: This would be a great oppurtunity to check what our GCE model can say about the *s*-process subtraction published in Chapter 3 (see Hirai, Wanajo, and Saitoh 2019). (1) We can predict [Ba/Eu] trends from the GCE model and compare to the observations (Figure 3.2). (2) We can compare the predicted *r*/*s*-process percentage from [Ba/Eu] (Equation 3.1) and from the model directly. To do these checks, we need to add europium to the model and track barium coming from the *r*- and *s*-processes.

To conclude, we have confirmed that NSMs are the most likely physical origin of the *r*-process in dwarf galaxies using the largest catalog of barium abundances of dwarf galaxies and new models of GCE. Future work will use these models to provide observational constraints to NSM models and predict for the first time the number of NSMs that have occurred in these different dwarf galaxies.

References

Abbott, B. P. et al. (2017). "GW170817: Observation of Gravitational Waves from a Binary Neutron Star Inspiral". In: *Physical Review Letters* 119.16, 161101, p. 161101. DOI: 10.1103/PhysRevLett.119.161101. arXiv: 1710.05832 [gr-qc].

El-Badry, K. et al. (2016). "Breathing FIRE: How Stellar Feedback Drives Radial Migration, Rapid Size Fluctuations, and Population Gradients in Low-mass Galaxies". In: *ApJ* 820, 131, p. 131. DOI: 10.3847/0004-637X/820/2/131. arXiv: 1512.01235.

Cescutti, G. et al. (2015). "The role of neutron star mergers in the chemical evolution of the Galactic halo". In: *A&A* 577, A139, A139. DOI: 10.1051/0004-6361/201525698. arXiv: 1503.02954 [astro-ph.GA].

Chabrier, G. (2003). "Galactic Stellar and Substellar Initial Mass Function". In: *PASP* 115, pp. 763–795. DOI: 10.1086/376392. eprint: astro-ph/0304382.

Chornock, R. et al. (2017). "The Electromagnetic Counterpart of the Binary Neutron Star Merger LIGO/Virgo GW170817. IV. Detection of Near-infrared Signatures of r-process Nucleosynthesis with Gemini-South". In: *ApJL* 848.2, L19, p. L19. DOI: 10.3847/2041-8213/aa905c. arXiv: 1710.05454 [astro-ph.HE].

Côté, Benoit, Marius Eichler, et al. (2019). "Neutron Star Mergers Might Not Be the Only Source of r-process Elements in the Milky Way". In: *ApJ* 875.2, 106, p. 106. DOI: 10.3847/1538-4357/ab10db. arXiv: 1809.03525 [astro-ph.HE].

Côté, Benoit, Chris L. Fryer, et al. (2018). "The Origin of r-process Elements in the Milky Way". In: *ApJ* 855.2, 99, p. 99. DOI: 10.3847/1538-4357/aaad67. arXiv: 1710.05875 [astro-ph.GA].

Côté, B. et al. (2017). "The Impact of Modeling Assumptions in Galactic Chemical Evolution Models". In: *ApJ* 835, 128, p. 128. DOI: 10.3847/1538-4357/835/2/128. arXiv: 1604.07824.

Cristallo, S. et al. (2015). "Evolution, Nucleosynthesis, and Yields of AGB Stars at Different Metallicities. III. Intermediate-mass Models, Revised Low-mass Models, and the ph-FRUITY Interface". In: *ApJS* 219, 40, p. 40. DOI: 10.1088/0067-0049/219/2/40. arXiv: 1507.07338 [astro-ph.SR].

de Boer, T. J. L. et al. (2014). "The episodic star formation history of the Carina dwarf spheroidal galaxy". In: *A&A* 572, A10, A10. DOI: 10.1051/0004-6361/201424119. arXiv: 1409.3229 [astro-ph.GA].

Emerick, A. et al. (2018). "Metal Mixing and Ejection in Dwarf Galaxies Are Dependent on Nucleosynthetic Source". In: *ApJ* 869, 94, p. 94. DOI: 10.3847/1538-4357/aaec7d. arXiv: 1809.01167.

Escala, I. et al. (2018). "Modelling chemical abundance distributions for dwarf galaxies in the Local Group: the impact of turbulent metal diffusion". In: *MNRAS* 474, pp. 2194–2211. DOI: 10.1093/mnras/stx2858. arXiv: 1710.06533.

Fishlock, C. K. et al. (2014). "Evolution and Nucleosynthesis of Asymptotic Giant Branch Stellar Models of Low Metallicity". In: *ApJ* 797, 44, p. 44. DOI: 10.1088/0004-637X/797/1/44. arXiv: 1410.7457 [astro-ph.SR].

Frischknecht, U. et al. (2016). "s-process production in rotating massive stars at solar and low metallicities". In: *MNRAS* 456, pp. 1803–1825. DOI: 10.1093/mnras/stv2723. arXiv: 1511.05730 [astro-ph.SR].

Hill, V. et al. (2019). "VLT/FLAMES high-resolution chemical abundances in Sculptor: a textbook dwarf spheroidal galaxy". In: *A&A* 626, A15, A15. DOI: 10.1051/0004-6361/201833950. arXiv: 1812.01486 [astro-ph.GA].

Hirai, Yutaka, Shinya Wanajo, and Takayuki R. Saitoh (2019). "Enrichment of Strontium in Dwarf Galaxies". In: *arXiv e-prints*, arXiv:1909.09163, arXiv:1909.09163. arXiv: 1909.09163 [astro-ph.GA].

Hotokezaka, Kenta, Paz Beniamini, and Tsvi Piran (2018). "Neutron star mergers as sites of r-process nucleosynthesis and short gamma-ray bursts". In: *International Journal of Modern Physics D* 27.13, 1842005, p. 1842005. DOI: 10.1142/S0218271818420051. arXiv: 1801.01141 [astro-ph.HE].

Iwamoto, K. et al. (1999). "Nucleosynthesis in Chandrasekhar Mass Models for Type IA Supernovae and Constraints on Progenitor Systems and Burning-Front Propagation". In: *ApJS* 125, pp. 439–462. DOI: 10.1086/313278. eprint: astro-ph/0002337.

Karakas, A. I. and M. Lugaro (2016). "Stellar Yields from Metal-rich Asymptotic Giant Branch Models". In: *ApJ* 825, 26, p. 26. DOI: 10.3847/0004-637X/825/1/26. arXiv: 1604.02178 [astro-ph.SR].

Karakas, A. I., M. Lugaro, et al. (2018). "Heavy-element yields and abundances of asymptotic giant branch models with a Small Magellanic Cloud metallicity". In: *MNRAS* 477, pp. 421–437. DOI: 10.1093/mnras/sty625. arXiv: 1803.02028 [astro-ph.SR].

Kasliwal, M. M. et al. (2017). "Illuminating gravitational waves: A concordant picture of photons from a neutron star merger". In: *Science* 358.6370, pp. 1559–1565. DOI: 10.1126/science.aap9455. arXiv: 1710.05436 [astro-ph.HE].

Kilpatrick, C. D. et al. (2017). "Electromagnetic evidence that SSS17a is the result of a binary neutron star merger". In: *Science* 358.6370, pp. 1583–1587. DOI: 10.1126/science.aaq0073. arXiv: 1710.05434 [astro-ph.HE].

Kirby, E. N. et al. (2011). "Multi-element Abundance Measurements from Medium-resolution Spectra. IV. Alpha Element Distributions in Milky Way Satellite Galaxies". In: *ApJ* 727, 79, p. 79. DOI: 10.1088/0004-637X/727/2/79. arXiv: 1011.5221 [astro-ph.GA].

Kodama, T. (1997). PhD thesis. PhD thesis, Institute of Astronomy, Univ. Tokyo , (1997).

Kroupa, P., C. A. Tout, and G. Gilmore (1993). "The distribution of low-mass stars in the Galactic disc". In: *MNRAS* 262, pp. 545–587. DOI: 10.1093/mnras/262.3.545.

Li, H. et al. (2014). "Estimating R-Process Yields from Abundances of the Metal-Poor Stars". In: *PASP* 126, pp. 544–552. DOI: 10.1086/677201. arXiv: 1407.4878 [astro-ph.SR].

Li, Weidong et al. (2011). "Nearby supernova rates from the Lick Observatory Supernova Search - III. The rate-size relation, and the rates as a function of galaxy Hubble type and colour". In: *MNRAS* 412.3, pp. 1473–1507. DOI: 10.1111/j.1365-2966.2011.18162.x. arXiv: 1006.4613 [astro-ph.SR].

Maoz, D. and O. Graur (2017). "Star Formation, Supernovae, Iron, and α: Consistent Cosmic and Galactic Histories". In: *ApJ* 848, 25, p. 25. DOI: 10.3847/1538-4357/aa8b6e. arXiv: 1703.04540 [astro-ph.HE].

Maoz, D., K. Sharon, and A. Gal-Yam (2010). "The Supernova Delay Time Distribution in Galaxy Clusters and Implications for Type-Ia Progenitors and Metal Enrichment". In: *ApJ* 722, pp. 1879–1894. DOI: 10.1088/0004-637X/722/2/1879. arXiv: 1006.3576.

Naiman, Jill P. et al. (2018). "First results from the IllustrisTNG simulations: a tale of two elements - chemical evolution of magnesium and europium". In: *MNRAS* 477.1, pp. 1206–1224. DOI: 10.1093/mnras/sty618. arXiv: 1707.03401 [astro-ph.GA].

Nomoto, K. et al. (2006). "Nucleosynthesis yields of core-collapse supernovae and hypernovae, and galactic chemical evolution". In: *Nuclear Physics A* 777, pp. 424–458. DOI: 10.1016/j.nuclphysa.2006.05.008. eprint: astro-ph/0605725.

Orr, Matthew E., Christopher C. Hayward, and Philip F. Hopkins (2019). "A simple non-equilibrium feedback model for galaxy-scale star formation: delayed feedback and SFR scatter". In: *MNRAS* 486.4, pp. 4724–4737. DOI: 10.1093/mnras/stz1156. arXiv: 1810.09460 [astro-ph.GA].

Padovani, P. and F. Matteucci (1993). "Stellar Mass Loss in Elliptical Galaxies and the Fueling of Active Galactic Nuclei". In: *ApJ* 416, p. 26. DOI: 10.1086/173212.

Revaz, Y. et al. (2016). "Computational issues in chemo-dynamical modelling of the formation and evolution of galaxies". In: *A&A* 588, A21, A21. DOI: 10.1051/0004-6361/201526438. arXiv: 1601.02017.

Safarzadeh, M. and E. Scannapieco (2017). "Simulating neutron star mergers as r-process sources in ultrafaint dwarf galaxies". In: *MNRAS* 471, pp. 2088–2096. DOI: 10.1093/mnras/stx1706. arXiv: 1707.01909.

Salpeter, E. E. (1955). "The Luminosity Function and Stellar Evolution." In: *ApJ* 121, p. 161. DOI: 10.1086/145971.

Schmidt, M. (1959). "The Rate of Star Formation." In: *ApJ* 129, p. 243. DOI: 10.1086/146614.

Shen, Sijing et al. (2015). "The History of R-Process Enrichment in the Milky Way". In: *ApJ* 807.2, 115, p. 115. DOI: 10.1088/0004-637X/807/2/115. arXiv: 1407.3796 [astro-ph.GA].

Smecker-Hane, Tammy A. et al. (1994). "The Stellar Population of the Carina Dwarf Spheroidal Galaxy. I. A New Color- Magnitude Diagram for the Giant and the Horizontal Branches". In: *AJ* 108, p. 507. DOI: 10.1086/117087. arXiv: astro-ph/9404057 [astro-ph].

Tanaka, Masaomi et al. (2017). "Kilonova from post-merger ejecta as an optical and near-Infrared counterpart of GW170817". In: *PASJ* 69.6, 102, p. 102. DOI: 10.1093/pasj/psx121. arXiv: 1710.05850 [astro-ph.HE].

Tanvir, N. R. et al. (2017). "The Emergence of a Lanthanide-rich Kilonova Following the Merger of Two Neutron Stars". In: *ApJL* 848, L27, p. L27. DOI: 10.3847/2041-8213/aa90b6. arXiv: 1710.05455 [astro-ph.HE].

Torrey, Paul et al. (2017). "An instability of feedback-regulated star formation in galactic nuclei". In: *MNRAS* 467.2, pp. 2301–2314. DOI: 10.1093/mnras/stx254. arXiv: 1601.07186 [astro-ph.GA].

van de Voort, Freeke et al. (2019). "Neutron star mergers and rare core-collapse supernovae as sources of r-process enrichment in simulated galaxies". In: *arXiv e-prints*, arXiv:1907.01557, arXiv:1907.01557. arXiv: 1907.01557 [astro-ph.GA].

Wanderman, David and Tsvi Piran (2015). "The rate, luminosity function and time delay of non-Collapsar short GRBs". In: *MNRAS* 448.4, pp. 3026–3037. DOI: 10.1093/mnras/stv123. arXiv: 1405.5878 [astro-ph.HE].

Wechsler, R. H. et al. (2002). "Concentrations of Dark Halos from Their Assembly Histories". In: *ApJ* 568, pp. 52–70. DOI: 10.1086/338765. eprint: astro-ph/0108151.

Weingartner, Joseph C. and B. T. Draine (2001). "Dust Grain-Size Distributions and Extinction in the Milky Way, Large Magellanic Cloud, and Small Magellanic Cloud". In: *ApJ* 548.1, pp. 296–309. DOI: 10.1086/318651. arXiv: astro-ph/0008146 [astro-ph].

Weisz, D. R., A. E. Dolphin, et al. (2014). "The Star Formation Histories of Local Group Dwarf Galaxies. II. Searching For Signatures of Reionization". In: *ApJ* 789, 148, p. 148. DOI: 10.1088/0004-637X/789/2/148. arXiv: 1405.3281.

Weisz, D. R., D. B. Zucker, et al. (2012). "The Star Formation History of Leo T from Hubble Space Telescope Imaging". In: *ApJ* 748, 88, p. 88. DOI: 10.1088/0004-637X/748/2/88. arXiv: 1201.4859.

Wetzel, A. R., A. J. Deason, and S. Garrison-Kimmel (2015). "Satellite Dwarf Galaxies in a Hierarchical Universe: Infall Histories, Group Preprocessing, and Reionization". In: *ApJ* 807, 49, p. 49. DOI: 10.1088/0004-637X/807/1/49. arXiv: 1501.01972.

Wheeler, C. et al. (2015). "Sweating the small stuff: simulating dwarf galaxies, ultra-faint dwarf galaxies, and their own tiny satellites". In: *MNRAS* 453, pp. 1305–1316. DOI: 10.1093/mnras/stv1691. arXiv: 1504.02466.

Chapter 5

THE STARS IN M15 WERE BORN WITH THE *R*-PROCESS

Kirby, E. N., G. E. Duggan, et al. (in prep). "The Stars in M15 Were Born with the *r*-process". In: *Astrophysical Journal, Letters*.

ABSTRACT

High-resolution spectroscopy of stars on the red giant branch (RGB) of the globular cluster M15 has revealed a large ($\sim$ 1 dex) dispersion in the abundances of *r*-process elements, like Ba and Eu. Neutron star mergers (NSMs) have been proposed as a major source of the *r*-process. However, most NSM models predict a delay time longer than the timescale for cluster formation. One possibility is that a NSM polluted the surfaces of stars in M15 long after the cluster finished forming. In this case, the abundances of the polluting elements would decrease in the first dredge-up as stars turn on to the RGB. We present Keck/DEIMOS abundances of Ba along the entire RGB and the top of the main sequence. The Ba abundances have no trend with stellar luminosity (evolutionary phase). Therefore, the stars were born with the Ba they have today, and Ba did not originate in a source with a delay time longer than the timescale for cluster formation.

5.1 Introduction

Elements beyond iron in the periodic table are made primarily via neutron capture, which can happen either slowly (*s*-process) or rapidly (*r*-process). While the *s*-process is known to occur primarily in asymptotic giant branch stars (Truran and Iben, 1977), there are still multiple candidate sites for the *r*-process. The gravitational wave-based discovery and subsequent electromagnetic observation of a kilonova in 2017 definitively showed that the *r*-process does occur in neutron star mergers (NSMs, Chornock et al., 2017; Kasen et al., 2017). However, it is far from clear that NSMs are the sole site of the *r*-process.

The strongest argument that the *r*-process is also created in other events is that NSMs are expected to have long delay times ($\gtrsim 10^8$ yr, Kalogera et al., 2001). For example, it is difficult to explain the early appearance of the *r*-process in the Milky Way (MW)

halo (van Oirschot et al., 2019). In the MW disk, the *r*-process element Eu appears to be created in lockstep with Mg (e.g., Ishigaki, Aoki, and Chiba, 2013), which is nearly instantaneously recycled from core collapse supernovae (CCSNe). Duggan et al. (2018) showed that the *r*-process component of Ba is delayed relative to CCSNe at [Fe/H] < -1.6—but perhaps not at higher metallicities—in the Sculptor dwarf galaxy. However, Skúladóttir et al. (2019) argued that Eu in Sculptor shows no delay relative to Mg, although their data was limited in the metallicity range where Duggan et al. showed that *r*-process Ba is delayed.

There are two possibilities for synthesizing the *r*-process with a short delay. First, it is possible that there is a prompt population of NSMs. For example, the dynamics of dense star clusters can shorten the delay time compared to a NSM formed in the field (Ramirez-Ruiz et al., 2015). Second, there could be another major source of the *r*-process. Although the high-entropy wind surrounding the proto-neutron star of a CCSN was initially thought to be a promising site for *r*-process production (Meyer et al., 1992), most CCSN simulations fail to achieve the conditions required for the *r*-process (e.g., Qian and Woosley, 1996). An alternative is jet-driven, magnetorotational CCSNe. Simulations of such explosions have shown both a robust *r*-process (Nishimura, Takiwaki, and Thielemann, 2015) or the failure to produce an *r*-process without unreasonably high magnetic fields (Mösta et al., 2018). The current state of the field is that observations indicate that some *r*-process material comes from prompt sources, but it is difficult to produce the *r*-process in theoretical simulations of prompt sources.

Globular clusters (GCs) might be able to help show a fuller range of *r*-process production sites. GCs are complex sites of star formation. Almost all GCs show multiple chemical populations (R. Gratton, C. Sneden, and E. Carretta, 2004; Raffaele G. Gratton, Eugenio Carretta, and Angela Bragaglia, 2012), but no theory proposed so far can explain all of the nuances of the observed chemical abundance patterns (Bastian and Lardo, 2018). The multiple populations in GCs are most evident in light elements, like O and Na, but a small number of GCs possibly shows variations in neutron-capture elements (Roederer, 2011). The exemplar (and only incontrovertible example) of this phenomenon is M15, which shows ~ 1 dex scatter in Ba, Eu, and other heavy elements (C. Sneden, Kraft, et al., 1997; C. Sneden, Johnson, et al., 2000; C. Sneden, Pilachowski, and Kraft, 2000; Sobeck et al., 2011; Worley et al., 2013). The neutron-capture abundance pattern in nearly all GCs, including M15, is dominated by the *r*-process (e.g., C. Sneden, Johnson, et al., 2000).

Therefore, some phenomenon must be able to pollute M15 inhomogeneously with the *r*-process. The inhomogeneity arises from a different source from the light elements because there is no correlation between the abundance variations in the light and neutron-capture elements in M15 or any other GC (Roederer, 2011).

In this letter, we investigate the possibility that the *r*-process in M15 was created by a NSM. Specifically, we consider a NSM with a "standard" delay time ($> 10^8$ yr), much longer than the timescale of the formation of the cluster ($\sim 10^7$ yr). In this scenario, the ejecta of the NSM would pollute stars after they formed. This scenario explains the star-to-star scatter in neutron-capture abundances because stars nearest to the NSM would have received the highest degree of pollution. The hypothesis predicts depletion of neutron-capture elements as stars ascend the red giant branch (RGB). We test this prediction with measurements of Ba abundances in M15 from the main sequence to the tip of the RGB.

5.2 Observations and Abundance Measurements

We observed a single slitmask with DEIMOS on the Keck II telescope on 2017 Sep 15. The slitmask, called `7078l1`, was the same as that observed by Kirby et al. (2016). We used *BVRI* photometry from Stetson (1994). We chose targets from the RGB and main sequence turn-off (MSTO). The selection was performed by drawing a polygon around the locus of stars in the color–magnitude diagram (CMD). The width of the polygon was about 0.7 mag in $B - V$ color, which is wide enough to include effectively 100% of candidate member stars.

We used the 1200B grating at a central wavelength of 5500 Å. The approximate spectral range was 3900–4500 Å with a resolution of $\Delta\lambda = 1.1$ Å. We obtained 13 exposures of 20 minutes each for a total exposure time of 4.3 hours. The seeing was 0.6", and the transparency was good. We reduced the spectra with `spec2d` (Cooper et al., 2012; Newman et al., 2013), including our own modifications for the wavelength solution for the 1200B grating (see de los Reyes, Kirby, and Shen, 2019).

Kirby et al. (2016) previously measured radial velocities, effective temperatures ($T_{\rm eff}$) and metallicities ([Fe/H]) for the stars on this slitmask. We used their membership determination, which enforced that members have radial velocities and metallicities within 3 standard deviations of their respective cluster means. We discarded the spectra of known non-members.

We measured Ba abundances using the procedure of Duggan et al. (2018). They

constructed a grid of synthetic spectra over a range of $T_{\rm eff}$, surface gravity ($\log g$), [Fe/H], and Ba abundance. The spectra were computed with MOOG (C. A. Sneden, 1973; Chris Sneden et al., 2012). The grid is searched for the Ba abundance that minimizes χ^2 between the grid and the observed spectrum. The other parameters were fixed at their previously determined values (Kirby et al., 2016). Table 5.1 gives the Ba abundances for all the stars in our sample. Stars with Ba abundance uncertainties greater than 0.5 dex are omitted from the table and from our subsequent analysis.

5.3 Mixing on the RGB

Low-mass stars, such as those in M15, experience mixing events as they evolve off the main sequence (see the review by Karakas and Lattanzio, 2014). The first mixing episode is the first dredge-up (FDU), which occurs when the core is exhausted of hydrogen. The resulting contraction of the core drives the star to expand and its convective envelope to deepen. The FDU brings products of hydrogen burning (e.g., ^{13}C) to the surface. It also submerges and dilutes species that are only present on the stellar surface. The quintessential example of dilution at the FDU is ^{7}Li. Because ^{7}Li burns at a low temperature, it exists only in the outer layers of the star. The FDU dilutes the surface abundance as Li-poor material is dredged up to the surface.

The second mixing episode occurs at the luminosity function bump in the RGB. The convective envelope retreats in mass coordinate when the star is about halfway up the RGB. The retreating envelope leaves behind a discontinuity in mean molecular weight. As the hydrogen burning shell expands in mass coordinate, it eventually crosses this discontinuity, causing a brief pause in the star's ascent up the RGB. It is here that "extra mixing"—most likely thermohaline mixing (Charbonnel and Zahn, 2007)—has been observed in several species, including C and Li (R. G. Gratton et al., 2000).

If a NSM polluted the surfaces of stars in M15 long after they formed, then the surface compositions of the stars would be different from their centers. Mixing at the FDU and the RGB bump would dilute the r-process species that originated in the NSM. Therefore, we search for dilution signatures of Ba in M15 at the stellar luminosities that correspond to these two mixing episodes.

To further quantify the observational signature of external pollution, we use Modules for Experimentation in Stellar Astrophysics (MESA, Paxton et al., 2011) to simulate the dilution at the FDU of an r-process pollution event. We simulate the post-main

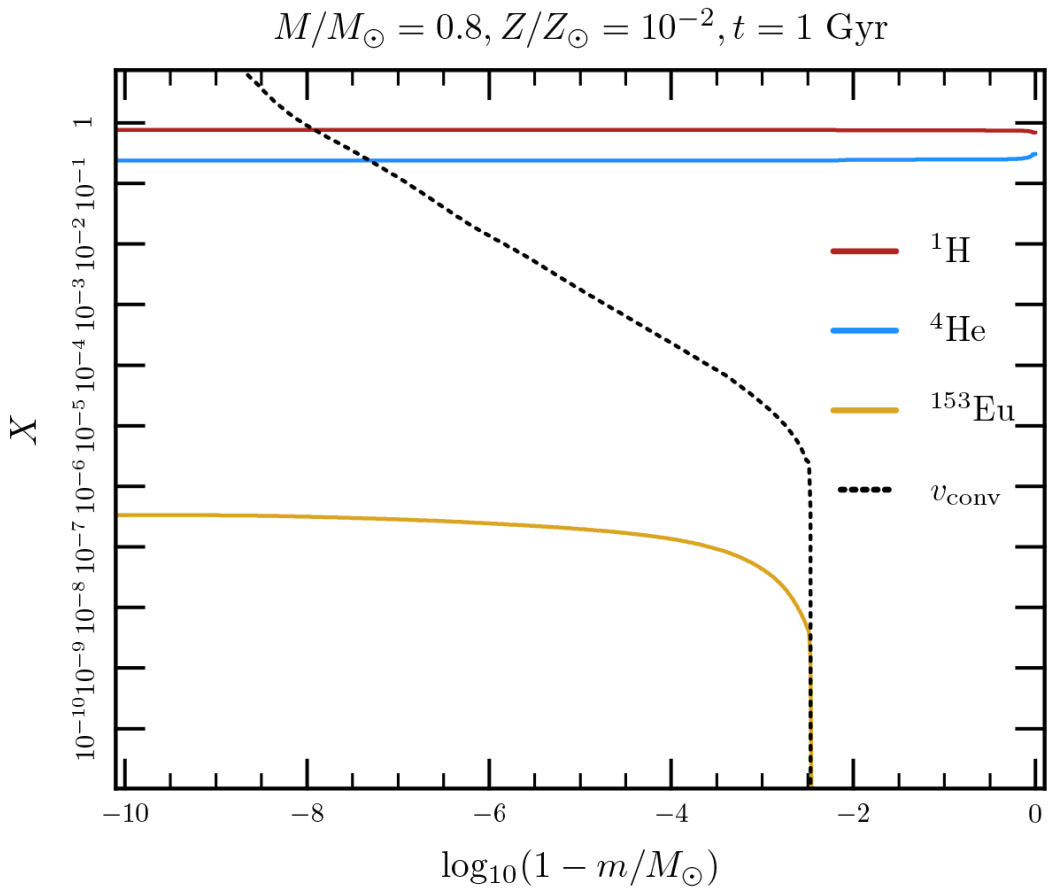

Figure 5.1: The initial conditions for a MESA model of a star polluted by an *r*-process event. The left edge of the plot represents the stellar surface. The dashed curve shows the convective velocity. The envelope ends where the curves become vertical.

sequence evolution of a 0.8 $M_\odot$ star with [Fe/H] = −2, roughly corresponding to stars at the MSTO in M15. Figure 5.1 shows the initial conditions of the star. Some *r*-process material, represented by ^{153}Eu, pollutes the surface of the star. Convection mixes this material throughout the convective envelope but no deeper. Figure 5.2 shows the evolution of ^{153}Eu abundance as the star increases in brightness. After some turbulence on the subgiant branch, the FDU depletes the surface abundance of ^{153}Eu by a factor of $\sim$ 30, or 1.5 dex. If this scenario is playing out in M15, then we expect to see such a depletion in the abundances of all *r*-process elements, including our Ba measurements.

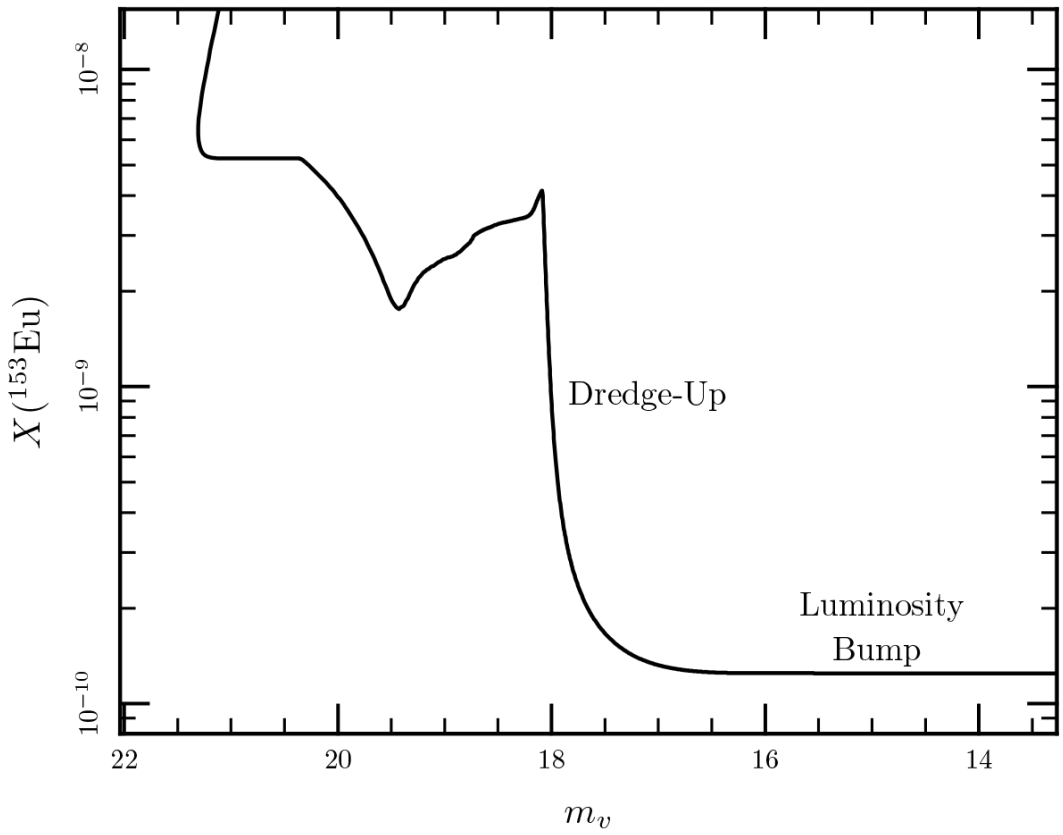

Figure 5.2: Evolution of surface-polluting *r*-process material as a function of apparent magnitude in M15. The FDU causes the steep decline at $V = 18$.

5.4 Results

Figure 5.3 summarizes our abundance measurements. The central panel shows the positions of our spectroscopic targets in the CMD in terms of absolute magnitude, where we used a distance modulus of $m - M = 15.40$ (Durrell and Harris, 1993). The right panel shows Ba abundances as a function of absolute magnitude. For reference, the left panel shows Li abundance measurements in both M15 (Kirby et al., 2016) and NGC 6397 (Lind et al., 2009), another metal-poor GC. We use NGC 6397 as a benchmark because its proximity permits exquisite spectroscopy even at the main sequence. The measurements in M15 are not of sufficient quality to fully illustrate the mixing episodes. The detections of Li trace the upper envelope of the true underlying Li abundance distribution.

The Ba abundances exhibit the $\sim$ 1 dex scatter that was already known to exist in M15. However, they show no trend with stellar luminosity. The mean [Ba/H] abundance at luminosities fainter than that expected for the FDU is -1.64 ± 0.10, where the mean is weighted by the inverse square of the uncertainties, and the error

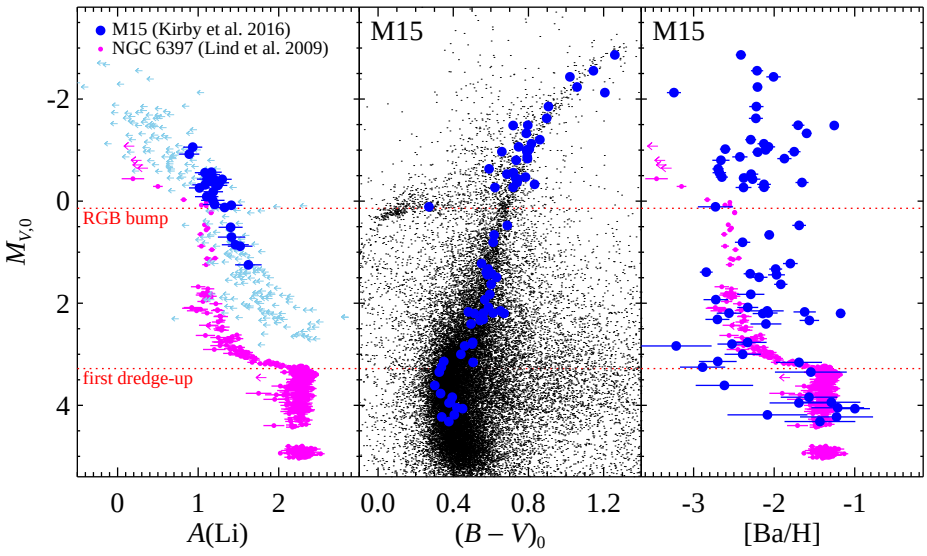

Figure 5.3: *Left:* As stars evolve up the RGB, Li is diluted. Measurements in M15 from DEIMOS (Kirby et al., 2016) are shown as large blue points and light blue upper limits. Higher quality measurements in NGC 6397 (small magenta points and upper limits, Lind et al., 2009) are also shown as a clearer demonstration of the dilution. *Center:* The color–magnitude diagram of M15 (small points, Stetson, 1994). Stars with Ba abundance measurements from DEIMOS are shown as large blue points. *Right:* DEIMOS measurements of [Ba/H] for stars at a variety of evolutionary phases in M15 (blue). The Li abundances in NGC 6397, shifted by an arbitrary constant, are shown in magenta to illustrate the expected dilution if Ba were present only on the stellar surface. The blue points in the center and right panels represent the same stars. Red dotted lines indicate the absolute magnitudes of the FDU and RGB bump.

bar is the standard error of the mean. The mean abundance is -2.11 ± 0.01 for stars brighter than the RGB bump, and -2.03 ± 0.02 for stars between the two mixing episodes. The abundances do not show the expected $\sim$ 1.5 dex decrease at the FDU, nor do they show the steady decline expected from extra mixing after the RGB bump.

The fact that the mean abundance is higher for main sequence stars is almost certainly a result of selection bias. The Ba measurements become less certain at fainter magnitudes, as reflected by the increasing error bars as a function of increasing magnitude in Figure 5.3. We experimented with relaxing the error cut to 1.0 dex. In that case, the difference in [Ba/H] abundance above and below the FDU decreases from 0.39 dex to 0.30 dex. Therefore, we conclude that selection against Ba-poor faint stars causes at least some of the apparent dependence of Ba abundance on luminosity. Regardless, any observed decrease in abundance at the

FDU is short of what we expected in the external pollution scenario.

5.5 Discussion

The giants would have lower Ba abundances than main sequence stars in M15 if Ba and other *r*-process elements originated in a NSM that occurred long after the cluster finished forming. We did not observe the expected decline in abundance. Therefore, Ba in M15 stars is well-mixed throughout the star. We conclude that the *r*-process elements in M15 were generated before or during the formation of the cluster.

This is not the first study to measure the abundances of neutron-capture elements on the main sequence in globular clusters. Other clusters with measurements of neutron-capture abundances on or near the main sequence include M92 (King et al., 1998), M5 (Ramírez and Cohen, 2003), 47 Tuc, NGC 6397, NGC 6752 (James, François, Bonifacio, E. Carretta, et al., 2004; James, François, Bonifacio, A. Bragaglia, et al., 2004), and M13 (Cohen and Meléndez, 2005). In no cluster does the abundance of heavy elements depend on evolutionary state. The unique aspect of this study is that M15 was an especially interesting candidate due to its large scatter in neutron-capture abundances, which might be expected if the NSM had preferentially polluted the stars closest to it.

Our study rules out a source with a delay time greater than the cluster formation time, but it does not necessarily rule out a NSM altogether. As mentioned earlier, dense cluster environments can accelerate the dynamical evolution of compact binaries so that the NSM delay times would be shorter than in the field (Ramirez-Ruiz et al., 2015). However, M15 is likely not dense enough to cause dynamically driven NSMs. Still, Zevin et al. (2019) argued that it is possible for a binary neutron star system, formed from the first generation of stars in the GC, to merge within the cluster lifetime (30–50 Myr). This scenario requires many conditions to be true, including Case BB mass transfer and the ability for the NSM to enrich the cluster despite any natal kick. In summary, we have ruled out one channel for *r*-process enrichment in M15, but the possibilities remain numerous.

ACKNOWLEDGEMENTS

This material is based upon work supported by the National Science Foundation under Grant No. AST-1847909. E.N.K. gratefully acknowledges support from a Cottrell Scholar award administered by the Research Corporation for Science

Advancement as well as funding from generous donors to the California Institute of Technology.

We are grateful to the many people who have worked to make the Keck Telescope and its instruments a reality and to operate and maintain the Keck Observatory. The authors wish to extend special thanks to those of Hawaiian ancestry on whose sacred mountain we are privileged to be guests. Without their generous hospitality, none of the observations presented herein would have been possible. We express our deep gratitude to the staff at academic and telescope facilities whose labor maintains spaces for scientific inquiry.

Facility: Keck:II (DEIMOS).
Software: spec2d (Cooper et al., 2012; Newman et al., 2013), MOOG (C. A. Sneden, 1973; Chris Sneden et al., 2012), MESA (Paxton et al., 2011).

Table 5.1: Barium Abundances in M15

Star	R.A. (J2000)	Decl. (J2000)	$M_{V,0}$ (mag)	$(B-V)_0$ (mag)	$v_{\rm helio}$ (km s^{-1})	$T_{\rm eff}$ (K)	log g (g in cm s^{-2})	[Fe/H] (dex)	[Ba/H] (dex)
41376	21 29 59.34	+12 09 11.9	−2.87	1.26	−98.9 ± 2.1	4231	0.68	−2.45 ± 0.10	−2.41 ± 0.06
40809	21 29 59.17	+12 10 16.0	−2.56	1.15	−109.1 ± 2.1	4790	1.04	−2.53 ± 0.10	−2.21 ± 0.08
36569	21 29 57.94	+12 10 17.0	−2.44	1.02	−119.5 ± 2.1	4409	0.86	−2.52 ± 0.10	−2.01 ± 0.09
31227	21 29 56.32	+12 09 54.8	−2.24	1.06	−97.9 ± 2.1	4470	1.06	−2.49 ± 0.10	−2.21 ± 0.06
38742	21 29 58.55	+12 09 49.8	−2.13	1.21	−105.1 ± 2.1	5176	1.10	−2.73 ± 0.10	−3.24 ± 0.09
41670	21 29 59.43	+12 10 11.7	−1.85	0.91	−103.8 ± 2.1	4832	1.40	−2.49 ± 0.10	−2.22 ± 0.09
60808	21 30 15.67	+12 08 23.3	−1.62	0.90	−110.2 ± 2.1	4722	1.46	−2.37 ± 0.10	−2.23 ± 0.09
43593	21 30 00.05	+12 09 18.6	−1.49	0.80	−111.6 ± 2.1	4958	1.61	−2.40 ± 0.10	−1.70 ± 0.08
54055	21 30 06.97	+12 07 46.8	−1.48	0.72	−112.7 ± 2.1	5159	1.64	−2.34 ± 0.10	−1.25 ± 0.04
16135	21 29 43.55	+12 10 03.7	−1.33	0.79	−101.3 ± 2.1	4986	1.63	−2.36 ± 0.10	−1.60 ± 0.06
33889	21 29 57.17	+12 09 42.6	−1.20	0.86	−128.9 ± 2.1	4820	1.72	−2.50 ± 0.10	−2.29 ± 0.07
59959	21 30 14.28	+12 09 23.8	−1.12	0.82	−105.5 ± 2.1	4771	1.70	−2.43 ± 0.10	−2.13 ± 0.08
48120	21 30 01.83	+12 09 49.2	−1.06	0.75	−113.8 ± 2.1	4741	1.65	−2.40 ± 0.10	−2.07 ± 0.08
44027	21 30 00.19	+12 09 56.2	−1.02	0.80	−110.7 ± 2.1	4963	1.77	−2.60 ± 0.10	−2.61 ± 0.07
55914	21 30 08.96	+12 08 49.3	−1.00	0.79	−118.4 ± 2.1	4850	1.76	−2.40 ± 0.10	−2.11 ± 0.08
49483	21 30 02.77	+12 10 38.4	−0.97	0.66	−115.0 ± 2.1	5217	1.93	−2.47 ± 0.10	−1.75 ± 0.08

Continued on next page

Table 5.1 – *Continued from previous page*

Star	R.A.	Decl.	$M_{V,0}$	$(B-V)_0$	$v_{\rm helio}$	$T_{\rm eff}$	log g	[Fe/H]	[Ba/H]
45688	21 30 00.76	+12 09 51.9	−0.96	0.79	−94.6 ± 2.1	4901	1.78	−2.40 ± 0.10	−2.20 ± 0.07
51057	21 30 04.02	+12 08 58.1	−0.87	0.79	−109.5 ± 2.1	4846	1.85	−2.46 ± 0.10	−2.43 ± 0.09
47982	21 30 01.75	+12 10 18.7	−0.83	0.79	−113.8 ± 2.1	4957	1.89	−2.34 ± 0.10	−1.87 ± 0.09
49428	21 30 02.74	+12 09 00.5	−0.80	0.73	−114.7 ± 2.1	4716	1.84	−2.71 ± 0.10	−2.66 ± 0.11
32206	21 29 56.66	+12 09 52.0	−0.63	0.59	−97.5 ± 2.1	5541	2.08	−2.61 ± 0.10	−2.70 ± 0.07
54512	21 30 07.50	+12 10 11.8	−0.56	0.72	−111.7 ± 2.1	4964	2.06	−2.53 ± 0.10	−2.68 ± 0.08
34335	21 29 57.30	+12 10 19.4	−0.53	0.69	−121.2 ± 2.1	4999	2.00	−2.46 ± 0.10	−2.29 ± 0.09
46494	21 30 01.06	+12 09 51.3	−0.47	0.78	−114.8 ± 2.1	4938	1.98	−2.48 ± 0.10	−2.65 ± 0.07
29005	21 29 55.28	+12 09 43.9	−0.45	0.73	−103.3 ± 2.1	4871	2.00	−2.42 ± 0.10	−2.38 ± 0.06
42594	21 29 59.73	+12 10 10.1	−0.43	0.74	−105.5 ± 2.1	5020	2.00	−2.44 ± 0.10	−2.27 ± 0.10
50124	21 30 03.27	+12 10 11.1	−0.37	0.74	−113.1 ± 2.1	4982	2.10	−2.47 ± 0.10	−1.65 ± 0.08
57863	21 30 11.27	+12 10 15.0	−0.33	0.83	−100.4 ± 2.1	4842	2.13	−2.72 ± 0.11	−2.13 ± 0.09
52787	21 30 05.58	+12 07 05.5	−0.27	0.72	−112.3 ± 2.1	5088	2.11	−2.21 ± 0.10	−2.13 ± 0.07
37854	21 29 58.30	+12 09 54.1	−0.27	0.62	−113.2 ± 2.1	4963	2.09	−2.59 ± 0.10	−2.38 ± 0.10
28721	21 29 55.13	+12 10 22.8	+0.11	0.27	−92.1 ± 2.2	6427	2.65	−2.33 ± 0.11	−2.73 ± 0.22
52771	21 30 05.57	+12 08 33.0	+0.47	0.69	−109.0 ± 2.1	5197	2.48	−2.41 ± 0.10	−1.69 ± 0.08
55135	21 30 08.16	+12 08 54.3	+0.66	0.62	−106.2 ± 2.1	5173	2.58	−2.41 ± 0.10	−2.06 ± 0.06
22822	21 29 50.80	+12 09 51.9	+0.81	0.61	−102.7 ± 2.1	5219	2.60	−2.47 ± 0.10	−2.39 ± 0.10

Continued on next page

Table 5.1 – *Continued from previous page*

Star	R.A.	Decl.	$M_{V,0}$	$(B-V)_0$	$v_{\rm helio}$	$T_{\rm eff}$	log g	[Fe/H]	[Ba/H]
55541	21 30 08.54	+12 08 43.4	+1.22	0.55	−105.0 ± 2.1	5391	2.88	−2.34 ± 0.11	−1.80 ± 0.09
54237	21 30 07.18	+12 08 38.6	+1.33	0.59	−115.9 ± 2.1	5352	2.89	−2.40 ± 0.11	−1.98 ± 0.08
17122	21 29 44.89	+12 09 21.1	+1.39	0.58	−106.6 ± 2.1	5249	2.87	−2.60 ± 0.10	−2.84 ± 0.08
56979	21 30 10.17	+12 09 14.6	+1.42	0.60	−117.6 ± 2.1	5336	2.94	−2.40 ± 0.10	−2.30 ± 0.08
61191	21 30 16.32	+12 08 05.9	+1.44	0.58	−116.2 ± 2.1	5471	2.98	−2.42 ± 0.11	−1.97 ± 0.10
57312	21 30 10.57	+12 10 27.3	+1.49	0.63	−117.5 ± 2.1	5175	3.00	−2.68 ± 0.11	−2.19 ± 0.10
15681	21 29 42.91	+12 10 57.3	+1.63	0.60	−105.0 ± 2.1	5275	3.02	−2.39 ± 0.10	−1.92 ± 0.08
56947	21 30 10.14	+12 07 12.2	+1.82	0.59	−108.4 ± 2.2	5492	3.13	−2.45 ± 0.11	−2.29 ± 0.17
8920	21 29 28.21	+12 10 15.6	+1.93	0.57	−110.7 ± 2.2	5428	3.22	−2.58 ± 0.11	−2.72 ± 0.15
61776	21 30 17.39	+12 08 17.1	+2.08	0.59	−113.0 ± 2.5	5524	3.23	−2.43 ± 0.13	−2.33 ± 0.13
50825	21 30 03.82	+12 09 58.2	+2.15	0.65	−106.5 ± 2.2	5349	3.20	−2.34 ± 0.11	−2.09 ± 0.21
61068	21 30 16.10	+12 08 14.6	+2.17	0.48	−115.9 ± 2.2	5464	3.35	−2.40 ± 0.12	−1.62 ± 0.14
59374	21 30 13.38	+12 08 45.2	+2.19	0.61	−106.9 ± 2.2	5400	3.32	−2.47 ± 0.11	−2.07 ± 0.12
56251	21 30 09.34	+12 06 43.3	+2.19	0.56	−115.8 ± 2.2	5431	3.25	−2.27 ± 0.11	−2.56 ± 0.15
31125	21 29 56.28	+12 10 16.8	+2.20	0.67	−111.1 ± 2.1	4549	3.62	−2.08 ± 0.10	−1.18 ± 0.06
58363	21 30 11.91	+12 07 10.7	+2.20	0.51	−114.8 ± 2.2	5562	3.35	−2.35 ± 0.12	−2.14 ± 0.13
11998	21 29 36.32	+12 08 23.6	+2.32	0.56	−113.6 ± 2.2	5621	3.36	−2.45 ± 0.12	−2.70 ± 0.15
59071	21 30 12.95	+12 09 46.5	+2.34	0.54	−108.0 ± 2.3	5519	3.40	−2.38 ± 0.11	−1.56 ± 0.12

Continued on next page

Table 5.1 – *Continued from previous page*

Star	R.A.	Decl.	$M_{V,0}$	$(B-V)_0$	v_{helio}	T_{eff}	$\log g$	[Fe/H]	[Ba/H]
62219	21 30 18.20	+12 07 24.8	+2.41	0.49	−108.5 ± 2.3	5711	3.43	−2.45 ± 0.16	−2.10 ± 0.19
6374	21 29 17.88	+12 10 39.9	+2.77	0.50	−103.5 ± 4.9	6042	3.67	−2.46 ± 0.30	−2.33 ± 0.24
7175	21 29 21.57	+12 10 20.8	+2.80	0.50	−108.7 ± 2.4	5896	3.66	−2.91 ± 0.25	−2.52 ± 0.18
58890	21 30 12.65	+12 06 41.7	+2.84	0.46	−116.9 ± 2.4	5813	3.62	−2.72 ± 0.20	−3.22 ± 0.44
23303	21 29 51.28	+12 08 50.3	+3.00	0.44	−102.7 ± 2.3	6098	3.83	−2.49 ± 0.16	−2.39 ± 0.23
18956	21 29 47.04	+12 09 48.6	+3.14	0.35	−109.7 ± 2.7	6162	3.89	−2.65 ± 0.18	−2.70 ± 0.23
26974	21 29 54.04	+12 10 33.2	+3.16	0.51	−100.4 ± 2.9	6101	3.91	−2.34 ± 0.18	−1.69 ± 0.29
18422	21 29 46.41	+12 09 46.4	+3.25	0.34	−103.7 ± 2.5	6213	3.93	−2.99 ± 0.30	−2.89 ± 0.28
22363	21 29 50.36	+12 10 30.8	+3.35	0.33	−104.6 ± 8.4	6263	4.01	−2.28 ± 0.39	−1.54 ± 0.45
18685	21 29 46.73	+12 10 38.1	+3.61	0.30	−109.6 ± 5.5	6173	4.07	−2.62 ± 0.23	−2.62 ± 0.36
21703	21 29 49.76	+12 09 15.8	+3.77	0.33	−109.9 ± 3.5	6497	4.28	−3.22 ± 0.49	−5.22 ± 0.43
16177	21 29 43.61	+12 09 17.1	+3.84	0.39	−119.4 ± 3.7	6093	4.17	−2.10 ± 0.19	−1.57 ± 0.35
8227	21 29 25.80	+12 11 45.7	+3.94	0.39	−113.3 ± 3.4	6709	4.38	−1.95 ± 0.23	−1.29 ± 0.36
12699	21 29 37.77	+12 09 02.4	+3.95	0.38	−108.3 ± 3.5	6791	4.38	−2.44 ± 0.46	−1.69 ± 0.36
7834	21 29 24.29	+12 12 10.4	+4.05	0.42	−115.3 ± 7.1	6575	4.34	−2.50 ± 0.35	−1.21 ± 0.33
8868	21 29 28.04	+12 11 46.2	+4.06	0.45	−104.7 ± 5.0	6663	4.43	−2.06 ± 0.30	−1.00 ± 0.19
9864	21 29 31.05	+12 09 01.0	+4.19	0.41	−113.2 ± 4.0	6323	4.36	−2.25 ± 0.26	−2.08 ± 0.50
7436	21 29 22.71	+12 09 00.6	+4.23	0.34	−119.0 ± 29.7	6541	4.41	−1.91 ± 0.30	−1.23 ± 0.45

Continued on next page

Table 5.1 – *Continued from previous page*

Star	R.A.	Decl.	$M_{V,0}$	$(B-V)_0$	$v_{\rm helio}$	$T_{\rm eff}$	log g	[Fe/H]	[Ba/H]
8447	21 29 26.60	+12 11 46.1	+4.32	0.38	-114.5 ± 7.0	6496	4.41	-2.10 ± 0.26	-1.43 ± 0.44

References—Photometry sourced from Stetson (1994).

References

Bastian, Nate and Carmela Lardo (2018). "Multiple Stellar Populations in Globular Clusters". In: *ARA&A* 56, pp. 83–136. DOI: 10.1146/annurev-astro-081817-051839. arXiv: 1712.01286 [astro-ph.SR].

Charbonnel, C. and J.-P. Zahn (2007). "Thermohaline mixing: a physical mechanism governing the photospheric composition of low-mass giants". In: *A&A* 467, pp. L15–L18. DOI: 10.1051/0004-6361:20077274. eprint: astro-ph/0703302.

Chornock, R. et al. (2017). "The Electromagnetic Counterpart of the Binary Neutron Star Merger LIGO/Virgo GW170817. IV. Detection of Near-infrared Signatures of r-process Nucleosynthesis with Gemini-South". In: *ApJL* 848.2, L19, p. L19. DOI: 10.3847/2041-8213/aa905c. arXiv: 1710.05454 [astro-ph.HE].

Cohen, J. G. and J. Meléndez (2005). "Abundances in a Large Sample of Stars in M3 and M13". In: *AJ* 129, pp. 303–329. DOI: 10.1086/426369. eprint: astro-ph/0409725.

Cooper, M. C. et al. (2012). *spec2d: DEEP2 DEIMOS Spectral Pipeline*. Astrophysics Source Code Library. ascl: 1203.003.

de los Reyes, M. A. C., E. N. Kirby, and K. J. Shen (2019). "Using Manganese to Probe the Physics of Type Ia Supernovae". In: *ApJ, submitted*.

Duggan, Gina E. et al. (2018). "Neutron Star Mergers are the Dominant Source of the r-process in the Early Evolution of Dwarf Galaxies". In: *ApJ* 869.1, 50, p. 50. DOI: 10.3847/1538-4357/aaeb8e. arXiv: 1809.04597 [astro-ph.GA].

Durrell, Patrick R. and William E. Harris (1993). "A Color-Magnitude Study of the Globular Cluster M15". In: *AJ* 105, p. 1420. DOI: 10.1086/116521.

Gratton, R. G. et al. (2000). "Mixing along the red giant branch in metal-poor field stars". In: *A&A* 354, pp. 169–187.

Gratton, R., C. Sneden, and E. Carretta (2004). "Abundance Variations Within Globular Clusters". In: *ARA&A* 42, pp. 385–440. DOI: 10.1146/annurev.astro.42.053102.133945.

Gratton, Raffaele G., Eugenio Carretta, and Angela Bragaglia (2012). "Multiple populations in globular clusters. Lessons learned from the Milky Way globular clusters". In: *A&A Rv* 20, 50, p. 50. DOI: 10.1007/s00159-012-0050-3. arXiv: 1201.6526 [astro-ph.SR].

Ishigaki, M. N., W. Aoki, and M. Chiba (2013). "Chemical Abundances of the Milky Way Thick Disk and Stellar Halo. II. Sodium, Iron-peak, and Neutron-capture Elements". In: *ApJ* 771.1, 67, p. 67. DOI: 10.1088/0004-637X/771/1/67. arXiv: 1306.0954 [astro-ph.GA].

James, G., P. François, P. Bonifacio, A. Bragaglia, et al. (2004). "Heavy elements abundances in turn-off stars and early subgiants in NGC 6752". In: *A&A* 414, pp. 1071–1079. DOI: 10.1051/0004-6361:20034014. arXiv: astro-ph/0311278 [astro-ph].

James, G., P. François, P. Bonifacio, E. Carretta, et al. (2004). "Heavy elements and chemical enrichment in globular clusters". In: *A&A* 427, pp. 825–838. DOI: 10.1051/0004-6361:20041512. arXiv: astro-ph/0408330 [astro-ph].

Kalogera, V. et al. (2001). "The Coalescence Rate of Double Neutron Star Systems". In: *ApJ* 556.1, pp. 340–356. DOI: 10.1086/321583. arXiv: astro-ph/0012038 [astro-ph].

Karakas, Amanda I. and John C. Lattanzio (2014). "The Dawes Review 2: Nucleosynthesis and Stellar Yields of Low- and Intermediate-Mass Single Stars". In: *PASA* 31, e030, e030. DOI: 10.1017/pasa.2014.21. arXiv: 1405.0062 [astro-ph.SR].

Kasen, Daniel et al. (2017). "Origin of the heavy elements in binary neutron-star mergers from a gravitational-wave event". In: *Nature* 551.7678, pp. 80–84. DOI: 10.1038/nature24453. arXiv: 1710.05463 [astro-ph.HE].

King, Jeremy R. et al. (1998). "Keck HIRES Spectroscopy of M92 Subgiants: Surprising Abundances near the Turnoff". In: *AJ* 115.2, pp. 666–684. DOI: 10.1086/300209.

Kirby, E. N. et al. (2016). "Lithium-rich Giants in Globular Clusters". In: *ApJ* 819, 135, p. 135. DOI: 10.3847/0004-637X/819/2/135. arXiv: 1601.01315 [astro-ph.SR].

Lind, K. et al. (2009). "Signatures of intrinsic Li depletion and Li-Na anti-correlation in the metal-poor globular cluster NGC 6397". In: *A&A* 503, pp. 545–557. DOI: 10.1051/0004-6361/200912524. arXiv: 0906.2876 [astro-ph.SR].

Meyer, B. S. et al. (1992). "R-Process Nucleosynthesis in the High-Entropy Supernova Bubble". In: *ApJ* 399, p. 656. DOI: 10.1086/171957.

Mösta, Philipp et al. (2018). "r-process Nucleosynthesis from Three-dimensional Magnetorotational Core-collapse Supernovae". In: *ApJ* 864.2, 171, p. 171. DOI: 10.3847/1538-4357/aad6ec. arXiv: 1712.09370 [astro-ph.HE].

Newman, J. A. et al. (2013). "The DEEP2 Galaxy Redshift Survey: Design, Observations, Data Reduction, and Redshifts". In: *ApJS* 208, 5, p. 5. DOI: 10.1088/0067-0049/208/1/5. arXiv: 1203.3192 [astro-ph.CO].

Nishimura, Nobuya, Tomoya Takiwaki, and Friedrich-Karl Thielemann (2015). "The r-process Nucleosynthesis in the Various Jet-like Explosions of Magnetorotational Core-collapse Supernovae". In: *ApJ* 810.2, 109, p. 109. DOI: 10.1088/0004-637X/810/2/109. arXiv: 1501.06567 [astro-ph.SR].

Paxton, Bill et al. (2011). "Modules for Experiments in Stellar Astrophysics (MESA)". In: *ApJS* 192.1, 3, p. 3. DOI: 10.1088/0067-0049/192/1/3. arXiv: 1009.1622 [astro-ph.SR].

Qian, Y. -Z. and S. E. Woosley (1996). "Nucleosynthesis in Neutrino-driven Winds. I. The Physical Conditions". In: *ApJ* 471, p. 331. DOI: 10.1086/177973. arXiv: astro-ph/9611094 [astro-ph].

Ramírez, S. V. and J. G. Cohen (2003). "Abundances in Stars from the Red Giant Branch Tip to near the Main-Sequence Turnoff in M5". In: *AJ* 125, pp. 224–245. DOI: 10.1086/345510. eprint: astro-ph/0210245.

Ramirez-Ruiz, Enrico et al. (2015). "Compact Stellar Binary Assembly in the First Nuclear Star Clusters and r-process Synthesis in the Early Universe". In: *ApJL* 802.2, L22, p. L22. DOI: 10.1088/2041-8205/802/2/L22. arXiv: 1410.3467 [astro-ph.GA].

Roederer, Ian U. (2011). "Primordial r-process Dispersion in Metal-poor Globular Clusters". In: *ApJL* 732.1, L17, p. L17. DOI: 10.1088/2041-8205/732/1/L17. arXiv: 1104.5056 [astro-ph.GA].

Skúladóttir, Ása et al. (2019). "Neutron-capture elements in dwarf galaxies I: Chemical clocks & the short timescale of the *r*-process". In: *arXiv e-prints*, arXiv:1908.10729, arXiv:1908.10729. arXiv: 1908.10729 [astro-ph.GA].

Sneden, C. A. (1973). "Carbon and Nitrogen Abundances in Metal-Poor Stars." PhD thesis. University of Texas Austin.

Sneden, C., J. Johnson, et al. (2000). "Neutron-Capture Element Abundances in the Globular Cluster M15". In: *ApJL* 536, pp. L85–L88. DOI: 10.1086/312742.

Sneden, C., R. P. Kraft, et al. (1997). "Star-To-Star Abundance Variations Among Bright Giants in the Metal-Poor Globular Cluster M15". In: *AJ* 114, p. 1964. DOI: 10.1086/118618.

Sneden, C., C. A. Pilachowski, and R. P. Kraft (2000). "Barium and Sodium Abundances in the Globular Clusters M15 and M92". In: *AJ* 120, pp. 1351–1363. DOI: 10.1086/301509.

Sneden, Chris et al. (2012). *MOOG: LTE line analysis and spectrum synthesis*. ascl: 1202.009.

Sobeck, J. S. et al. (2011). "The Abundances of Neutron-capture Species in the Very Metal-poor Globular Cluster M15: A Uniform Analysis of Red Giant Branch and Red Horizontal Branch Stars". In: *AJ* 141, 175, p. 175. DOI: 10.1088/0004-6256/141/6/175. arXiv: 1103.1008 [astro-ph.SR].

Stetson, Peter B. (1994). "The Center of the Core-Cusp Globular Cluster M15: CFHT and HST Observations, ALLFRAME Reductions". In: *PASP* 106, p. 250. DOI: 10.1086/133378.

Truran, J. W. and Jr. Iben I. (1977). "On s-process nucleosynthesis in thermally pulsing stars." In: *ApJ* 216, pp. 797–810. DOI: 10.1086/155523.

van Oirschot, Pim et al. (2019). "Semi-analytic modelling of the europium production by neutron star mergers in the halo of the Milky Way". In: *MNRAS* 483.4, pp. 4397–4410. DOI: 10.1093/mnras/sty3383. arXiv: 1812.03218 [astro-ph.GA].

Worley, C. C. et al. (2013). "Ba and Eu abundances in M 15 giant stars". In: *A&A* 553, A47, A47. DOI: 10.1051/0004-6361/201321097. arXiv: 1302.6122 [astro-ph.SR].

Zevin, Michael et al. (2019). "Can Neutron-Star Mergers Explain the r-process Enrichment in Globular Clusters?" In: *arXiv e-prints*, arXiv:1906.11299, arXiv:1906.11299. arXiv: 1906.11299 [astro-ph.HE].

Chapter 6

ALIGNING THE ZTF SCIENCE FOCAL PLANE USING STELLAR IMAGES

Duggan, G. E., R. Dekany, and J. Milburn (2018). "Aligning the ZTF science focal plane using stellar images". In: *Ground-based and Airborne Instrumentation for Astronomy VII*. Vol. 10702. Society of Photo-Optical Instrumentation Engineers (SPIE) Conference Series, 107024K. DOI: 10.1117/12.2309994.

ABSTRACT

The Zwicky Transient Facility (ZTF) is a next-generation, optical, synoptic survey that leverages the success of the Palomar Transient Factory (PTF). ZTF has a large science focal plane (SFP) that needs to be aligned such that all portions of the CCDs are simultaneously placed in focus to optimize the survey's efficiency. The SFP consists of 16 large, wafer-scale science CCDs, which are mosaicked to achieve 47 $\deg^2$ field of view. The SFP is aligned by repositioning each CCD based on the measured height map, which is a map of the camera's z position at which each portion of the CCD is in focus. This height map is measured using on-sky stellar images in order to recreate the optical path that will be used throughout the survey. We present our technique for placing the SFP in focus, which includes two different methods to measure the height map of the SFP. The first method measures the height at which a star is in focus by fitting a parabola to each star's photometric width as the star is moved in and out of focus. The second method measures the height by decomposing a defocused star into its image moments. We will discuss the strengths and limitations of each method and their outputs. By repositioning the CCDs, we were able to reduce the standard deviation of the height map from 33 to 14 microns, which improved the survey's speed by $\sim 81\%$.

6.1 Introduction

ZTF is a high-efficiency, wide-field, optical, time-domain survey developed to explore new parameter space for short-cadence science and to develop scientific utilization infrastructure in preparation for the Large Synoptic Survey Telescope (LSST). The ZTF Observing System (OS) consists of the 1.2-meter diameter Samuel Oschin

Telescope at Palomar Mountain. The OS is outfitted with a ZTF Camera (Dekany et al., 2016) containing a new 640 Mpix 16 CCD mosaic science focal plane (SFP). The SFP is housed in a vacuum cryostat, positioned with a hexapod, and located at the prime focus of the Schmidt telescope system.

ZTF is an updated version of the Palomar Transient Factory (PTF) with new hardware and software. ZTF is designed to dramatically improve the survey speed of PTF. Improvements, including new CCDs and updated telescope slewing mechanisms, enable the exposure time per image and overhead between images to be decreased by a factor of two and three, respectively. Arguably the most important improvement is increasing the field of view by a factor of seven—from 7.26 to 47 $\deg^2$. All of these improvements combine to provide an areal survey rate of 3,750 $\deg^2$/hr, which will enable ZTF to scan the viewable sky (3π) an average of 290 times per year.

The 47-$\deg^2$ SFP presents a technical challenge: positioning all areas of the SFP in focus simultaneously. This is important for the survey's sensitivity, since having a portion of the SFP always out of focus reduces the average limiting magnitude of the stars ZTF is able to observe or increases the time needed to achieve a given limiting magnitude. The engineering requirement is to measure the SFP with 10 μm precision in order to achieve the desired photometric sensitivity.

We present two different methods to create a height map, which is a map proportional to the height of each pixel across the entire SFP. Both of these methods utilize on-sky images. This provides a distinct advantage over lab profilometry imaging, because we are replicating the conditions that will be used throughout the survey. The final SFP height map is an average of the maps produced by each method. The ZTF camera was brought back to the lab to re-shim the CCD supports to minimize height differences across the SFP. Then the ZTF camera was re-installed, and we report the improvement to the height variation across the SFP and the resulting improvement in survey efficiency.

6.2 Placing the science focal plane in approximate focus

In May 2017, the ZTF cryostat was installed into the Oschin Telescope in a temporary optical configuration, which did not fully conform to the ZTF OS optical design (Reiley et al., 2017). Due to vendor delays, a large aspheric plate, needed to compensate for spherical aberration induced by the thick cryostat window, was not available for these tests. Based on Zemax design analysis, the absence of this aspheric plate resulted in aberrations present at all points of the ZTF optical field that

are described by a Seidel spherical wavefront aberration coefficient of $W_{040} \sim -7.0$ waves. With a R-band filter, this results in a shift of focus to achieve the minimum root mean square (RMS) spot size of

$$\delta z = 8(F/\#)^2 \times \left(-\frac{4}{3}W_{040}\right) = -\frac{32}{3}(F/\#)^2 W_{040} = -\frac{32}{3}(2.5)^2(-7\times 0.6\mu\text{m}) = 280\mu\text{m}, \tag{6.1}$$

relative to the paraxial focus that would be optimal in the absence of any optical aberrations. Here, we define positive motion to be in the direction from the prime focus toward the telescope primary mirror. However, a global shift in focus does not effect our measurements at all because we are measuring the relative heights in the SFP. The hexapod height at which each part of a CCD is in focus relative to one another (described by a 'height map') is independent of the large spherical aberration present during these experiments. The combination of this large spherical aberration and vignetting does effect our measurements, and we discuss this further in Secs. 6.3 and 6.3.

After installing the positioning hexapod onto the prime focus hub, the cryostat onto the hexapod, and the R-band optical filter to the front of the cryostat, we performed a coarse, initial, solid-body alignment of the cryostat relative to the telescope focal plane. We manually adjusted the hexapod z[1], tip, and tilt using field- and hexapod-z-dependent stellar image widths as the metric—see this surface map of the stellar full width at half maximum (FWHM) given in Fig. 6.1 as an example. By minimizing the stellar FWHMs seen in these maps, we are able to distinguish the optimal hexapod z position (i.e., the z position that places the majority of the SFP in focus) within 35 μm in variable seeing. Although roughly identifying the optimal z position is important, adjusting the tip and tilt to flatten the SFP is essential to measuring an accurate height map of the SFP. A visible gradient on the stellar FWHM map corresponds to a large global tip and/or tilt, which dramatically increases the range of z positions needed to place each section of the SFP in focus.

Following this, we obtained several series of through-focus scans by taking images at different z positions, which included positions above and below the optimal z position for the SFP that was found using our stellar FWHM map. We varied the

[1]Typically we refer to the hexapod axial as the 'focus'. However, to avoid confusion with the state of a star being 'in focus' and the hexapod position where that occurs, we will simply refer to this axis as z.

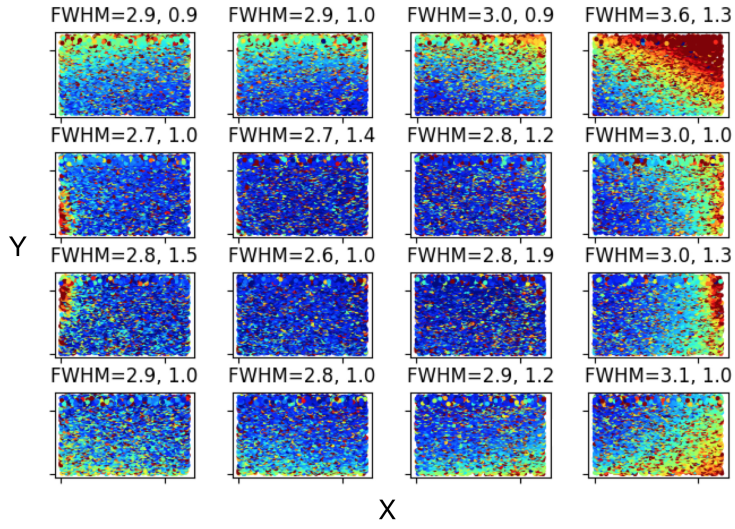

Figure 6.1: Stellar FWHM map of the SFP. This field-dependent stellar image FWHM was measured at the optimal hexapod z position obtained using rigid-body motions of the ZTF hexapod. This technique is used to place the SFP in approximate focus by adjusting the z, tip, and tilt of the hexapod. The FWHM color ranges from dark blue (FWHM = 2 pixels) to dark red (FWHM = 4 pixels). The FWHM average and standard deviation for each CCD is printed above each CCD (in the form FWHM = mean, std). With this method we estimate that we can identify the z position that places the majority of the SFP in focus within 35 μm.

camera exposure time of these images between 30 and 120 sec and varied the number of the different z positions between five and nine positions. This was done to explore both the dependency of our prepared analysis methods to out-of-focus distance and signal-to-noise ratio (S/N), which is a function of the number of sky- and read-noise pixels within the defocused stellar point spread function (PSF). We will discuss the optimal set of images selected for each method in the following sections.

6.3 Creating a height map of the science focal plane

The ultimate goal is to calculate a set of height adjustments to the CCDs required to bring the entire SFP into focus simultaneously. This is equivalent to calculating the hexapod z position (or height) where each section of the SFP is placed in focus. For example, if a section of the SFP reaches focus at a larger z value (relative to the rest of the SFP), one has to move that section of the CCD up relative to the cryostat body (or, e.g., the cryostat cold plate) to flatten the plane. In other words, the 'height' in height map refers to the height of the hexapod when the section is in focus and is actually the inverted map of the true shape of the CCDs, so the height map is

equivalent to the adjustments required to flatten the SFP. This section discusses how we create this height map of the SFP.

We generalize "each section" of the SFP to be each N x N pixel sub-frame of the image. In practice N = 512 was found to be the ideal sub-frame size, since it assures that a sufficient number of stars are present in the determination of the height for that section. The end result is a 48 x 48 pixel image with each CCD represented by a 12x12 sub-array and a total of 2,304 sections in the SFP.

Although all the pre- and post-processing is identical, we can determine the height for each section of the SFP by two different methods: parabola method and donut method. Each method is impacted differently by the sources of biases present in ZTF. Ultimately, these methods were in agreement and one did not appear inherently less biased, so we simply averaged the results of the two methods. We will discuss the theory behind each method, the main sources of bias, and the detailed procedure used to calculate a height map.

Parabola method: parabolic fits to FWHM

With the parabola method, the height at an individual star's position is determined by fitting a parabola to FWHM measurements of the star in images at different hexapod z positions. We tested this method in October 2015 on PTF to confirm the method's ability to measure a height map within ZTF's required precision of 10 μm.

Parabola algorithm

In the absence of diffraction and atmospheric or static design optical aberrations, we would expect the dependence of the stellar FWHM on z, as shown in Fig. 6.2, to be symmetric on both sides of focus (i.e., the hexapod z that places the star in focus, z_0). The aforementioned diffraction and aberrations, however, preclude the experimental reproduction of the idealized curve, and add a 'floor' value for RMS spot size ($s_{\mathrm{rms,min}}$). The RMS image radius, s_{rms}, is the sum in quadrature of $s_{\mathrm{rms,min}}$ and the linear dependence of the spot size on the defocus value ($z - z_0$). For relatively small defocus values, a taylor expansion shows that s_{rms} follows an approximately parabolic shape. In fact, we define the parabolic focus range as that over which this approximation is valid,

$$s_{\mathrm{rms}} = \langle \sqrt{\mathrm{K}(z - z_0)^2 + s_{\mathrm{rms,min}}^2} \rangle \propto \mathrm{K}' + \frac{1}{2}(z - z_0)^2 \tag{6.2}$$

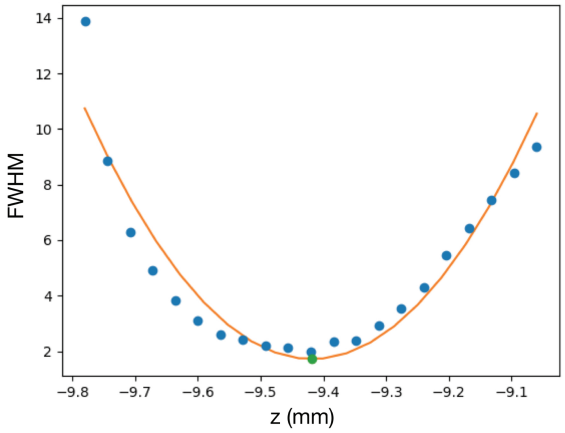

Figure 6.2: Measuring the height for a ZTF star using the parabola method. Here we fit a parabola (orange) to a single star's FWHM measured in many images (blue dots) to calculate the height where the hexapod places the star in focus (z_0, green dot). By averaging the standard deviation of the height returned by the parabolic fit for all stars, we measure an average height error of 15 μm for a single star. The shape deviation from an ideal parabola is due to the combination of spherical aberrations and vignetting.

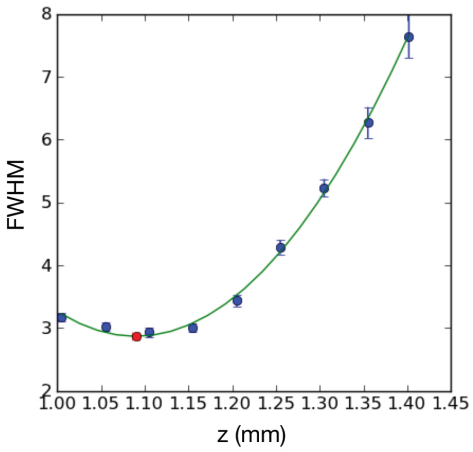

Figure 6.3: Measuring the height for a PTF star using the parabola method. We fit a parabola (green) to a single star's FWHM vs. z (blue dots) to calculate the height where the hexapod places the star in focus (z_0, red dot). The average standard deviation of the height is 4.6 μm for a single star.

for arbitrary constants, K and K′, which incorporate the F/# of the beam, the observing wavelength, and wavefront static RMS error. The important form of this equation is that it is symmetric in defocus value, meaning that z_0 is, to first order, independent of the physics incorporated into K′. Thus, simply by plotting and fitting a parabolic curve to the relationship between spot radius (or FWHM) and z, z_0 (a.k.a., the height at the star's position) can be obtained.

Sources of bias

Because the parabola method relies on the numerical best fit determination of the (local) parabolic minimum, the sources of focus error, or bias, are only those that result in a shift of this minimum location. Effects on the measured image size that are symmetrical in the defocus value (defined as $z - z_0$ in Sec. 6.3) are irrelevant to the determination of the minimum location. Spherical aberration, for example, results in an increase in image width that is symmetric on both sides of focus (i.e., z_0), and therefore does not impact the accuracy of the parabola method. Similarly,

vignetting alone introduces a bias into the measured image width as a function of field position due to the finite primary mirror diameter. However, this impact is symmetric with respect to the defocus value. Because the same vignetting bias applies on both sides of focus, and is constant for any given star position in the field, the measured parabola minimum remains unaffected. Note, the vignetting due to both the centrally obscuring cryostat and support shadows, which also depends on field location, has no first-order impact on the image size at all (in the absence of aberrations), as long as the central obscuration remains interior to the entrance pupil.

However, in the combined presence of both spherical aberration and vignetting, second-order biases impact the parabolic minimum location (i.e., z_0) in the parabola method. The details of the combined aberrations are complicated, and we attribute the deviations from the ideal parabolic shape in FWHM vs. z to the combined aberrations. The altered shape of ZTF's FWHM vs. z can be seen by comparing how well the best parabolic fit matches the observations for a single star in ZTF (Fig. 6.2) to PTF (Fig. 6.3), because the vignetting and spherical aberrations are significantly smaller in PTF. The altered shape of the ZTF observations results in increased uncertainty in the coefficient describing the parabolic minimum location (z_0) returned by the fitting algorithm (see Step 6 in Sec. 6.3). The standard deviation of z_0 for a given star increases on average from 4.6 to 15 μm with PTF and ZTF, respectively. Note that the deviations from the parabolic shape might be exacerbated by assuming a two-dimensional Gaussian PSF when measuring the FWHM of the stars.

Changes in atmospheric seeing during a through-focus scan could systematically increase or decrease the FWHM measured for a given star as z is changed, which would alter the z_0 measured. To adjust for this, we randomize the order we took the images, instead of steadily increasing or decreasing the z position. This way changes in seeing would increase the uncertainty when fitting for z_0, but would not bias it to a different z position.

Parabola procedure

Now that we understand the algorithm and biases, here we describe the detailed procedure used to measure the height for each section of the SFP using the parabola method.

Step 1: Collect images. We experimented with taking images of the same stars

with the hexapod z position changing by a fine step size of 0.04 mm steps (as seen in Fig. 6.2), but found that a step of 0.1 mm was sufficient. We need images 0.2 mm on either side of the highest and lowest section of the SFP in order to span the necessary z range to adequately measure the height of every section. In May on ZTF, this was achieved with nine 30 sec images from −8.92 to −9.72 mm with 0.1 mm steps, where the optimal hexapod z position (i.e., the z that places the majority of the SFP in focus) was −9.4 mm.

Step 2: Clean images. Images were sufficiently clean without bias or flat field corrections, so we only needed to use PyRAF[2] to correct for pre-scan and over-scan regions.

Step 3: Identify stars and measure properties. We used SExtractor (Bertin and Arnouts, 1996) to measure the x and y coordinates (in pixels) and the FWHM of the stars seen in each image. In order to apply S/N cuts we used SExtractor to measure the flux with a variety of different apertures and the background. We also had SExtractor return the elongation parameter to remove streaks.

Step 4: Purify star sample. To only include the cleanest sample of stars when measuring the height per SFP section, we reject the following groups of stars. We exclude all stars within 25 pixels of a CCD edge to avoid edge effects. We reject stars with elongation values greater than 3.0 to ensure all streaks are removed. We calculate the S/N for each star for a range of apertures to account for different size stars, and select the aperture with highest S/N. We required the S/N to be greater than 50 to reduce the computation time of the next step. We also required the S/N to be less than 1,000 to avoid saturated stars. Finally, we rejected stars with outlier FWHM values (partially to avoid double stars), which were identified through four iterations of rejecting stars that have FWHM that are $3\sigma_{\rm MAD}$ outliers.

Step 5: Match stars in all images. We find stars that appear in all images and record the FWHM in each image. To reduce the computation time of this step, we break up the stars into the 2,304 SFP sections and only search for matches within a given section. Stars are considered a match if they are within 12 pixels of each other in different images, and stars are rejected if more than one match is identified in an image.

Step 6: Find height for each star. We fit a parabola to the FWHM vs. z observations for each star to find z_0 (a.k.a., position of the parabolic minima or

[2]PyRAF is a product of the Space Telescope Science Institute, which is operated by AURA for NASA.

the height for that star) and its error—see Fig. 6.2. The parabolic fit is done using Python's scipy.optimize.curve_fit (Jones, Oliphant, Peterson, et al., 2001) function, where FWHM = $\beta(z - z_0)$ + FWHM$_0$ was fit to the observations. This fit returned the optimal coefficients (β, z_0, and FWHM$_0$) and the corresponding estimated covariance matrix. The square root of the diagonal values of the covariance matrix gives the standard deviation of each coefficient. Therefore, this fit returns z_0 and the standard deviation of z_0 for a given star.

Once z_0 is measured using all the images in the through-focus scan, we re-measure z_0 with a subset of the images. We do this to avoid becoming biased by regions far from focus where the parabolic approximation is no longer valid (see Eq. 6.2). The subset of images is defined as the closest five images to the initial z_0 measured or all images within 0.2 mm of z_0, whichever includes more images. Using this subset we measure the final z_0, which gives the height for each star.

Step 7: Average height for each SFP section and measure precision. The heights of all of the stars with x and y positions within a given SFP section are averaged together to determine the height for the section. The heights of the stars are averaged using a weighted average that weights the stars by the reciprocal of the height variance, where this is the error returned from the parabolic fit mentioned in the previous step. If we average the standard deviation of the height for all ZTF stars in the SFP, we measure a standard deviation of 15 μm, which is the typical height error per star. If we average the standard deviation of the height for all ZTF sections in the SFP, we measure a standard deviation of 9 μm, which is the typical height error per SFP section. We conclude the parabola method with ZTF measures the SFP height with a precision of 9 μm.

Step 8: Measure the stability of the height map. We repeat this entire analysis five times with observations from three different days. After removing the global tip and tilt from each height map (see Sec. 6.4), we average all five maps to create a master height map determined using the parabola method (look ahead to Fig. 6.13 to see this master map). To quantify the stability of the height map, we subtract each of the five height maps from the average height map and see how the measured heights of each section changes. For each of these five 'difference maps' we measure the difference between the section that had the largest increase in height and the section that had the largest decrease in height and report this as the peak-to-valley difference. The peak-to-valley difference between each of the five height maps and the averaged map is [40.6, 67.2, 37.4, 25.5, 33.8] with an average of 41 μm. The standard deviation of

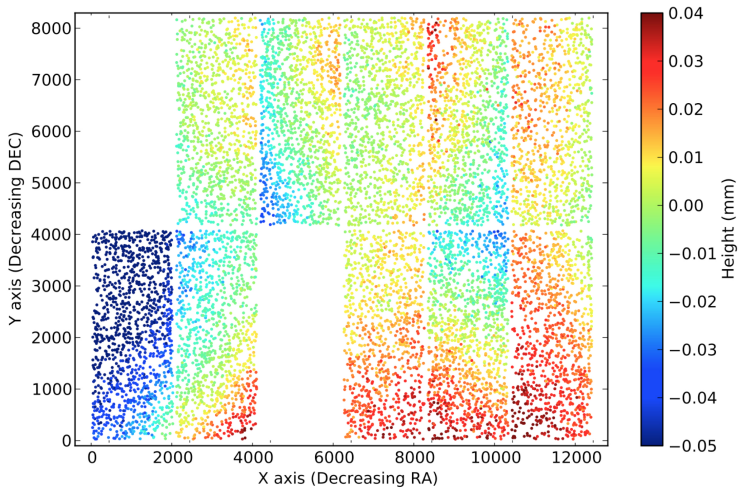

Figure 6.4: Height map of PTF's SFP created from images taken in October 2015. This map shows the heights of individual stars, which have an average height uncertainty of 4.6 μm standard deviation.

the height changes between an individual map and the average map is [6.3, 10.2, 6.5, 4.6, 5.8] with an average of 6.7 μm. The peak-to-valley difference shows that the height in a given section can have large fluctuations. However, the average standard deviation of the height difference between maps of 6.7 μm is consistent with the height uncertainty of 9 μm per section reported in Step 8. We conclude that the ZTF height map is stable within our measurement height errors of 9 μm per SFP section.

Test with PTF to ensure precision

In October 2015, we tested the parabola method on the PTF system as both a verification that this method can achieve the required precision and check against an existing map measured using a profilometer in 2008 (Rahmer et al., 2008).

We used the same procedure described in Sec. 6.3 with some small differences. In addition to pre-scan and over-scan corrections, PTF images need bias and flat field corrections. Each 4k×2k CCD in PTF is divided into $\sim 410 \times 270$ pixel sub-frames for a total of 75 sections per CCD. Two CCDs are missing from this analysis—one was temporarily not functioning properly (the top left CCD in Fig. 6.4) and one wasn't functioning for the duration of the survey.

Smaller spherical aberrations and vignetting with PTF resulted in smaller height uncertainties. The average standard deviation of the height for a star was 4.6 μm (see Fig. 6.3). You can see a height map for individual stars in Fig. 6.4. The map

of the height for the CCD sections is shown in Fig. 6.5, where the average standard deviation of the height for a CCD section was 1 μm.

To measure the stability of the height map, we used three different maps measured from three through-focus scans from the same night. Subtracting these three maps showed that the height differences for CCD sections ranged from -15 to $+15$ μm, so a peak-to-valley differences of 30 μm. The height measurement error of a CCD section (1 μm) is well below the height differences seen in different maps ($\lesssim$ 30 μm). It is possible that we are seeing the PTF CCD mosaic changing shape within a night, possibly due to changing environment (e.g., thermal fluctuations, gravity, or seeing dependent biases). However, additional analysis would have been needed to confirm this. Although the maximum height change between different height maps is larger than the ZTF requirement of 10 μm, more than 90% of the CCD sections had height differences less than 10 μm. Given the measurement error for the height of a CCD section was 1 μm and more than 90% of the CCD sections were stable within 10 μm, this test confirmed that the parabola method would be able to meet ZTF's requirement.

As an important sanity check we compared the height map we measured in October 2015 using the parabola method with the height map published in 2008 using profilometry (Rahmer et al. 2008, compare Figs. 6.5 and 6.6). The maps measure heights of the same overall spatial pattern and the same range across PTF's SFP of $\sim$ 90 μm. Height differences between the two maps of up to $\sim$ 30 μm are seen when comparing specific CCD sections, which is same height difference that was observed when comparing the three PTF height maps to each other. It is worth noting that differences could be due to curvature introduced by the optics which the parabola method would detect but the profilometer would not, simply because the profilometry was measured in the lab instead of in situ. We conclude that the height maps created from profilometry and the parabola method are sufficiently in agreement, and consider this a successful sanity check.

Donut method: second moments of "donuts"

An alternative method of determining the height of the SFP relies upon the calculation of the second moment of image intensity from images sufficiently out of focus such that the stars appear as blurred donuts. We can theoretically use this donut method with a single defocused image; however, it is subject to errors such as those induced by atmospheric seeing. Therefore we use images on either side of focus to

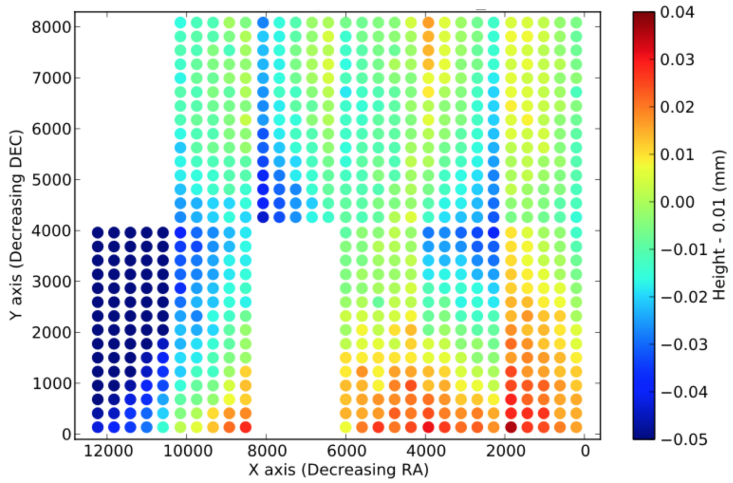

Figure 6.5: Height map of PTF's SFP created from images taken in October 2015. Each CCD is broken into 75 410×270 pixel sub-frames. This map shows the heights of sections, measured by averaging all stars that are in a given section. Each section has an average uncertainty of 1 μm standard deviation. We compared three maps with images taken during the same night and found height differences within the ZTF requirement (10 μm) for 90% of the SFP sections. This verified the stability of the maps and validated the parabola method could be used for ZTF.

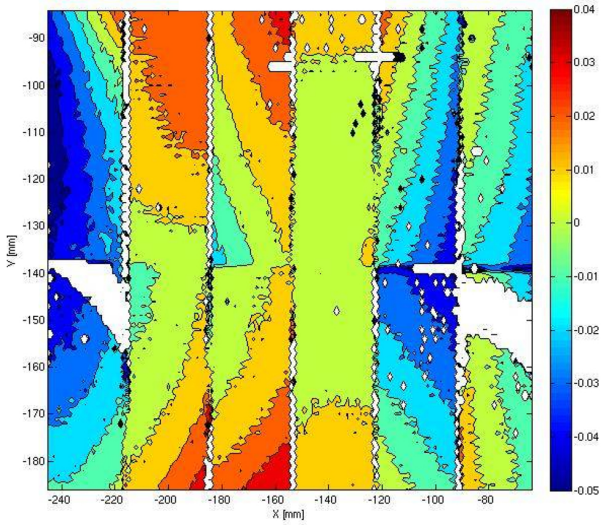

Figure 6.6: *Reproduced from Rahmer et al. (2008), Fig. 9.* Profilometry height map published in 2008 in Rahmer et al. (2008). After they subtracted the global tip and tilt of PTF's SFP, they found the map varied 90 μm peak-to-valley and 17 μm RMS. The calibration they performed reported an accuracy of 10 μm peak-to-valley and 1 μm RMS. Comparing this map to Fig. 6.5 provided an important sanity check, since the overall height pattern was consistent and the same peak-to-valley difference was observed across the plane.

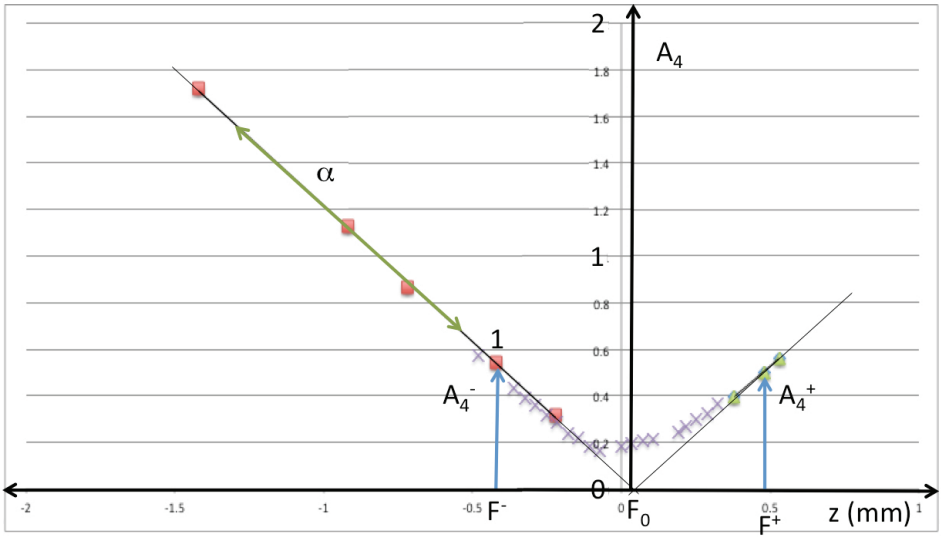

Figure 6.7: Demonstration of the donut method. This is how we use the donut method to determine the height at which a SFP section is in focus (F_0), which is described in Sec. 6.3. The A_4 parameter defined in Eq. (6.5) is plotted vs. the hexapod z position. The squares each represent a 120 sec image—red for images taken below focus and green for images above. The 'x's mark 30 sec images observed for the parabola method. Two thin black lines represent the lines in Eq. (6.6) with slopes of α that pass through an image below focus (A_4^- at position F^-) and above focus (A_4^+ at position F^+). They intersect at position F_0 with a value of $A_4 = \delta$. The δ parameter is essentially zero in this plot, so is not labeled.

measure the height of a SFP section.

Donut algorithm

Given defocused images on both sides of focus, at hexapod z positions F^- and F^+, one can derive the height at which a SFP section is in focus (F_0[3]) in terms of the calculated second moments. Below, we summarize this method originally published in Tokovinin and Heathcote (2006) and refer you to Fig. 6.7 for a graphic depiction.

For a given defocused and pixelated image intensity, I_{ij}, the second spatial moment in x and y are M_x and M_y, respectively, and are defined as

$$M_x = I_0^{-1} \sum (x_{ij} - x_c)^2 I_{ij} \text{ and } M_y = I_0^{-1} \sum (y_{ij} - y_c)^2 I_{ij}. \quad (6.3)$$

[3]Note that F_0 is identical to z_0 used in Sec. 6.3. F_0 is used here to be consistent with the equations in Tokovinin and Heathcote (2006).

The zeroth and first moments used in Eq. (6.3) are

$$I_0 = \sum I_{ij},\ x_c = I_0^{-1} \sum x_{ij} I_{ij},\ \text{and}\ y_c = I_0^{-1} \sum y_{ij} I_{ij}. \tag{6.4}$$

We consider the second moments (M_x and M_y) together to define the parameter A_4,

$$A_4 = \mathrm{p}\sqrt{(M_x + M_y)/2}, \tag{6.5}$$

where p is the angular size of the detector pixels in arcseconds (1.0 arcseconds/pixel for the ZTF camera). With an image above focus (F^+, A_4^+) and below (F^+, A_4^+), two linear relationships are given:

$$A_4^- = \alpha(F_0 - F^-) + \delta \text{ and } A_4^+ = \alpha(F^+ - F_0) + \delta, \tag{6.6}$$

where α is the slope, F_0 is the z position where the lines intersect, and δ is the A_4 value at F_0 (see Fig. 6.7). Here we assume that α and δ are identical on both sides of focus; the effect of these assumptions are discussed in Sec. 6.3. The two A_4 vs. z lines can be combined to solve for F_0, yielding

$$F_0 = (F^+ + F^-)/2 + (A_4^- - A_4^+)/(2\alpha). \tag{6.7}$$

Note that determining the focus with the donut algorithm depends on knowing α. A global α parameter can be calculated for an instrument (e.g., ZTF) by using two images on the same side of focus; however, we find that a position-dependent α parameter is required to reduce error (see Secs. 6.3 and 6.3).

Sources of bias

The donut method relies on the intersection of the linear trend of A_4 vs. z above and below focus, so—like the parabola method—the donut method is only impacted by biases that are asymmetric. Spherical aberrations and vignetting have symmetric impacts when treated individually (see Sec. 6.3 for a more in depth discussion of this).

When treated together, spherical aberrations and vignetting impact the determination of the height using the donut method, specifically by causing a significant dependence of α (see Eq. 6.7) on the star's position in the SFP. To confirm that the

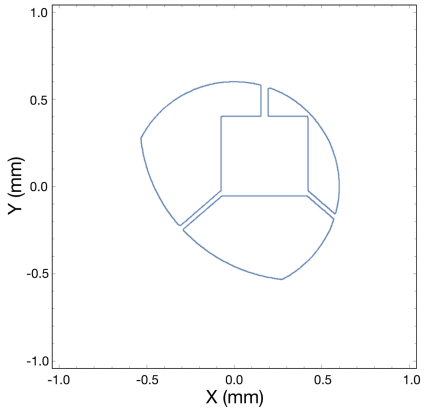

Figure 6.8: Example of the vignetted ZTF pupil used for image simulation. This pupil corresponds to an off-axis field point in the far corner of the ZTF CCD mosaic array (3.5, 3.5) degrees off-axis. The units of the abscissa and coordinate are in meters and are projected onto the telescope entrance pupil. We use the following values: the telescope pupil radius = 0.6 m, cryostat shadow width = 0.498×0.457 m, and primary mirror radius = 0.914 m.

combined effect of spherical aberrations and vignetting is the origin of the dependence of α on position, we generate simulated image data[4] of the ZTF optical system including both $W_{040} = -7$ waves and realistic vignetting across the field (Fig. 6.8). To explore the accuracy of the donut method[5], we generated synthetic image data for each CCD, under the model that individual CCDs sat upon a staircase of relative z positions, each positioned 25 μm higher than the last, in CCD numbering order with CCD S01 being the 'lowest' and thus requiring the largest $+z$ value of hexapod position to focus this CCD. The results of this analysis confirm that the position dependence of α is due to spherical aberrations and vignetting effects, and is particularly sensitive to the large vignetting present in ZTF. This motivated measuring an α map of the SFP from which a polynomial was fitted to determine α at a given pixel (see Step 5 in Sec. 6.3).

An additional impact of the combination of spherical aberrations and vignetting is that α differs slightly on either side of focus. As we mentioned when we introduced the two lines in Eq. (6.6), we assume that α and δ are identical on both sides of focus. A careful study of the two lines in Fig. 6.7 shows that this is not actually true. We

[4]The code to generate this vignetting can be found in the Mathematica workbook, "Analytic moment for obscured image.nb".

[5]Due to the computational burden of producing these simulations, producing enough images to constrain the parabola method was deemed unnecessary.

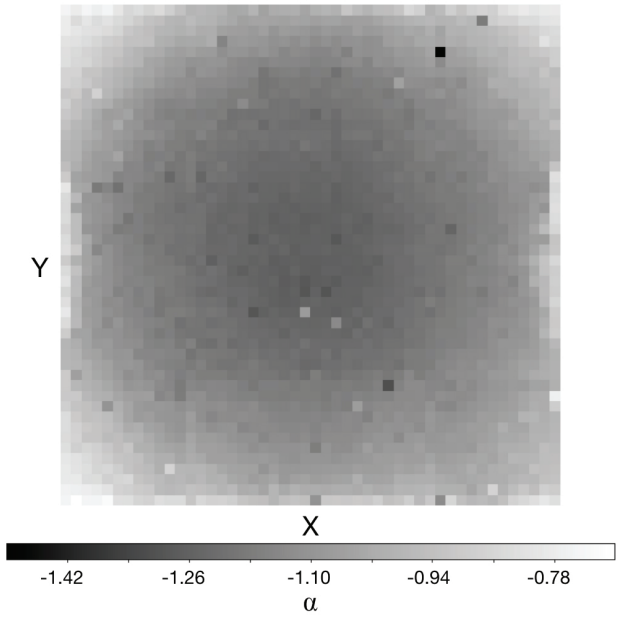

Figure 6.9: Master map of α as a function of position. This is a map of the α parameter as a function of pixel location for the entire SFP. The master map is the median combination of many α maps made with pairs of images on the same side of focus. A parabolic function is fitted to the map shown here, and this function is used when creating height maps with the donut method.

believe α is not symmetric for the same reason the FWHM vs. z was not perfectly parabolic in the parabola method. The fact that α differs on either side of focus causes small errors when determining the z position where these lines intersect (i.e., F_0 or the height). Also note that assuming δ is the same on both sides is valid if the atmospheric seeing is constant for all images used.

Donut procedure

Keeping these biases in mind, here is the detailed procedure we have designed to measure the height for each section of the SFP using the donut method.

Step 1: Collect images. We find that the optimal regime for A_4 values fall within 0.5 and 1.5 for the donut method. In this regime, sources have high S/N, sources are compatible with SExtractor alogirthms, and we are in the linear regime of A_4 vs. z. For ZTF, this corresponds to images roughly 0.5 mm out of focus. We obtained a large set of images taken at the following hexapod z positions: -8.0, -8.5, -9.0, -9.2, -9.8, -9.9, and -9.95 mm. Note that for this set of images the exposure time was 120 seconds and the optimal hexapod z position was -9.41 mm. However, we

find that four images—two on each side of focus—roughly 0.5 mm out of focus are needed to calculate a height map. Two images on the same side of focus are used to measure a map of α and two images on different sides of focus are used to measure a height map of the SFP.

Step 2: Clean images. All images are processed using IRAF (Tody, 1993) by removing the pre-scan and over-scan regions, subtracting a master bias image, and dividing by a master flat field image.

Step 3: Identify stars and measure properties. We extracted the sources from each of the images using SExtractor to obtain the x and y coordinates (in pixels) and the second moments in x and y for each source. Default SExtractor parameters are not designed to find out of focus donuts, so a few adjustments are necessary. The following SExtractor parameters should be adjusted: DETECT_MINAREA, DEBLEND_MINCOUNT, DETECT_THRESH, and ANALYSIS_THRESH[6]. When processing ZTF images the object and memory stack would often over-flow causing some sources to fail during extraction. To adjust for this we increased the MEMORY_OBJSTACK, MEMORY_PIXSTACK, and MEMORY_BUFSIZE by a factor of three from the defaults.

Step 4: Measure median value of $\mathbf{A_4}$ for each SFP section. The original implementation of the donut algorithm (Sec. 6.3) was very computationally intensive. Attempts to identify the same star in images on both sides of focus yielded many stars that could not be properly matched and decreased the population of analyzed stars dramatically. This was a failure of the cross-correlation algorithm and not a fundamental problem with the process. Instead of matching individual donuts, we determined the median value of the A_4 metric for each section of the SFP.

Step 5: Measure $\boldsymbol{\alpha}$ as a function of position. In order to calculate the focus from Eq. 6.7 we need to determine α. We can measure α as a function of position by determining the slope of the line when plotting A_4 vs. z for two images on the same side of focus. Each pair of A_4 images on the same side of focus produces a single α map, and a set of α maps can then be combined into a single master α map (see Fig. 6.9). The master α map can then be fitted to a parabolic function that is then used to calculate α as a function of x and y pixel coordinates. The following parameters[7] describe this function: $\alpha = \mathrm{p00} + \mathrm{p10}x + \mathrm{p01}y + \mathrm{p20}x^2 + \mathrm{p11}xy + \mathrm{p02}y^2$.

[6]For ZTF images we used the following values: DETECT_MINAREA=100-600, DEBLEND_MINCOUNT=0.5, DETECT_THRESH=3.0, ANALYSIS_THRESH=3.0.

[7]For ZTF this equation is $\alpha = -0.7161 - 4.387 \times 10^{-5}x - 4.496 \times 10^{-5}y + 1.693 \times 10^{-9}x^2 +$

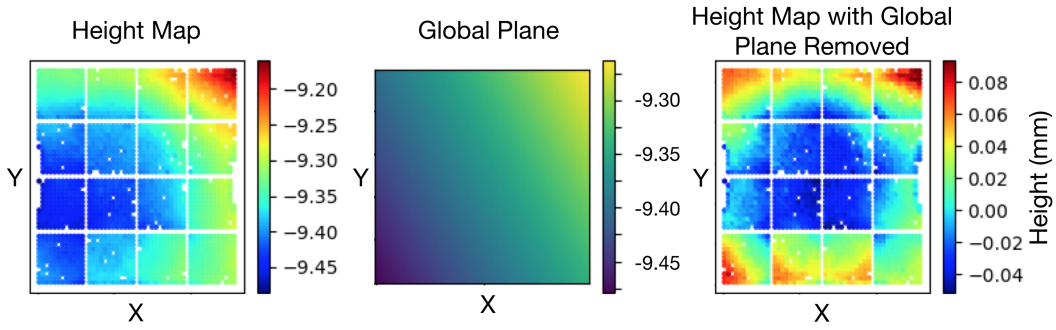

Figure 6.10: Removing the global tip/tilt from a height map. A global plane (center) is fitted to the original height map (left). The plane is subtracted from the original height map to create a new height map (right) that has no global tip/tilt remaining. This new height map can now be accurately combined or compared with other height maps.

Step 6: Find height for each SFP section. Once α has been determined, any pair of images taken on opposite sides of focus can be used to calculate the height from the measured A_4^+ and A_4^- donut metric (based on the SExtractor determined second moments). Height maps were constructed using all of the possible combinations of images taken on opposite sides of focus—11 pairs were used in total. After selecting a set of high quality height maps and removing the global tip/tilt from each map (see Sec. 6.4), the height maps were combined using IRAF (combine=median) to create a master height map (skip ahead to Fig. 6.13 to view this master height map).

6.4 Measuring adjustments to the science focus plane from height maps

Remove global tip/tilt from each map

Althought we did flatten the SFP by iteratively shifting the hexapod and creating a FWHM map (see Fig. 6.1 and Sec. 6.2), global tip/tilts need to be measured and removed from each height map before comparing or averaging them. These global tip/tilts occur due to incorrect alignment of the hexapod and other effects—such as shifting caused by the telescope moving to or being at different positions. Different height maps measured at the same reported hexapod position show different global tip/tilts, so incorrect alignment of the hexapod clearly is not the the only source of misalignment. The global tip/tilt is measured by fitting a plane, $z = \mathrm{a}x + \mathrm{b}y + \mathrm{c}$, to the height map of the entire SFP. Subtracting this plane from the height map removes any global tip/tilt.

$1.114 \times 10^{-10} xy + 1.719 \times 10^{-9} y^2$.

The height maps measured in Sec. 6.3 are formatted as a list of CCD #, x, y, and z_0 values for each SFP section. The x and y parameters are the pixel coordinates for the center of the CCD section with the bottom left pixel of each CCD having coordinate (0,0). The z_0 parameter is height of the section (i.e., the hexapod z position where this section of the SFP is in focus). To fit a plane to the entire SFP, the x and y section coordinates need to be transformed to place them relative to the entire SFP instead of relative to each CCD. We also properly account for the chip gap between CCDs by transforming the distance into number of 15 μm pixels that would fit in the chip gap. For ZTF, there is a 462 pixel-sized gap between CCDs in the x direction and a 645 pixel gap in the y direction. Once we have x and y positions that place the CCDs in the correct pixel positions (see left panel in Fig. 6.10), we fit a plane to the entire SFP.

We fit a plane to a height map using a least squares fit to the data (see center panel in Fig. 6.10). This is done either by using Python's astropy.modeling[8] (The Astropy Collaboration et al., 2018) for height maps created by the parabola method or Matlab's Curve Fitting Toolbox for height maps created by the donut method.

At this point we subtract the plane from the data to return the height map with the global tip/tilt removed (see right panel in Fig. 6.10). Switching the x and y coordinates back to the values relative to each CCD prepares the height map for the next stage—fitting a plane to each CCD.

Fit a plane to each CCD

Once the global tip/tilt is removed from the SFP height map, the height maps from each method can be combined (see Step 8 in Sec. 6.3 and Step 6 in Sec. 6.3). When we have a master height map for each method, we fit a plane ($z = \mathrm{a}x + \mathrm{b}y + \mathrm{c}$) using the same technique described in Sec. 6.4 to the height map of each CCD (see left panel in Fig. 6.11). The coefficients of the plane equation (a, b, c) are then used to calculate a new image that represents the plane fit to the individual CCD (see center panel in Fig. 6.11). The resulting plane fit image is then subtracted from the master height map to evaluate the residual features in the image that are not accounted for by the planes (see right panel in Fig. 6.11).

As an aside, this technique can be used to study the shape of the individual CCDs. Figure 6.12 shows the residual features of each CCD after the CCD plane is sub-

[8]We fit a plane using Python with these two commands:
p_init = astropy.modeling.models.Polynomial2D(degree=1) and
fit_p = astropy.modeling.fitting.LevMarLSQFitter()

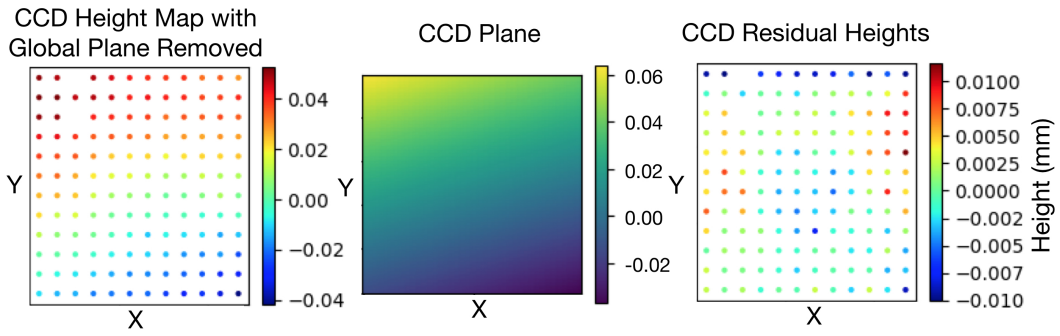

Figure 6.11: Fit a plane to each CCD. After the global tip/tilt has been removed from a height map, we can fit a plane (center) to each CCD height map (left, CCD S02 in this example). This plane provides a formula to calculate the height corrections that should be applied to each CCD support in order to flatten the SFP (see Table 6.1). Subtracting the plane from the CCD height map results in the CCD residual heights (right).

tracted. This shows $\sim 8-15\,\mu$m peak-to-valley height differences within a CCD with a typically concave shape. It is important to note that these residuals also include light contamination (e.g., scattered light), so this is not a pure measurement of CCD shape. For these ZTF images, you can see contamination from outgassing material. Since these images were taken, all outgassing material has been replaced and all signs of contamination have been removed.

6.5 Compare the results of the parabola and donut methods

The master height maps measured using the two different methods—parabola and donut—are shown in Fig. 6.13. The two methods produced very similar height maps—both in magnitude and the overall spatial pattern. By subtracting these two height maps (Fig. 6.14), we measure a maximum section height decrease of $-22\,\mu$m and a maximum section height increase of $+26\,\mu$m, which results in a $48\,\mu$m peak-to-valley height difference between the maps. The standard deviation of the height differences between these two maps is $8\,\mu$m. If you recall, the precision that we were able to calculate the height of a section of the SFP using the parabola method was $9\,\mu$m (Step 7 in Sec. 6.3), so this level of difference between the two maps is within our measurement error. In addition, similar height differences were observed between maps measured solely by the parabola method ($41\,\mu$m peak-to-valley and $6.7\,\mu$m standard deviation, Step 8 in Sec. 6.3). We do not see a clear reason why one method is more intrinsically precise than the other, so our final results are an

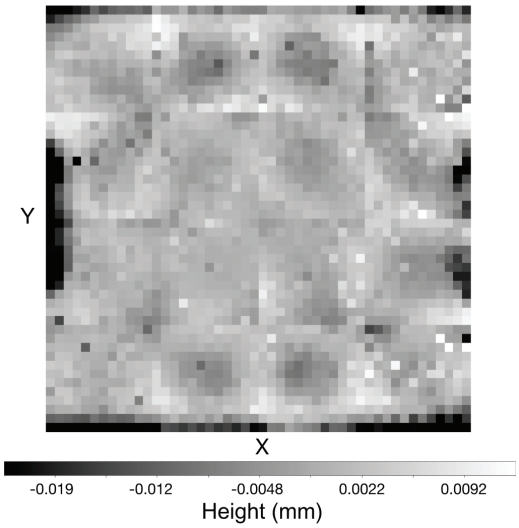

Figure 6.12: CCD residual heights. This is a map of each CCD's residual heights (an example can be seen in the right panel of Fig. 6.11). Although CCD gaps are not displayed in this image, the 16 CCDs can still be distinguished by eye. This height map shows that many of the CCDs have a concave shape and have $\sim 8-15$ μm height differences. Please note that this image includes contamination due to outgassing material (specifically see the darkened edges). The gaskets that support the cryostat window have since been replaced and all signs of contamination have been removed.

average of these two maps. From this average, we now can determine how the SFP should be repositioned.

6.6 Final science focal plane adjustments

We fit the final CCD planes to each CCD from the final height map—the average of the master height map created via the parabola and donut method. The coefficients for each CCD plane is given in Table 6.1. The CCD naming convention is that the CCD number increases as you follow the row from left to right, and then continue this trend on the row below. Therefore the top-left CCD is S01, the top-right CCD is S04, the bottom-left CCD is S13, and bottom-right CCD is S16.

The sign convention is that these coefficients represent the measured *hexapod z* position that brought each CCD into focus (with positive values moving the hexapod toward the telescope's primary mirror). Thus, these values also represent *the required adjustment* to the current CCD positions. For example, a negative fit plane height represents a point on the CCD where the hexapod had to move away from the primary mirror to reach focus, so this point on the CCD is currently too 'high' relative to the cryostat body and needs to be 'lowered' with respect to the cryostat

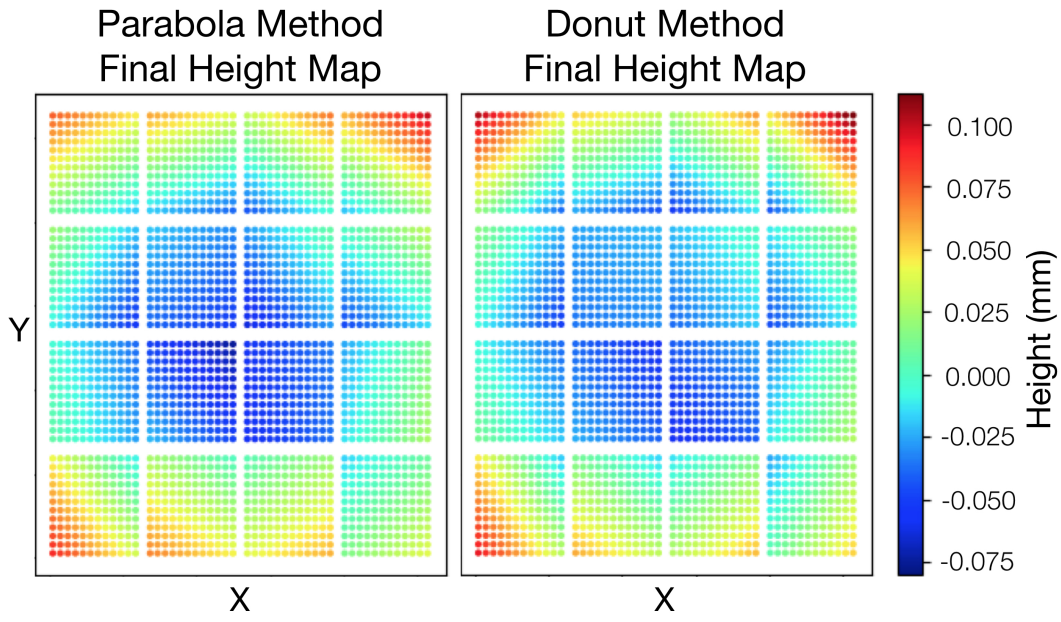

Figure 6.13: Master height maps using the parabola method (left) and donut method (right). This shows the CCD plane fitted to each CCD (see center panel in Fig. 6.11) for the two different methods. Figure 6.14 shows the difference between these two maps. An average of these two maps was used to calculate the final plane coefficients in Table 6.1.

body.

These planes therefore describe the correction that should be applied to the CCD supports in order to flatten the SFP. Each CCD has three supports and the height adjustment applied to each support can be found by finding the value of the CCD plane at the pixel above each support. The details of this conversion are beyond the scope of this proceeding.

6.7 Conclusion

The ZTF requirement is to measure the SFP within 10 μm RMS. Initially we use a stellar FWHM map to place the SFP in approximate focus. In variable seeing this technique can determine the hexapod z position where the SFP is in focus within 35 μm (Fig. 6.1). Following this, we use two different methods for creating a height map of the SFP—the parabola and donut method. Using the parabola method, the precision of the section heights is 9 μm standard deviation (Step 7 in Sec. 6.3), and the stability of the section heights is 6.7 μm standard deviation (Step 8 in Sec. 6.3). After removing the global tip/tilt from the height maps, we

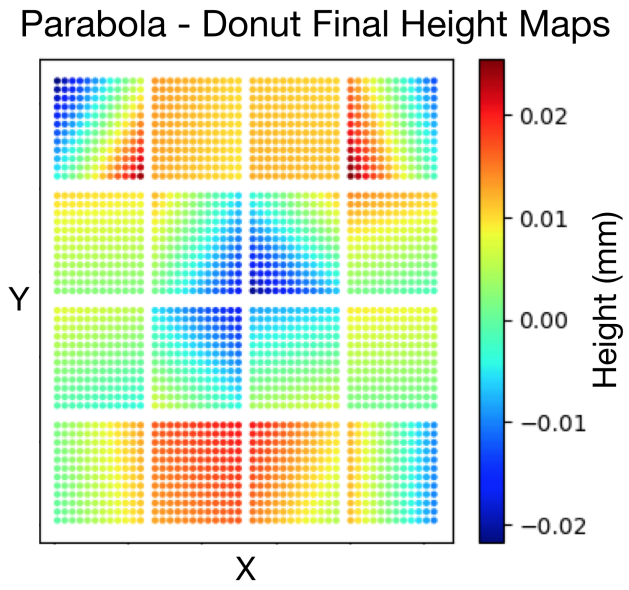

Figure 6.14: Height difference between the two methods. This is a map of the subtraction between the master height maps calculated using the parabola and donut methods (these maps are shown in Fig. 6.13). The height differences vary 48 μm peak-to-valley and the standard deviation of this difference map plotted is 8 μm. The height difference of the results of our two methods (8 μm standard deviation) is within the ZTF requirement.

combine them to make a master map for each method. At that point we fit a plane to the CCDs in each map. The section heights of these two sets of planes (Fig. 6.13) agree within 8 μm standard deviation (Fig. 6.14), which is within the ZTF requirement. Our final height map is the the average of the results from the parabola and donut methods. The final CCD plane coefficients (Table 6.1) determine how the CCDs should be repositioned. Based on the results presented in this chapter, the CCD supports were reshimmed to adjust the CCD heights to flatten the SFP. Some errors were introduced when converting the planes described in Table 6.1 to height corrections to the CCD supports, and efforts to correct this are ongoing. Even with these flaws, the standard deviation of the height across the entire SFP measured before and after the SFP was repositioned decreased from 33 to 14 μm. We calculate that this reduction in the height variation would improve the typical FWHM from approximately 2.80″ to 2.08″. This decrease in FWHM would reduce the integration needed to reach a given brightness by 45%. Without a thorough calculation that incorporates all contributions to the survey speed (e.g., overhead time between images), we approximate the impact this has on the survey speed by

Table 6.1: Final plane coefficients for the 16 ZTF science CCDs. All z values describe the required adjustment to the current CCD positions to flatten the SFP. The equation of each plane is $z = \mathrm{a}x + \mathrm{b}y + \mathrm{c}$, where a positive height value implies that point on the focal plane needs to be raised (moved in $+z$ with respect to the cryostat cold plate). The origin for the (x,y) coordinate system is the center of lower-left pixel (0,0) for each CCD.

CCD	a (μm/pixel)	b (μm/pixel)	c (μm)
S01	-0.00772	0.01374	16.9
S02	-0.00289	0.01409	-18.4
S03	0.00714	0.01368	-40.9
S04	0.01018	0.01581	-29.8
S05	-0.00728	0.00538	-9.6
S06	0.00026	0.00315	-39.8
S07	0.00530	0.00509	-49.3
S08	0.00570	0.00711	-40.2
S09	-0.00519	-0.00204	2.1
S10	-0.00285	-0.00269	-27.5
S11	0.00343	0.00227	-58.2
S12	0.00731	-0.00215	-12.4
S13	-0.00921	-0.00772	81.8
S14	-0.00409	-0.00750	58.7
S15	0.00483	-0.00581	25.6
S16	0.00692	-0.00563	7.4

converting the 45% time reduction directly to an increase in survey speed of 81%.

ACKNOWLEDGEMENTS

This material is based upon work supported by the National Science Foundation Graduate Research Fellowship under Grant No. DGE-1745301. This work is based on observations obtained with the Samuel Oschin Telescope 48-inch and the 60-inch Telescope at the Palomar Observatory as part of the Zwicky Transient Facility project, a scientific collaboration among the California Institute of Technology, the Oskar Klein Centre, the Weizmann Institute of Science, the University of Maryland, the University of Washington, Deutsches Elektronen-Synchrotron, the University of Wisconsin-Milwaukee, and the TANGO Program of the University System of Taiwan. Further support is provided by the U.S. National Science Foundation under Grant No. AST-1440341.

References

Bertin, E. and S. Arnouts (1996). "SExtractor: Software for source extraction." In: *Astronomy and Astrophysics, Supplement* 117, pp. 393–404. DOI: 10.1051/aas:1996164.

Dekany, Richard et al. (2016). "The Zwicky Transient Facility Camera". In: *Proc. SPIE*. Vol. 9908. Society of Photo-Optical Instrumentation Engineers (SPIE) Conference Series, p. 99085M. DOI: 10.1117/12.2234558.

Jones, Eric, Travis Oliphant, Pearu Peterson, et al. (2001). *SciPy: Open source scientific tools for Python*. [Online; accessed 2017-01-16]. URL: http://www.scipy.org/.

Rahmer, G. et al. (2008). "The 12K×8K CCD mosaic camera for the Palomar Transient Factory". In: *Ground-based and Airborne Instrumentation for Astronomy II*. Vol. 7014. Proceedings of the SPIE, 70144Y. DOI: 10.1117/12.788086.

Reiley, D. J. et al. (2017). "Optical design of the Zwicky Transient Facility: a major upgrade to the 48" Schmidt Camera at Palomar Observatory". In: *Society of Photo-Optical Instrumentation Engineers (SPIE) Conference Series*. Vol. 10590. Society of Photo-Optical Instrumentation Engineers (SPIE) Conference Series, 105901U. DOI: 10.1117/12.2292085.

The Astropy Collaboration et al. (2018). "The Astropy Project: Building an inclusive, open-science project and status of the v2.0 core package". In: *ArXiv e-prints*. arXiv: 1801.02634 [astro-ph.IM].

Tody, D. (1993). "IRAF in the Nineties". In: *Astronomical Data Analysis Software and Systems II*. Ed. by R. J. Hanisch, R. J. V. Brissenden, and J. Barnes. Vol. 52. Astronomical Society of the Pacific Conference Series, p. 173.

Tokovinin, A. and S. Heathcote (2006). "Donut: Measuring Optical Aberrations from a Single Extrafocal Image". In: *Publications of the ASP* 118, pp. 1165–1175. DOI: 10.1086/506972. eprint: astro-ph/0606388.

Chapter 7

OUTRO

This thesis demonstrates that MRS can reliably measure barium abundances in red giants in nearby dwarf galaxies (Chapter 2). Using MRS increases the efficiency of barium abundance measurements. The subsequently reduced observational resources required to measure barium abundances will enable more surveys to make these measurements (e.g., PFS, Sugai et al. 2015). Larger catalogs of stars with barium abundances will further expand our knowledge of the *s*- and *r*-processes, because barium abundances are an important probe of both—as discussed at length in this thesis.

Chapter 2 presents the largest catalog of barium abundances in dwarf galaxies to date. All of the parameters and abundances in this catalog of $\sim$ 250 stars are measured in a self-consistent way. Many simulations and models currently compare their predictions to the Milky Way halo (e.g., van de Voort et al., 2019; Naiman et al., 2018), mainly because there are numerous [Eu/Fe] measurements. However, a large percentage of the stars in the Milky Way halo are stars stripped from various dwarf galaxies. Comparing simulations to an intact dwarf galaxy is a better approach because these stars are described by a simpler chemical evolution of a single system. Therefore, our catalog of dwarf galaxy abundances is a useful resource to compare the abundances reported in simulations and models. Preliminary results in Chapter 4 show that this comparison can be used to verify the *r*-process origins, rates, and yields required to explain the observed abundances.

Our analysis of the abundance trends within a dwarf galaxy reveal that the *r*-process trend ([Ba/Fe]$_r$) is significantly more positive than the α-element trend ([Mg/Fe]) at early times ([Fe/H] < -1.6, Chapter 3). This is seen in three different dwarf spheroidal galaxies—Sculptor, Draco, and Ursa Minor. Because α-elements are created in CCSNe and have a different slope than the *r*-process, the majority of the *r*-process is not created by any type of massive star death (e.g., a rare CCSNe). This is an important observational constraint in the search for the *r*-process origin and supports NSMs being the dominant source of the *r*-process early in the history of dwarf galaxies.

An additional observational constraint in the search for the *r*-process origin is the

r-process abundances in globular cluster M15. There is $\sim$1 dex spread in [Ba/Fe] and [Eu/Fe] abundances, even though the [Fe/H] and [α/Fe] abundances do not show a significant spread (e.g., Sneden, 1973). In Chapter 5, we test if the answer to this unusual abundance pattern is a r-process event (e.g., NSM) occurring after the stars in the cluster were born and unevenly polluting the surfaces of the stars in the cluster. We found that is not the case. The only explanation is that a very prompt r-process event occurred before the observed stars were born. This supports the idea that a type of massive star death (e.g., a rare CCSNe) contributed the unusual r-process enrichment in this globular cluster.

I am excited to see how the observational puzzles created by the different abundance trends in different clusters and galaxies are explained by r-process origin(s). In addition to studying the r-process with chemical abundances, directly finding individual NSMs with LIGO and pinpointing the NSM's location with transient surveys is another important way of determining the r-process origin. Chapter 6 discusses one of many challenges in building a large camera for a transient survey. The hardware and software required to run a large transient survey is complex. Understanding the challenges faced by current transient surveys (e.g., ZTF) will help scientists prepare for future surveys like LSST (Abell et al., 2009). Thankfully, the invested money, time, and effort in ZTF is already being rewarded in the form of important discoveries (e.g., Bellm et al., 2019; De et al., 2019; Burdge et al., 2019; Ho et al., 2019). In the future, when we have several NSMs near enough to find and follow up with transient surveys, we will have direct observational constraints on the rate and yield of NSMs. This, combined with the observational constraints provided by chemical abundances, should allow the question of where the r-process elements are made to be answered at last.

References

Abell, P. A. et al. (2009). "LSST Science Book, Version 2.0". In: arXiv: 0912.0201.

Bellm, Eric C. et al. (2019). "The Zwicky Transient Facility: System Overview, Performance, and First Results". In: *PASP* 131.995, p. 018002. DOI: 10.1088/1538-3873/aaecbe. arXiv: 1902.01932 [astro-ph.IM].

Burdge, Kevin B. et al. (2019). "General relativistic orbital decay in a seven-minute-orbital-period eclipsing binary system". In: *Nature* 571.7766, pp. 528–531. DOI: 10.1038/s41586-019-1403-0. arXiv: 1907.11291 [astro-ph.SR].

De, Kishalay et al. (2019). "ZTF 18aaqeasu (SN2018byg): A Massive Helium-shell Double Detonation on a Sub-Chandrasekhar-mass White Dwarf". In: *ApJL*

873.2, L18, p. L18. DOI: 10.3847/2041-8213/ab0aec. arXiv: 1901.00874 [astro-ph.HE].

Ho, Anna Y. Q. et al. (2019). "Evidence for Late-stage Eruptive Mass-loss in the Progenitor to SN2018gep, a Broad-lined Ic Supernova: Pre-explosion Emission and a Rapidly Rising Luminous Transient". In: *arXiv e-prints*, arXiv:1904.11009, arXiv:1904.11009. arXiv: 1904.11009 [astro-ph.HE].

Naiman, Jill P. et al. (2018). "First results from the IllustrisTNG simulations: a tale of two elements - chemical evolution of magnesium and europium". In: *MNRAS* 477.1, pp. 1206–1224. DOI: 10.1093/mnras/sty618. arXiv: 1707.03401 [astro-ph.GA].

Sneden, C. A. (1973). "Carbon and Nitrogen Abundances in Metal-Poor Stars." PhD thesis. THE UNIVERSITY OF TEXAS AT AUSTIN.

Sugai, H. et al. (2015). "Prime Focus Spectrograph for the Subaru telescope: massively multiplexed optical and near-infrared fiber spectrograph". In: *Journal of Astronomical Telescopes, Instruments, and Systems* 1.3, 035001, p. 035001. DOI: 10.1117/1.JATIS.1.3.035001. arXiv: 1507.00725 [astro-ph.IM].

van de Voort, Freeke et al. (2019). "Neutron star mergers and rare core-collapse supernovae as sources of r-process enrichment in simulated galaxies". In: *arXiv e-prints*, arXiv:1907.01557, arXiv:1907.01557. arXiv: 1907.01557 [astro-ph.GA].